Experimental and Theoretical study of Ionospheric Irregularities in the F Region at Low-Latitudes(Dissertation_全文)

AUTHOR(S):

Maruyama, Takashi

(2)

Experimental and Theoretical Study of Ionospheric Irregularities in the F Region at Low-Latitudes

by

Takashi Maruyama

December 1991

Abstract

This thesis deals with morphological features of equatorial spread F clarified by the satellite measurements, i.e., seasonal-longitudinal effect of spread F occurrence. The physical mechanism producing seasonal and longitudinal variations is discussed theoretically and numerically.

The occurrence probability of topside spread F is examined based on the ISS-b (Ionosphere Sounding Satellite -b) ionograms. Spread echo traces are identified from the digital ionogram data with the aid of a computer instead of generally-used manual scaling by eye. Global distribution maps of spread F are derived as a form of occurrence probability for three different periods, August-December, November-March, and February-June. These maps of occurrence probability revealed many global perspectives of spread F such as large occurrence probability at high and equatorial latitudes with relatively quiescent regions at around 30° in magnetic latitude in both hemispheres. Most important finding among them is a significant and systematic longitudinal-seasonal variation in the occurrence of equatorial spread F (ESF). The longitudes of high occurrence probability appear to be characterized by the declination angle of the earth's magnetic field.

For further investigation of the longitudinal control of equatorial spread F, distribution maps of the ESF activity are derived. Because, as a nature of the orbit of ISS-b, a data set for four months is required to derive spread F distribution maps for the whole globe in terms of primitive occurrence probability; a different method is applied here. Spread F is dealt with quantitatively and its index is defined for each ionogram. The functional fitting is applied of the spread F index to draw distribution map for each month. Thus seasonal and longitudinal characteristics of ESF are successfully separated as follows: The ESF activity during the northern winter period reveals maximum enhancement at the longitudes of large westward geomagnetic declination angle (Atlantic longitudes), similarly, during the northern summer at the longitudes of large eastward declination (Pacific longitudes), and during equinoctial seasons at the longitudes of small declination angle (Indian longitudes).

As a next step, we consider a possible mechanism that produces above-noted seasonal-longitudinal effect. For this purpose the background large scale electron density distributions at the satellite altitude are examined. We determined the electron density at the satellite height from the strengths of cosmic radio noise which were recorded simultaneously with the topside soundings. The analysis is based on the fact that the radio noise strengths rapidly decrease below the local plasma frequency at the satellite. Distribution maps of the electron density are obtained for

typical northern winter and summer seasons. The results reveal that the large-scale electron density structure tends to be symmetric with respect to the magnetic equator in the regions of high ESF activity and asymmetric in the regions of low ESF activity. These symmetry/asymmetry features are taken account of by the influence of a transequatorial component of thermospheric winds in the magnetic meridional plane. We propose that the change in plasma distribution along the magnetic field line due to the transequatorial wind component plays an important role to suppress the plasma instability or generation of spread F. In the mechanism proposed here the contributions from plasma away from the equator are important. However most existing theory of equatorial spread F, the gravitational Rayleigh-Taylor instability, is two-dimensional approximation in the magnetic equatorial plane. Thus we need to develop a non-local theory of Rayleigh-Taylor instability.

An analytical expression of the gravitational Rayleigh-Taylor instability including the contributions from plasma away from the equator is derived. For numerical calculation of the growth rate, vertical and latitudinal distribution of the electron density must be known. (Zonal distribution is assumed to be uniform as a ground state.) As it is impossible to model the complete density distribution based on observations, the electron density distribution is obtained by solving the ion continuity equations including dynamics for O^+, NO^+, O_2^+, and N_2^+ ions. Effects of the transequatorial component of the thermospheric wind and the ambient $\boldsymbol{E}\times\boldsymbol{B}$ drift are included in the modeling of the ion density. The numerical calculations confirm that there exists an appreciable thermospheric wind effect on the growth rate of the instability as we have expected from the observations.

So far the nomenclature of "equatorial spread F" has been used without paying any attention to the latitudinal extension. It is an interesting issue to consider whether the irregularities at the subtropical latitudes to lower midlatitudes are identical to the equatorial spread F or intrinsic at those latitudes. The non-local theory developed for the equatorial spread F is applied at subtropical to lower midlatitude region. Some observed features of irregularities by the ISS-b satellite and others may be explained as to be generated at those latitudes. The plasma instability at subtropical and lower midlatitudes is shown to be the $\boldsymbol{E}\times\boldsymbol{B}$ drift instability driven on the bottomside.

Acknowledgments

The author wishes to express his hearty and sincere gratitude to Professor Iwane Kimura of Kyoto University for his guidance and supervision to finish this thesis.

The author wishes to thank Professors Susumu Kato and Shoichiro Fukao of Kyoto University for their helpful comments and guidance throughout the work.

The major part of the work, Chapters 2 and 3, is greatly in debt to the ISS project in the Radio Research Laboratories (currently Communications Research Laboratory) of Ministry of Posts and Telecommunications. The author wishes to express his sincere gratitude to Professor Nobuo Matuura of Nagoya University, the former Director of the Radio Science Division of the Radio Research Laboratories, for his advice and guidance of the research in the ISS project.

A part of this work, Chapter 4, was carried out when the author was staying at Cornell University in the United States of America as a visiting fellow. The author wishes to thank Professor M.C. Kelley of Cornell University for his helpful discussion and comments.

The author also would express his hearty appreciation to Drs. Nobuyoshi Fugono, the Director General of the Communications Research Laboratory, and Tadahiko Ogawa of the Hiraiso Solar Terrestrial Research Center, Communications Research Laboratory, and Professor Noboru Wakai of Tohkai University, the former Director General of the Radio Research Laboratories, for their continual encouragement throughout the work.

Table of Contents

List of Figures

List of Tables

Chapter 1: General Introduction

1.1. Historical background

We first make a historical survey of ionospheric irregularities in the F region, which is stressed on the global morphology of spread F. A general review of spread F is not intended because there are a number of excellent review works on this problem (e.g., FEJER and KELLEY, 1980).

1.1.1. Global morphology In the ionospheric F region electron density irregularities often develop, which are called spread F since they were first recognized as diffuse echo traces on ionograms. Spread F and its related phenomena have been studied by means of a variety of observational techniques such as bottomside soundings, topside soundings, ground-based radar observations, satellite in-situ measurements, radio wave beacon signals, optical method, and so forth.

It has long been known that appearance of spread F varies with local time, season, geographical location, and many other geophysical conditions (SHIMAZAKI, 1959; HERMAN, 1966). At an early stage of the spread F study, SHIMAZAKI (1959) proposed the spread F equator that divides the global area into two hemispheric regions to describe seasonal and longitudinal characteristics of spread F. In the hemisphere north of the spread F equator, large spread F occurrence appears around the December solstice and the June solstice in the south of it as shown in Figure 1.1. HERMAN (1966) suggested a mechanism to generate ionospheric irregularities responsible for spread F based on the idea of spread F equator. However the spread F equator takes no account of the important factors that spread F appears near equinoxes in most equatorial stations and occurrence of spread F exhibits large latitudinal dependence.

The spread F equator was derived from an analysis of the bottomside sounding data obtained at the ground-based ionosonde stations. There may be two major difficulties in studying global morphology of spread F based on the bottomside soundings.

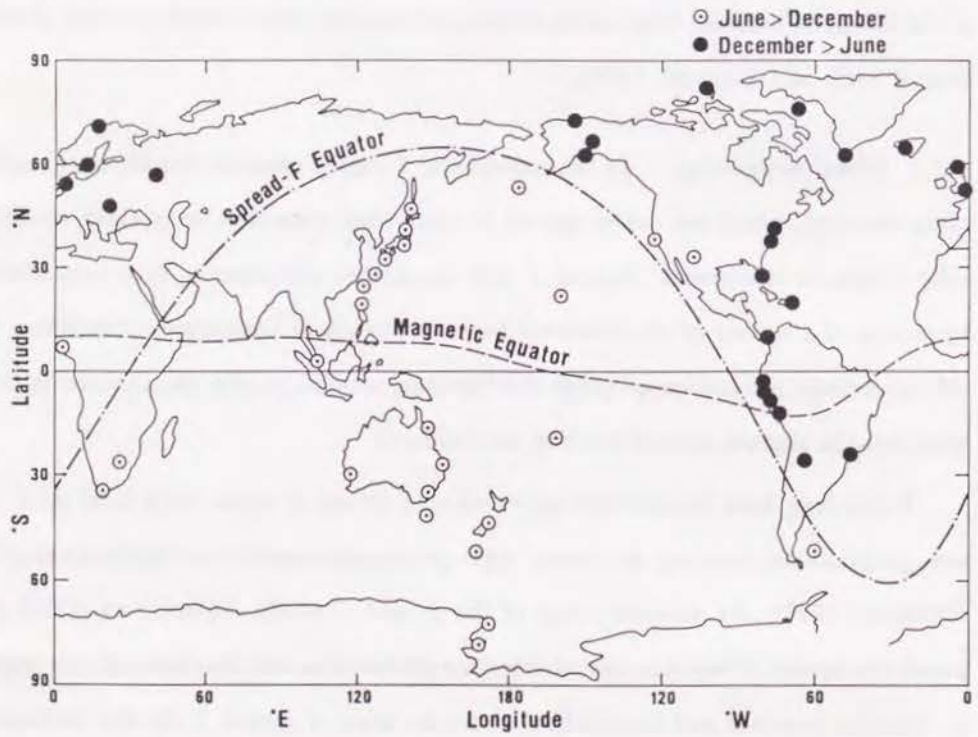

Fig. 1.1. Spread F equator reproduced from SHIMAZAKI (1959). At the stations in the north of the spread F equator shown by the dash-dotted curve, occurrence probability of spread F in the December solstice is higher than that in the June solstice, while at the stations in the south of it, the occurrence probability in the June solstice is higher than that in the December solstice. The magnetic equator determined from the magnetic dip angle is shown by the broken curve.

The first is the limited number of stations, and furthermore they distribute unevenly over the world as noticed in Figure 1.1; locations of the station are limited in land areas. In particular, at the equatorial latitudes, stations are scarce because of the Pacific and Atlantic Oceans. The second is the lack of reliability of spread F information which cannot be removed by statistical procedure. Usually, spread F can be determined from the letter "F" in the monthly tabulation of the ionospheric critical frequency, f_oF_2, issued by local organizations independently. There is, however, no quantitative standard to scale spread F. Historically, the scaling of ionospheric parameters has been devoted to engineering interests for the short wave communications, for which the ionospheric critical frequency is the most important parameter and the spread F information attached to the scaled f_oF_2 value is considered to be a subsidiary parameter to provide the quality of the scaled value. Thus it is almost impossible to compare the spread F activity at different stations.

Ambiguity in the morphological studies based on the ground observations alone has been much improved by realization of satellite techniques. The first topside sounding satellite, Alouette 1, confirmed existence of spread F irregularities extending into the topside ionosphere with elongation along the earth's magnetic field lines (LOCKWOOD and PETRIE, 1963). A pattern of spread F occurrence in geomagnetic latitude and local solar time was investigated by CALVERT and SCHMID (1964) from the Alouette 1 topside ionograms recorded over the regions along the meridian of 75°W by the ground station network (FRANKLIN *et al.*, 1969). The pattern of topside spread F occurrence showed existence of the region of nighttime equatorial spread F (ESF) distinguishable from the other latitude regions. MULDREW (1980*a*, *b*) and MARUYAMA and MATUURA (1980) investigated the global morphology of ESF by using topside ionograms and showed seasonal variation in the longitude of high occurrence probability of ESF.

In-situ measurements of ionospheric irregularities by means of the satellite-borne probes are also powerful tools for the study of ESF. HANSON and SANATANI (1971)

found from the retarding potential analyzer (RPA) experiments onboard the OGO 6 satellite that the occurrence probability of ESF irregularities was higher in the Atlantic region than any other longitudinal regions. HANSON *et al.* (1973) discussed about the formation mechanism of ESF irregularities on the basis of the OGO 6 observations and suggested the influence of both neutral winds and metallic ions, Fe^+ , as the controlling factors. BASU *et al.* (1976) derived a morphological model of equatorial scintillations based on the OGO 6 RPA measurements of electron density irregularities during the period of November-December in 1969 and 1970, and showed that the highest percentage occurrence of scintillations appeared at the Atlantic longitudes with a subsidiary maximum at the Pacific longitudes. A similar longitudinal variation of ESF irregularities was observed by means of the spherical electrostatic analyzer onboard the ISIS 1 satellite (BURKE *et al.*, 1979). BURKE *et al.* (1980) also showed plasma bubbles are often observed at the Atlantic longitudes. Thus fairly clear picture of global morphology for ESF was obtained, although it is not completed (BASU and BASU, 1985).

1.1.2. Physical mechanism Turning to the efforts to investigate physical mechanisms directly responsible for the generation of irregularities, it seems to be a key point to take account for the resemblance between the morphological features of topside and bottomside spread F that has been shown by CALVERT and SCHMID (1964). However, this resemblance was a statistical result. FARLEY *et al.* (1970) found that ESF irregularities appear almost simultaneously in bottomside, peak electron density, and topside regions of the F layer using VHF radar at Jicamarca (11°57' S, 76°52' W; dip$\simeq$1°N), near Lima, Peru. This simultaneous occurrence and other observed characteristics ruled out any previous theories on the generation of ionospheric irregularities (FARLEY *et al.*, 1970). Although BALSLEY *et al.* (1972) agreed with FARLEY *et al.* (1970) that none of the existent theories explains the whole set of phenomena associated with ESF, they demonstrate that the collision-dominated Rayleigh-Taylor instability is capable of setting up primary ESF irregularities.

WOODMAN and LAHOZ (1976) conducted experiments by the Jicamarca radar with new observational techniques designed to study the ESF irregularities, and they proposed a mechanism to explain the coexistence of irregularities in the bottomside and topside regions. That is, a plasma depleted region or plasma bubble first appears at the unstable bottomside and then the plasma bubble penetrates up to the higher electron density region of the F layer by the buoyancy force in analogy of hydrodynamics and eventually it reaches the topside which is a linear stable region. Thus small scale ESF irregularities may appear on the bottomside and also on the topside almost simultaneously by secondary instabilities within and around the bubbles or along the wake of them.

Succeeding extensive experimental and numerical studies support the scenario proposed by WOODMAN and LAHOZ, (1976): two dimensional nonlinear computer simulation revealed an upwelling of density depletion (SCANNAPIECO and OSSAKOW, 1976); rising plasma bubbles were directly detected by a satellite-borne probe (MCCLURE *et al.*, 1977); airglow depletions due to the plasma bubble associated with spread F were observed at the equator (WEBER *et al.*, 1978) and from the subtropical latitude station (MALCOLM *et al.*, 1984). It is now generally accepted that the basic mechanism for the generation of ESF irregularities is the nonlinear evolution of the gravitational Rayleigh-Taylor instability in combination with the $\boldsymbol{E}\times\boldsymbol{B}$ drift instability (BASU and KELLEY, 1979; KELLEY and MCCLURE, 1981; OSSAKOW, 1981)

The global morphology of equatorial spread F should be discussed in terms of the Rayleigh-Taylor instability. There are some candidate mechanisms to explain the longitudinal and seasonal characteristics of equatorial spread F. That is, longitudinal and seasonal changes in ionospheric parameters yield the change in the growth rate of the instability or trigger mechanism: (1) the reversal time of the zonal electric field from eastward to westward in the evening hours (RASTOGI, 1980); (2) the E region dynamo field which generates field aligned currents due to a hemispheric asymmetry of

the field (MULDREW, 1980*a*); (3) the transequatorial component of the thermospheric wind which modifies the Pedersen conductivity integrated along the magnetic field line (MARUYAMA and MATUURA, 1984); and (4) the longitudinal gradient of the integrated E region conductivity determined by the solar declination and the magnetic declination angles (TSUNODA, 1985). The third mechanism is examined in this study, in which the contribution of plasma laying off the equatorial plane must be considered. The asymmetric distribution of the ionization due to the transequatorial wind may result in an increase in the magnetic field line integrated Pedersen conductivity, which suppresses the growth of the Rayleigh-Taylor instability.

Effects of the transequatorial thermospheric wind on the ionospheric plasma distribution at low latitudes have been studied by many workers (BITTENCOURT *et al.*, 1976; BITTENCOURT and SAHAI, 1978; ANDERSON and ROBLE, 1981). According to these, a poleward wind transports ionization to the lower altitudes along the magnetic field line through the momentum transfer from the neutral particles to ions, while at the same time an equatorward wind transports ionization to the higher altitudes in the other hemisphere. Thus the transequatorial wind yields hemispheric asymmetry in plasma distribution off the equatorial plane.

There are some efforts to investigate the ionospheric instability taking the contribution of plasma away from the equatorial plane into consideration. HAERENDEL (1973) derived a growth rate of the Rayleigh-Taylor instability in terms of an upward gradient of the integrated ion content for O^+ within the magnetic flux tube. Ambient electric fields are neglected in the derivation. ZALESAK *et al.* (1982) developed a three-layer model for numerical simulations of the effects of neutral winds and background Pedersen conductivity. Their layer 2 represents an equatorial plane and layers 1 and 3 simulate the E layer away from the equatorial plane. Three layers are electrically connected with each other via a conducting magnetic field line. For the purpose of the present study, we will derive a multilayer model of the linear growth rate for the Rayleigh-Taylor and the $\boldsymbol{E} \times \boldsymbol{B}$ drift instability involving plasma in the entire

magnetic flux tube, which may be considered as an extension of the linear three-layer model described by ZALESAK *et al.*

1.2. Scope of the present work

In Chapter 2 a comprehensive data set of topside spread F by the ISS-b satellite is presented and global morphology of spread F based on the observations is examined. Section 2.2 gives an outline of the experiment including engineering parameters and orbital conditions relevant to the analyses. One of the advantages of the ISS-b ionosonde is the digital ionograms. To keep the standard for the identification of spread F being constant, spread F is determined by a computer processing, which procedure is described in section 2.3. For preliminary discussion, worldwide distribution of topside spread F is presented in section 2.4. Section 2.5 focuses spread F in the equatorial region between 30°N and 30°S, which is a major interest in this thesis. An important characteristic of ESF presented in this section is a combined seasonal and longitudinal variability of its activity; we call it the seasonal-longitudinal effect of ESF. In section 2.6 in-situ ionospheric irregularities at the satellite heights, i.e., plasma bubbles and plasma blobs, are examined. Those irregularities are considered to be a direct evidence of the plasma instability responsible for the generation of ESF.

In Chapter 3 large-scale ionospheric structure is discussed in connection with the seasonal-longitudinal effect of ESF. So far longitudinal effects of ESF irregularities have been discussed to some extent based on limited data sets. However, it is shown that none of these mechanisms explains the seasonal-longitudinal effect of ESF found in Chapter 2. To find an alternative mechanism controlling the seasonal-longitudinal effect of ESF, the background ionosphere is examined in section 3.2. The results are interpreted in terms of transequatorial thermospheric winds, which cause the interhemispheric plasma flows, in section 3.3. In section 3.4 a possible connection between the large-scale ionospheric structure and plasma instability is discussed; it is proposed that the redistribution of plasma along the magnetic field line due to the

transequatorial winds suppresses the growth of the plasma instability through the increase of field line integrated Pedersen conductivity.

Chapter 4 numerically elaborates the mechanism of the seasonal-longitudinal effect of ESF proposed in Chapter 3. For this purpose a diagnostic model is developed including contribution of the plasma away from the equator. In section 4.2 theoretical expression of non-local plasma instability model is derived. Section 4.3 describes numerical computations and models for the neutral winds and electric fields. In section 4.4 computational results show an appreciable effect of neutral winds on the generation of ESF, and at the same time, zonal electric fields have an equally important effect on ESF.

Chapter 5 discusses two more features related with ESF; one is the latitudinal extent of the ESF region, and the other is the density enhancements or plasma blobs observed at the satellite heights associated with ESF irregularities. In section 5.2 latitudinal extent of the equatorial irregularities is briefly reviewed based on published materials. Section 5.3 applies the diagnostic model developed in Chapter 4 to the magnetic field configuration at midlatitudes. The computational results are compared with observations in section 5.4. Further, the generation mechanism of plasma blobs is attributed to the $\boldsymbol{E} \times \boldsymbol{B}$ instability.

Chapter 6 summarizes the conclusion of the present work.

Chapter 2: Topside Spread F Observed by ISS-b

2.1. Introduction

It has long been known that appearance of spread F varies with local time, season, geographical location, and many other geophysical conditions (SHIMAZAKI, 1959; HERMAN, 1966). Nevertheless global picture was not been completely known. There may be two major difficulties in studying global morphology of spread F based on the bottomside sounding. The first is the limited number of ionosonde stations, and furthermore they distribute unevenly over the world; locations of the station are limited in continents and islands. In particular, at the equatorial latitudes, stations are scarce because of the Pacific and Atlantic Oceans. The second is the lack of reliability of spread F information which cannot be removed by statistical procedure. Usually, spread F can be determined from the letter "F" in the monthly tabulation of the ionospheric critical frequency, f_oF_2, issued by local organizations independently. There is, however, no quantitative standard to scale spread F. Historically, the scaling of ionospheric parameters has been devoted to engineering interests for the short wave communications, for which the ionospheric critical frequency is the most important parameter and the spread F information attached to the scaled f_oF_2 value is considered to be a subsidiary parameter to provide the quality of the f_oF_2 value. Thus it is almost impossible to compare the spread F activity at different stations.

The above difficulties were resolved to some extent by the launch of the topside sounding satellites, Alouette 1, 2, ISIS 1, and 2, but still data were restricted in the limited areas over which the satellite is visible from the telemetry station. The fifth topside sounding satellite, ISS-b (Ionosphere Sounding Satellite -b), was launched on February 16, 1978 by Japan. This satellite carries an onboard tape recorder that is able to store ionograms observed during whole revolution period of the satellite orbit. Four revolutions of observation in a day are chosen so that the longitudes of the data points may be distributed uniformly.

In this chapter morphological features of spread F are examined on the basis of the ISS-b observations. At first, in section 2.2, an outline of the ISS-b topside sounding including engineering parameters and orbital conditions is presented. One of the advantages of the ISS-b ionosonde is the digital ionograms. As mentioned before, it is important to keep the standard for the scaling of spread F being constant. Spread F is determined by a computer processing, which procedure is described in section 2.3. For preliminary discussion, worldwide distribution of topside spread F is presented in section 2.4. Section 2.5 focuses equatorial spread F (ESF), which is the major interest in this thesis. In section 2.6, in-situ ionospheric irregularities at the satellite heights, i.e., plasma bubbles and plasma blobs, are examined. Those irregularities are considered to be a direct evidence of the plasma instability responsible to the generation of ESF irregularities in the topside ionosphere.

2.2. Outline of the experiments

2.2.1. The ISS-b satellite The experimental studies that will be described in Chapters 2 and 3 are based on the observations by the topside sounding satellite, ISS-b. The ISS-b satellite was launched on February 16, 1978, and has been operated till the end of 1980 on a routine basis. Four major experimental instruments were aboard the satellite: topside sounder, ion mass spectrometer, retarding potential analyzer, and fixed-frequency radio noise receivers. The topside sounder is designed to detect the critical frequency of the underlying ionospheric F_2 layer with the aid of an onboard pre-programed logic circuit and to observe the virtual range versus frequency characteristics in the swept-frequency mode, i.e., topside ionograms. The data obtained by the swept-frequency ionosonde mode of topside sounder are analyzed in this study. Hereafter we call the swept-frequency mode operation simply topside sounding.

The four experiments were conducted as a time sharing way with 64 second repetition period, and data were stored in an onboard magnetic tape recorder for

about one orbital period. The data store mode operations were performed at four times a day; orbits were selected so that the longitudes of the data points may be distributed uniformly on the whole earth by using onboard timer that controls the start time of the observation. The operation of data store mode for four whole-rotational periods a day is a great advantage compared with the other four topside sounder satellites launched previously, Alouette 1, 2, ISIS 1, and 2, because data obtained by those satellites were limited in the areas in which the satellite is visible from the telemetry station on the ground.

2.2.2. Parameters of the topside sounder Spread F presented in this thesis is based on the ionogram data which were digitized on the spacecraft for the benefit of efficient storage of the data by the onboard tape recorder and efficient processing of the data by a computer at the ground. The sounding frequency was swept stepwise from 0.5 MHz to 14.8 MHz in 16 sec with a frequency increment of 0.1 MHz. The received signal strengths at each frequency step were sampled in every 33.3 km virtual range increment over the range from 0 km to 1333.3 km. The intensity of each sampled signal was quantized into four levels or two bits, i.e., 0, 6, 12 and 18 dB above the receiver noise level. Thus one ionogram is constructed by segments at 40 virtual ranges and 144 frequency steps. The engineering parameters relevant to the interpretation of the data are summarized in Table 2.1.

Shown in Figure 2.1 are typical examples of reconstructed ionogram with normal echo traces (top) and spread F traces (middle and bottom). The strength of the echo at each elementary segment of the ionogram, 0.1 MHz in frequency and 33.3 km in virtual range, is represented by "|", "×", and "+" for the levels corresponding to 6, 12, and 18 dB above the background noise level, respectively. In the upper panel, an ionogram without spread F, the extraordinary mode echo starts at ~2.3 MHz, and some resonance spikes and the extraordinary Z-mode trace are observed as vertical wedge-like portions at the frequency lower than 2.3 MHz, although they are not eas-

TABLE 2.1. System Parameters of the ISS-b Satellite

Swept-Frequency Sounder	
Frequency Coverage	0.5 to 14.8 MHz (0.1 MHz step)
Frame Time	16 sec
Frame Rate	64 sec^{-1}
	Time Sharing with Other Experiments
Transmitter Power	150 W
Pulse Width	300 μsec
Pulse Repetition Rate	9 sec^{-1}
Sampling of Echo Signals	33.3 km in Virtual Range
Quantization of Echo Signals	0, 6, 12, and 18 dB
	Above the Background Noise Level
Overall Bandwidth of the Receiver	6 kHz
Orbital Parameters	
Perigee	972 km
Apogee	1220 km
Inclination Angle	70°
Period	107 min
Spin Rate	13.6 rpm

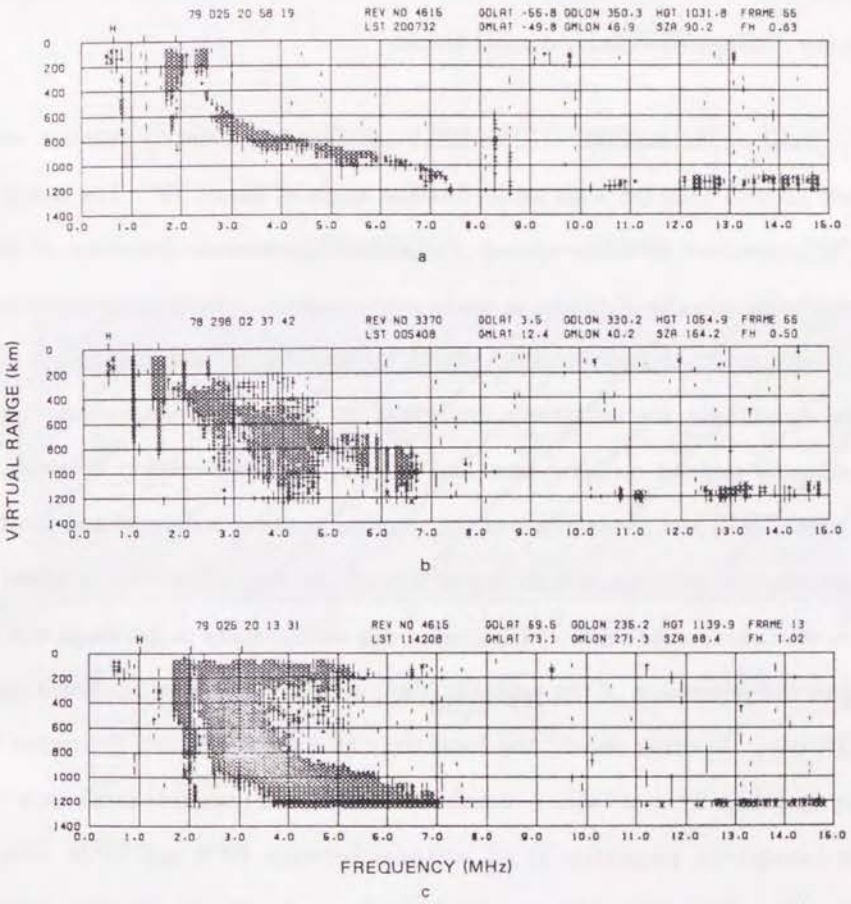

Fig. 2.1. Typical examples of ISS-b ionogram: no spread F configuration (upper panel); spread F ionogram near the equator (middle panel); and spread F ionogram at high latitude (lower panel). The intensity of the echo is expressed with three different characters, "|", "×", and "+" for the levels corresponding to 6, 12, and 18 dB above the background noise level, respectively.

ily distinguished each other from the ionogram information alone. The distinction between the ordinary and extraordinary mode traces is also difficult even in the case of no spread F traces. However, it is no matter for the study of spread F because spread F echoes are sufficiently wide as shown in the middle and bottom panels, and are easily distinguished from normal traces.

2.2.3. Orbit of the satellite The ISS-b satellite has a nearly circular orbit at an altitude around 1100 km with an inclination angle of about 70°. The nearly circular orbit is convenient to study spread F, because the remote detection of the spread F irregularities in the F region is made with constant sensitivity everywhere during the whole rotational period. The orbital parameters are summarized in Table 2.1. Orbital conditions are extremely important to investigate ionospheric phenomena that strongly depend on local time and season. The relationship between the local solar time (LST) and the latitude of the satellite position is determined by the orbital parameters, and varies as a function of day of the year. The orbital plane of ISS-b rotates westwards at the rate of 3 degrees a day with respect to the earth-sun direction owing to the precession of the orbit (2°/day) and the motion of the earth around the sun (1°/day). In other words, the local time at a given latitude decreases by about 12 min in a day. Thus it takes 4 months to observe the complete local time variations of the ionospheric properties at all latitudes between 70°S and 70°N. The diagram showing the relationship between the latitudes and LST for the first 1-year period from the launch is given in Figure 2.2.

2.3. Computer scaling of spread F

Evaluation of spread F for a large number of ISS-b topside ionograms was carried out directly from the raw digital data, i.e., without transformation of the data into an ionogram pattern and therefore without judgment of spread echo by eye. This method made it possible not only to improve efficiency in the data processing but also to

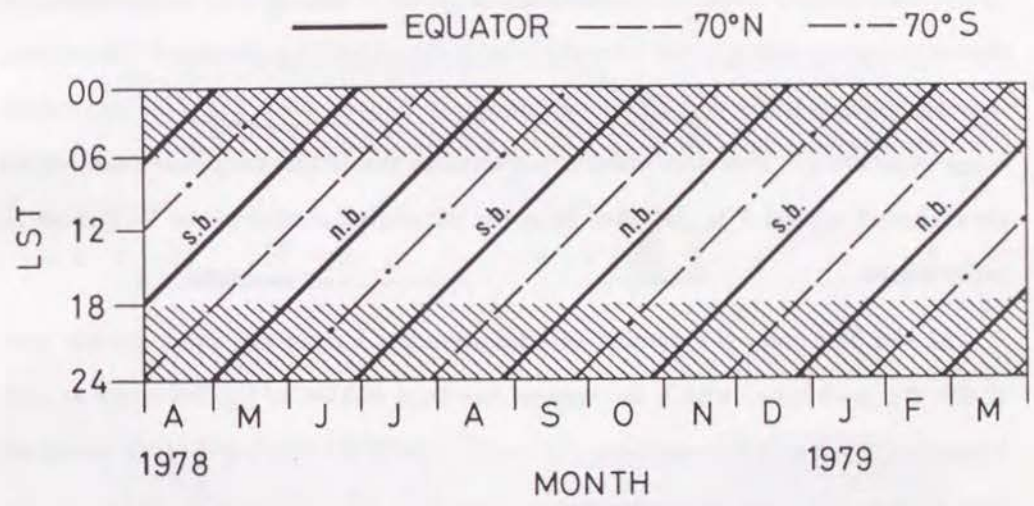

Fig. 2.2. Time chart indicating the local solar time (LST) at the satellite as a function of day of the year. Only the first one year from the launch is shown. The slanted lines indicate latitude of the satellite; the equator (heavy line), 70°N (dashed line), and 70°S (dash-dotted line). The satellite trajectory on a given day is parallel to the vertical axis and upward. The letter "**s.b.**" means that the satellite crosses the equator from north to south (southbound), and "**n.b.**" does from south to north (northbound). The shaded portions indicate nighttime.

eliminate inequality in the criteria for the manual identification by individuals, which sometimes encounters when bottomside spread F at different stations are compared. The procedure for the identification of spread F from the ionogram data is described below.

As noticed in the ionograms shown in Figure 2.1, most segments corresponding to the interference have the intensity level less than 12 dB or indicated by the symbol "|", while ionospheric echoes and resonance spikes have the intensity level greater than 12 dB. To eliminate errors in identification of spread F arising from interferences the segments corresponding to the intensity greater than 12 dB are examined. Sometimes, resonance spikes and a part of the extraordinary Z-mode trace near the zero virtual range cause errors. Therefore the echo segments at the virtual range less than 400 km are excluded; spread F is identified from the horizontal portion of the O- and/or X-mode traces.

At the first step, the number of echo segments having the value greater than 12 dB, N_i, is obtained within the vertical line from 400 km to the full range at each frequency. A series of the numbers, $N_i (i = 1, \cdots, 144)$, for one frame of the ionogram gives a spectrum covering the frequency range from 0.5 to 14.8 MHz, where the frequency is given by $(4 + i)/10$ MHz. Examples of N_i are shown by non-shaded area in the lower panels of Figures 2.3*a*-2.3*f* for a variety of ionograms. These primary spectrums would, however, still contain some contributions from signals other than the spread echo, such as long duration signals arising from resonance spikes, vertically-aligned echo traces near the local plasma cutoff, the extraordinary Z-mode trace, and severe interferences. These long duration signals usually appear as sharp peaks in the primary spectrum as seen in Figure 2.3. To eliminate these spike-like undesirable contributions, the number L_i is obtained as follows:

$$L_i = \min (N_{i-j}, \cdots, N_i, \cdots, N_{i+j}), \quad (i = 1, \cdots, 144) \tag{2.1}$$

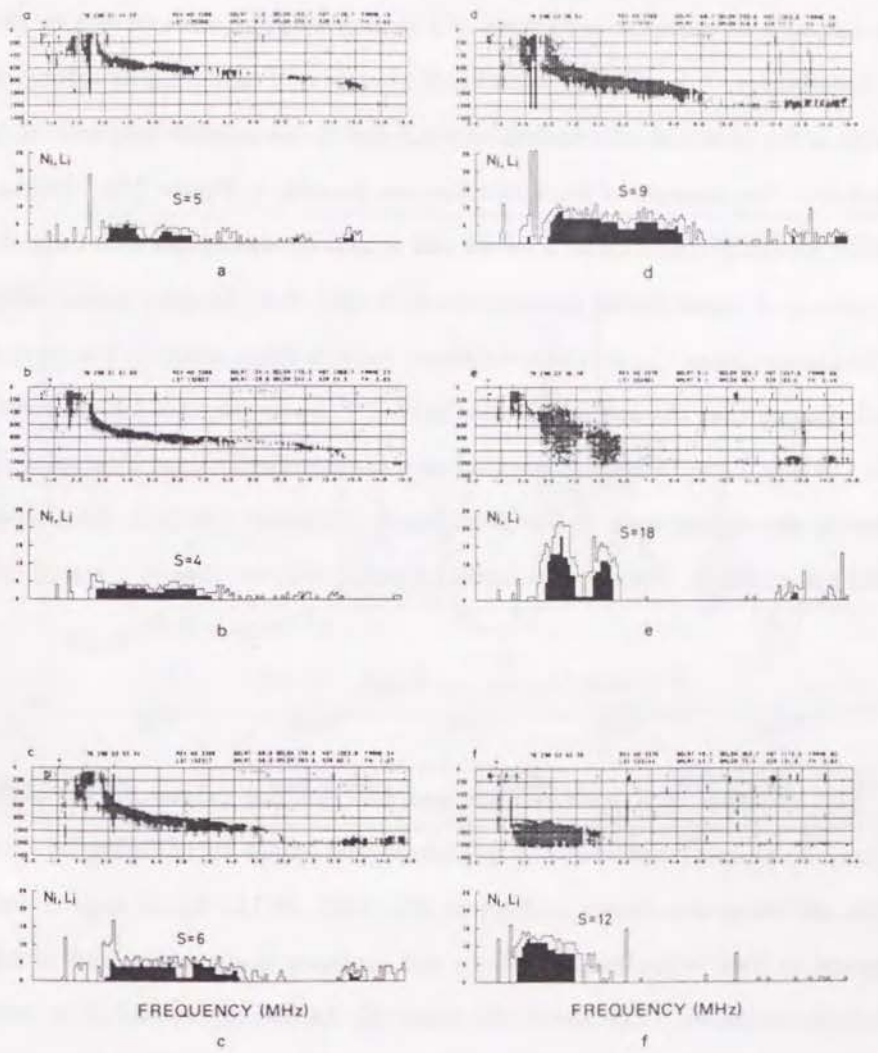

Fig. 2.3. ISS-b ionograms (upper part of each section) and indicators of vertical echo width (lower part of each section); continuous line is N_i, and shaded area is L_i. The six ionograms a to f correspond to the points a to f in Figure 2.4.

where "min" means to take a minimum value for the frequency range $f_d = (2j + 1)/10$ MHz. At the start and end of the series, $1 \leq i - j$ and $i + j \leq 144$, respectively. It is desirable to choose a large value of j to eliminate the error caused by the spike-like distribution of N_i. On the other hand, the effect of signal fading arising from the change in the direction of sounding antenna due to the satellite spin motion must be considered. An example of the spin effect can be seen in Figure 2.3*e*. The ionogram exhibits spread F condition as a whole, but echo trace disappears at 2.4 and 4.3 MHz. The period of signal fading corresponds to 2.1 sec, half the spin period. Therefore, the frequency range, f_d, in which minimum value is taken must be less than half the spin fading so that the spin-modulated spread F traces may not be underestimated. Here $j = 3$ or $f_d = 0.7$ MHz is adopted as a compromised value. Examples of L_i are shown by the shaded areas in the lower panels of Figures 2.3*a*-2.3*f*. Thus undesirable effects are excluded. Finally, the maximum value of L_i is taken as a spread F index;

$$S = \max(L_1, L_2, \cdots, L_{144}), \quad (i = 1, \cdots, 144) \tag{2.2}$$

The variation of S with latitude and LST for one orbital period is shown in Figure 2.4. The six points denoted by alphabetical letters *a*-*f* in Figure 2.4 correspond to the six ionograms shown in Figures 2.3*a*-2.3*f*. In the figure large S values are observed at high latitudes in northern and southern hemispheres, and at nighttime equatorial latitudes. The threshold value, S_0, to identify spread F is empirically determined by cross-examination of ionograms and calculated S values as shown in Figures 2.3 and 2.4 for several passes. The most adequate value of $S_0 = 6$ is adopted in the present analyses, i.e., ionograms with $S \geq 6$ is spread F. The value of S_0 seems somewhat larger than an expected value from the transmitted pulse width of 300 μsec, which corresponds to the virtual range of 45 km or to two elementary resolution segments of the ionogram. This discrepancy may partly be ascribed to the splitting into the ordinary and extraordinary traces, both traces are included in the

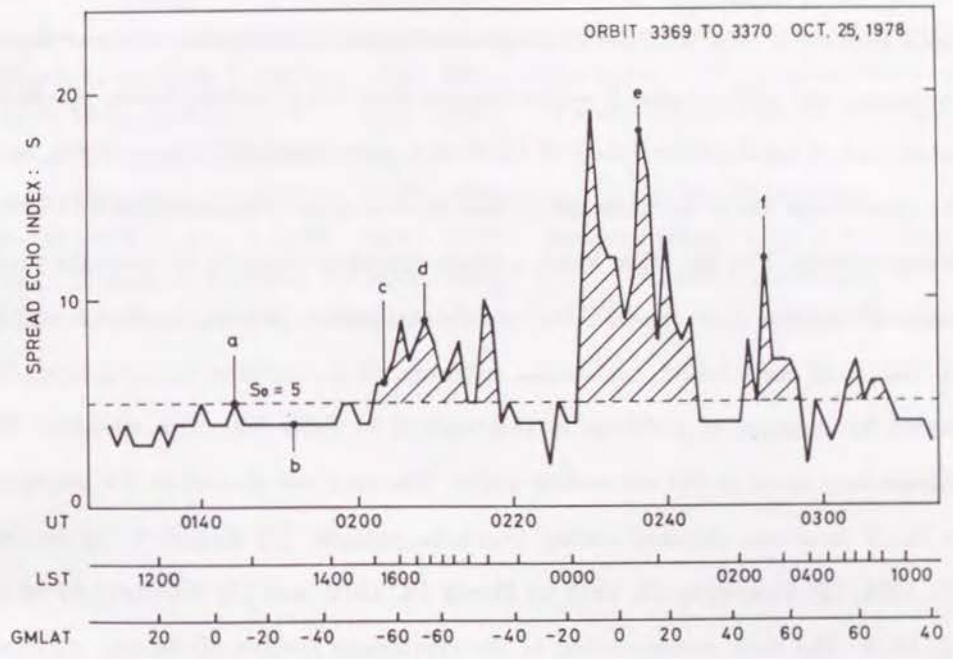

Fig. 2.4. Variation of the spread F index, S, along the satellite path for one orbital period. The ionograms corresponding to the points indicated by letters *a* to *f* are shown in Figure 2.3. The shaded areas, $S \geq 6$, denote spread F at high latitudes in both hemispheres and nighttime equatorial latitudes.

evaluation of N_i and therefore S, and partly be caused by pulse broadening due to instrumental effects in the receiver.

2.4. Worldwide characteristics of spread F

2.4.1. Latitudinal and local time variations The occurrence of spread F exhibits strong dependence on both local time and latitude. In fact, in Figure 2.4, the large S value appears at high latitudes and nighttime-equatorial latitudes, while at daytime-equatorial and midlatitudes S values are less than the threshold value. As we have mentioned in 2.2.3 the local time of ISS-b at a given latitude changes slowly so that the observation has to be continued at least for 4 months to examine the LST-latitude characteristics. On the other hand, a short period is desirable to separate possible seasonal variation from the LST-latitude characteristics. During the first 1 year from the launch of the satellite, continuous operation of the satellite was sometimes interrupted by engineering problems as summarized in Table 2.2. This situation didn't change very much in the succeeding years. The analyses in section 2.4 are devoted to the 3 data sets obtained during 4-months periods: (1) August 11 to December 11, 1978, (2) November 10, 1978 to March 12, 1979, and (3) February 13 to June 13, 1979. The data corresponding to the overlapped portion of the two consecutive periods were doubly used for the two sets.

Latitude and LST variations were examined by calculating occurrence probability of spread F as a ratio of the numbers of spread F ionograms and all ionograms in a small rectangular cell with increments of 10° in magnetic latitude and 1 h in local solar time. Figure 2.5 shows a contour diagram of percentage occurrence of spread F for the August-December period. There are high occurrence regions at the higher latitudes and low latitudes around the magnetic equator. The occurrence of spread F at the equatorial latitudes is confined mostly to the nighttime except for a minor peak at 1000 LST, while the occurrence of spread F at high latitudes extends over all hours. These general characteristics well agree with the previous results by means of Alouette

TABLE 2.2. Operational Status of ISS-b for the 1-st One Year From the Launch

Period	Orbit No.	Status
March 18 to April 1, 1978	404 - 595	Check-Out of the Satellite Missions
April 15 to June 11, 1978	777 - 1553	Normal Observation (4 rev./day)
June 12 to Aug. 10, 1978	-	Interrupted
Aug. 11 to Dec. 13, 1978	2365 - 4035	Normal Observation
Dec. 15, 1978 to Jan. 8, 1979	4056 - 4377	Reduced Observation (1 rev./day)
Jan. 10 to June 13, 1979	4403 - 6480	Normal Observation

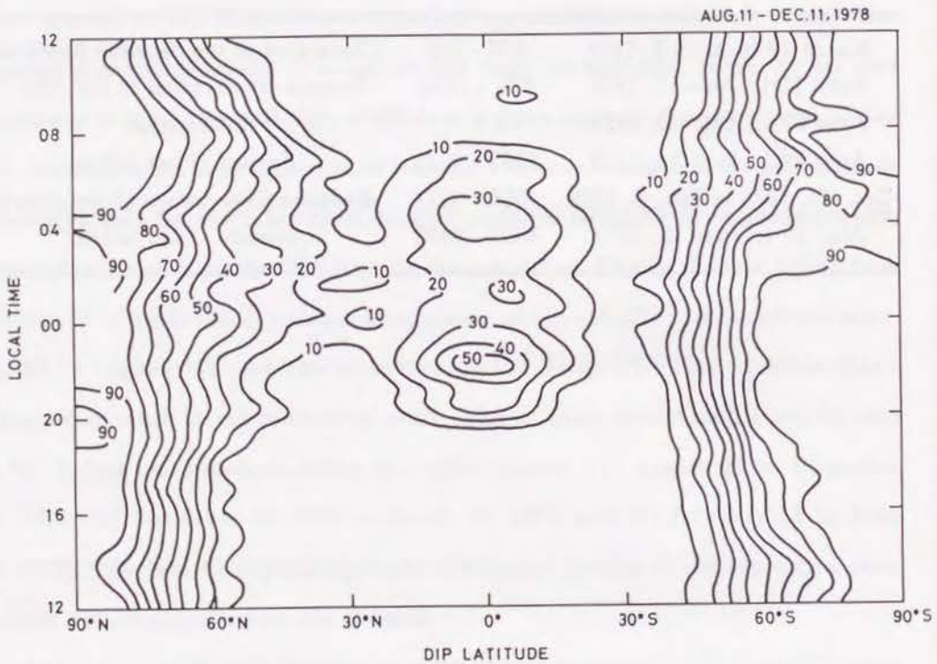

Fig. 2.5. Contour diagram of percentage occurrence of spread F as a function of magnetic (dip) latitude and local solar time for the period from August 11 to December 11, 1978.

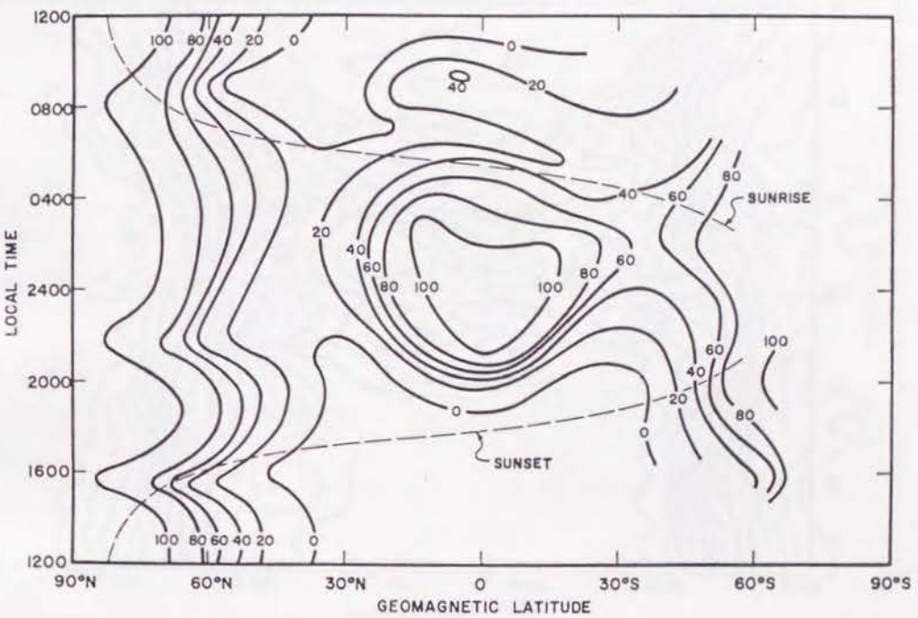

Fig. 2.6. Percentage occurrence of aspect-sensitive scattering echoes derived from the Alouette 1 topside sounder satellite recorded between September 1962 and January 1963 (after CALVERT and SCHMID (1964)).

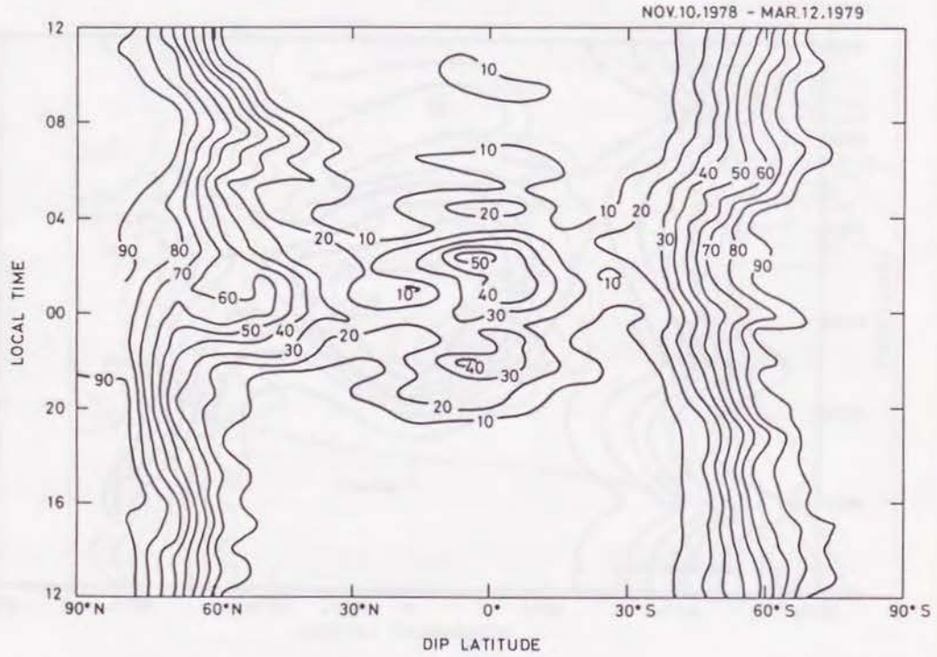

Fig. 2.7. Same as Figure 2.5 but for the period from November 10, 1978 to March 12, 1979.

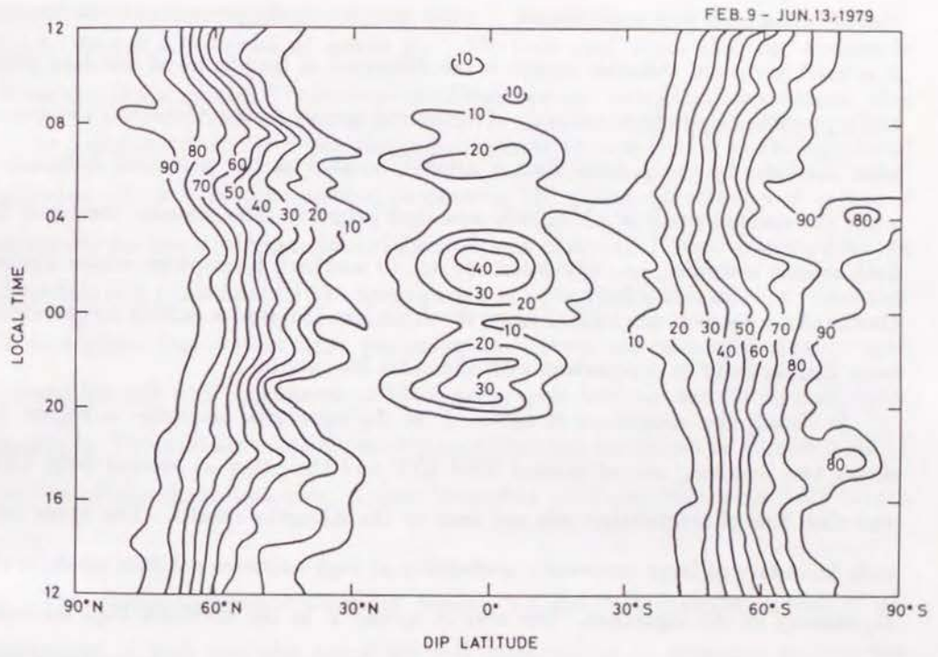

Fig. 2.8. Same as Figure 2.5 but for the period from February 9 to June 13, 1979.

1 topside sounder as reproduced in Figure 2.6 (CALVERT and SCHMID, 1964). The resemblance between Figures 2.5 and 2.6, in turn, implies that the procedure used for the determination of spread F in the present study works well.

Although Figures 2.5 and 2.6 resemble each other, there exists a quantitative difference such as the large occurrence probability in Figure 2.6 compared with ISS-b observations. This may be partly due to the difference in the method of spread F identification such that weak spread F is not included in the present analysis because it is hard to detect. Another reason is the difference in longitudes of the data point and a possible longitudinal anomaly of equatorial spread F; the Alouette 1 ionograms were obtained by the ground station network located at the American longitudes, while the current result is a longitude averaged property. The seasonal condition for both results is similar, i.e., autumnal equinox to northern hemisphere winter season. During these seasons, as clarified later, the American longitudes exhibit an extremely large ESF activity in comparison with the other longitudes.

In detail, the occurrence of spread F at the equatorial latitudes in Figure 2.5 shows two maxima, one at around 2200 LST and the other at around 0400 LST; and such fine characteristics are not seen in the Alouette results. The lower latitude boundary of large occurrence probability at high latitudes exhibits north/south asymmetry in the nighttime. The area of spread F at the northern high latitudes tends to extend into lower latitudes during nighttime, while that at the southern high latitudes doesn't. The north/south asymmetry was also observed by Alouette 1, but it is reverse to the ISS-b results.

The occurrence diagrams for the other data sets are shown in Figures 2.7 and 2.8. The major features in these diagrams, large occurrence probability in nighttime at equatorial latitudes and during a whole day at high latitudes, are similar to those of the first data set shown in Figure 2.5. Further, at the equatorial latitudes, the enhanced occurrence probability in the premidnight hours is commonly observed at around 2200 LST in the three data sets. While, the maximum in the postmidnight hours varies with the data set or presumably with the season. The steadily observed premidnight enhancement of spread F strongly suggests a connection with the post sunset enhancement of eastward electric field observed with the equatorial incoherent scatter radar facility at Jicamarca, Peru (FEJER *et al.*, 1979). The connection between the occurrence of spread F at the equatorial latitudes and electric field enhancement will be discussed in Chapter 4.

2.4.2. Global distribution of spread F We have seen above that the worldwide characteristics of spread F indicate strong local time and latitudinal dependence. One of the prominent features is the day/night asymmetry of spread F at the equatorial latitudes. Thus it is quite natural to examine the global distribution of spread F separately for day and night. Global distributions of spread F were examined for the same data sets those used for the investigation of latitudinal and local time variations. To draw global distribution maps, percentage occurrence was calculated in every small rectangular cell with increments of 10° in geographic latitude and 30° in geographic longitude. The contour maps of occurrence probability are shown in Figures 2.9-2.12 for two of the three data sets, August-December 1978 and November 1978-March 1979.

The daytime spread F shown in Figures 2.9 and 2.11 indicates spread F enhancement at high latitudes which are well characterized by magnetic latitude but not geographical latitude. The nighttime spread F is shown in Figures 2.10 and 2.12. The high latitude portions of the high occurrence probability are similar to those of daytime distribution. Essentially occurrence probability at high latitudes doesn't change very much in season and local time.

At low latitudes, the latitudinal variation of spread F shows maximum occurrence probability at the magnetic equator, indicated by the dashed line, irrespective of the deviation of the magnetic equator from the geographic equator. In contrast to high latitudes, spread F at the equatorial latitudes drastically varies with the lon-

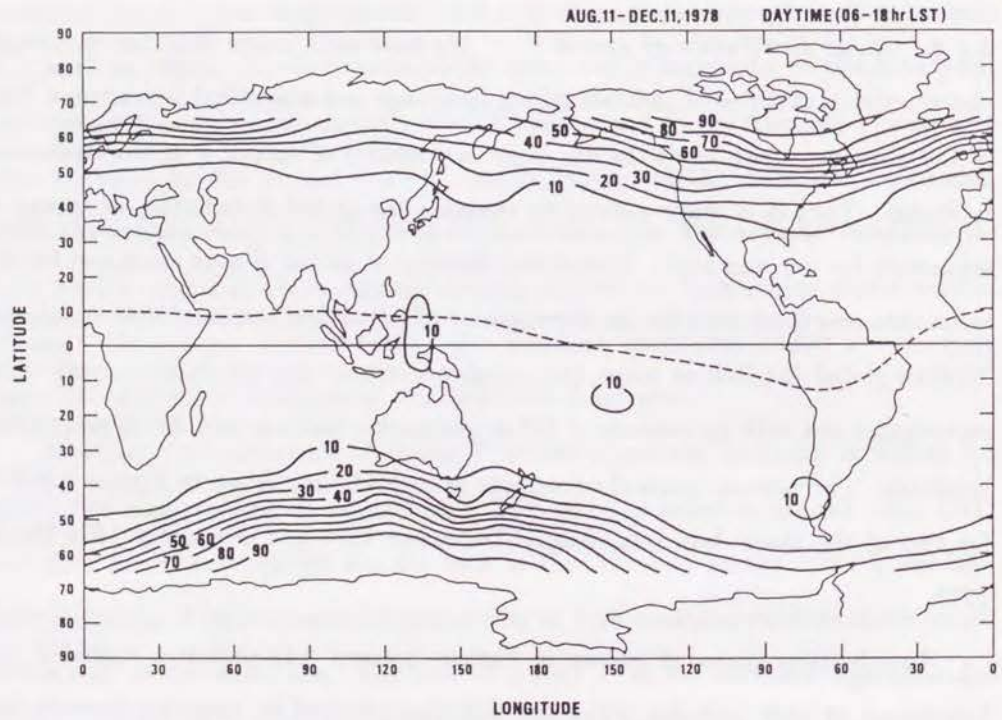

Fig. 2.9. Global distribution map of percentage occurrence of daytime spread F for the period from August 11 to December 11, 1978. The dashed line indicates the magnetic equator.

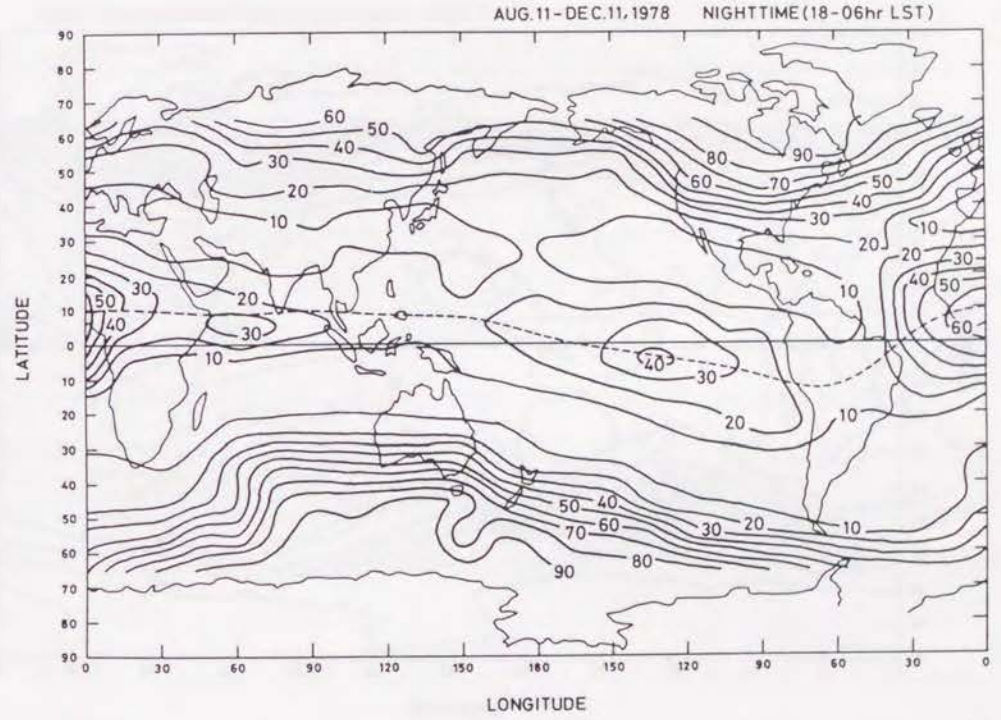

Fig. 2.10. Same as Figure 2.9 but for nighttime spread F.

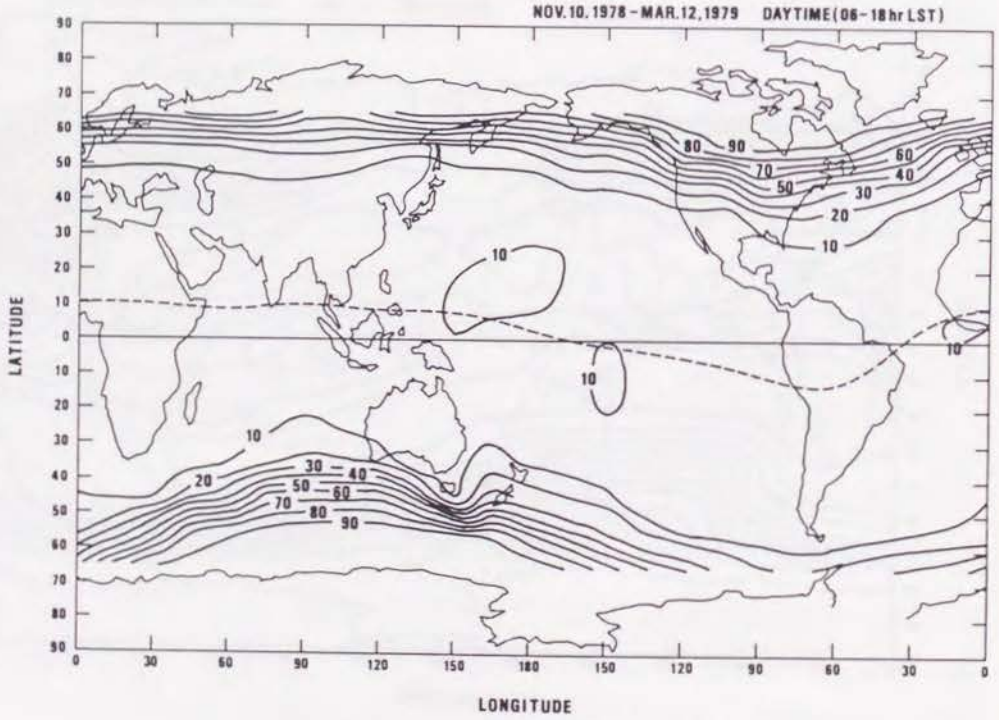

Fig. 2.11. Global distribution map of percentage occurrence of daytime spread F for the period from November 10, 1978 to March 12, 1979.

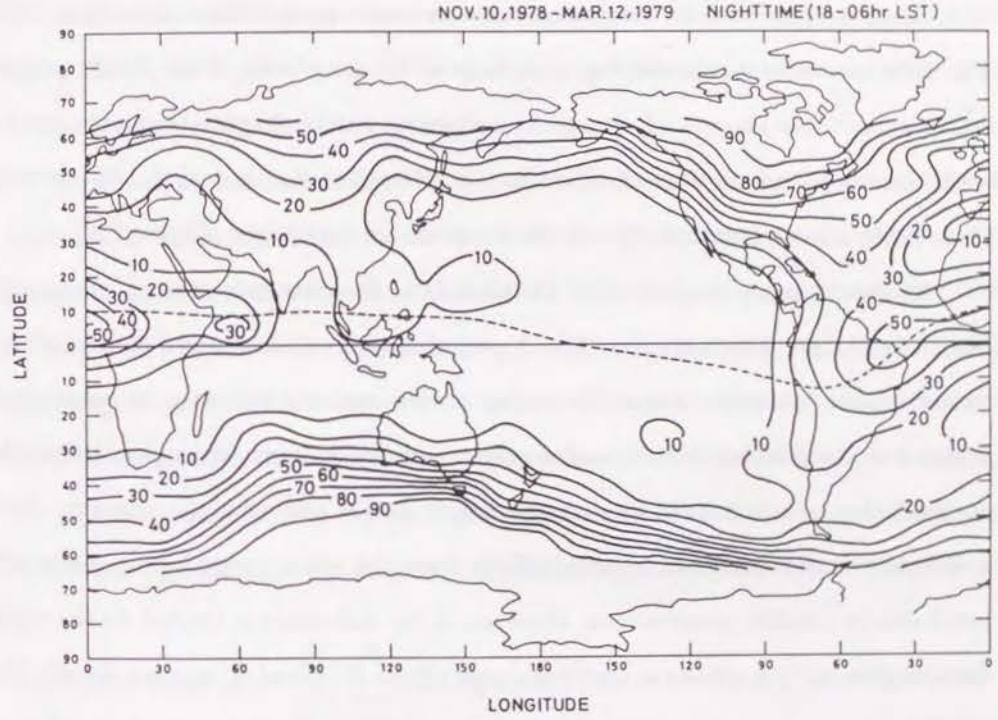

Fig. 2.12. Same as Figure 2.11 but for nighttime spread F.

gitude. In Figure 2.10 the August-December period, enhanced spread F regions lie at around 0° and 130°W longitudes. The maximum occurrence probability is greater than 60% at 0°, and 40% at 130°W, while the occurrence probability between these regions decreases to <20%. The longitudinal dependence of spread F at the equatorial latitudes is more exaggerated in the case of Figure 2.12, the November-March period, such that the maximum occurrence probability at 50°W-10°E is higher than 50%, while at 130°E-90°W longitudes the occurrence probability is less than 10%. The difference between the two figures is large at the longitudes of the Pacific region, where appreciable amount of spread F is observed in the August-December period while almost no spread F is observed in the November-March period. Apparently, there exists a large seasonal effect in the longitudinal variability of spread F.

We should note, however, that the periods of the data sets are not necessarily selected suitably. The November-March period may be characterized as a northern winter season, while the August-December period contains not only an equinoctial season but also northern winter and northern summer seasons: We suppose that the equinoctial season is defined as each one month before and after the equinox. Such a difficulty in separation of seasonal effects from the other properties is essentially inevitable in satellite observations. However, if the discussion is limited to the equatorial region, we are able to examine seasonal effects of spread F in more detail. The satellite crosses the equator twice during one revolution; northbound and southbound passes separated by 12 hours in local time at the equator. Thus observation for a given local time condition can be made every two months alternately for northbound and southbound passes as shown in Figure 2.2. In the next section we will focus on the combined seasonal and longitudinal effects of spread F at the equatorial latitudes.

2.5. Equatorial spread F

2.5.1. Mapping analysis of equatorial spread F Quite interesting seasonal and longitudinal dependence of spread F at equatorial latitudes (equatorial spread F or

ESF) was found above; hereafter discussion is focused on the equatorial region. In the previous section spread F is discussed in terms of occurrence probability that is defined by the ratio of the numbers of ionograms with spread F traces and all ionograms in a small area. Such occurrence probability is easy to interpret since the definition is primitive. In return to this, to obtain reliable results, sufficient number of ionograms are needed in each small area in which the ratio is calculated, and therefore we are not allowed to divide the data set into subsets with short period. To avoid this problem, strength of spread F is dealt, and functional representation is adopted for the longitudinal distribution of equatorial spread F.

Our analysis was carried out with respect to 11 data groups for the annual periods indicated in Table 2.3. The local solar time in the equatorial region for the first five groups (*a*-*e*) in the table covers 1800 to 2400 LST and the last six groups does 0000 to 0600 LST. In the table, one data group which should correspond to the period July-August and should lie between the groups of *b* and *c* is missing because of scarce available data owing to an unsatisfactory operational condition of the spacecraft.

The functional form to represent the global distribution of the spread F activity, $\mathcal{F}$, is defined by the spherical harmonic expansion as follows (MATUURA *et al.*, 1981):

$$\mathcal{F}(\lambda,\phi) = \mathcal{F}'(\theta^*,\phi) = \sum_{m=0}^{M}\sum_{n=m}^{N}[A_{nm}P_n^m(\cos\theta^*)\cos m\phi + B_{nm}P_n^m(\cos\theta^*)\sin m\phi] \tag{2.3}$$

where λ and ϕ are the geographic latitude and longitude, respectively, and θ^* is the modified colatitude defined as

$$\theta^* = \cot^{-1}\frac{I(\lambda,\phi)}{\sqrt{\cos\lambda}} \tag{2.4}$$

with the magnetic dip angle I. The contours of constant modified colatitude are dense and parallel to those of constant dip angle near the magnetic equator as shown

TABLE 2.3. Annual Periods of the Data Groups for ESF Study

Group	1978	1979	1980
		Premidnight (1800-2400 LST)	
a	...	Feb. 21 - March 29	Feb. 15 - March 22
b	April 27 - June 3	April 22 - May 26	April 16 - May 23
c	Aug. 24 - Oct. 2	Aug. 20 - Sept. 27	Aug. 18 - Sept. 14
d	Oct. 25 - Dec. 2	Oct. 20 - Nov. 26	Oct. 15 - Nov. 19
e	Dec. 23 - Jan. 28, 1979	Dec. 18 - Jan. 23, 1980	...
		Postmidnight (0000-0600 LST)	
f	...	Jan. 20 - Feb. 26	Jan. 16 - Feb. 22
g	...	March 22 - April 27	March 18 - April 23
h	May 29 - June 15	May 23 - June 13	May 17 - June 20
i	Aug. 11 - Sept. 1	Aug. 6 - Aug. 27	Aug. 1 - Aug. 12
j	Sept. 24 - Nov. 2	Sept. 23 - Oct. 27	Sept. 27 - Oct. 20
k	Nov. 25 - Dec. 30	Nov. 19 - Dec. 25	Nov. 13 - Dec. 15

in Figure 2.13. Since the occurrence probability of equatorial spread F is usually symmetric with respect to the magnetic equator, as we have seen in section 2.4, the modified colatitude may be pertinent coordinate for the representation of equatorial spread F characteristics. The notation $P_n^m(x)$ denotes the Legendre's associated function with order n and degree m of the argument x. The coefficients A_{nm} and B_{nm} in the equation are to be determined by least-square fitting of the functional values to the global data of spread F strength. We have already determined quantitative measure for width of echo traces, S, by equation (2.2). For the functional fitting, values exceed the threshold value, $S - S_0$, were used as the spread F strength, where S_0 is the threshold value suitably chosen, which is the same as the value chosen in section 2.4, and when a negative value appears, strength is set to 0.

The worldwide analyses of the occurrence probability of spread F have shown that regions of high occurrence are at the higher latitudes in both hemispheres and at the equatorial latitudes, and those regions are separated from each other with intermediate regions of low occurrence probability centered at around 30° in magnetic latitude in both hemispheres as seen in section 2.4, e.g., Figure 2.5. For the mathematical convenience we have artificially put the spread F strength at zero at the magnetic latitudes greater than 30° N and S or $0° < \theta^* < 49.3°, 130.7° < \theta^* < 180°$ in modified colatitude.

The mapping analysis was carried out with the maximum harmonic numbers in equation (2.3) as $N = 7$ and $M = 4$. The distribution maps of the ESF activity for the geographic latitude region between ±40° are shown in Figures 2.14*a*-2.14*k* corresponding to the data groups *a*-*k* in Table 2.3.

2.5.2. Seasonal-longitudinal effect The ESF activity distributions shown in Figures 2.14*d*, 2.14*e*, 2.14*k* are obtained for the northern winter months, and they resemble each other in feature indicating a remarkably high ESF activity at the Atlantic longitudes between 60°W and 0°. It should be noticed that no significant difference in

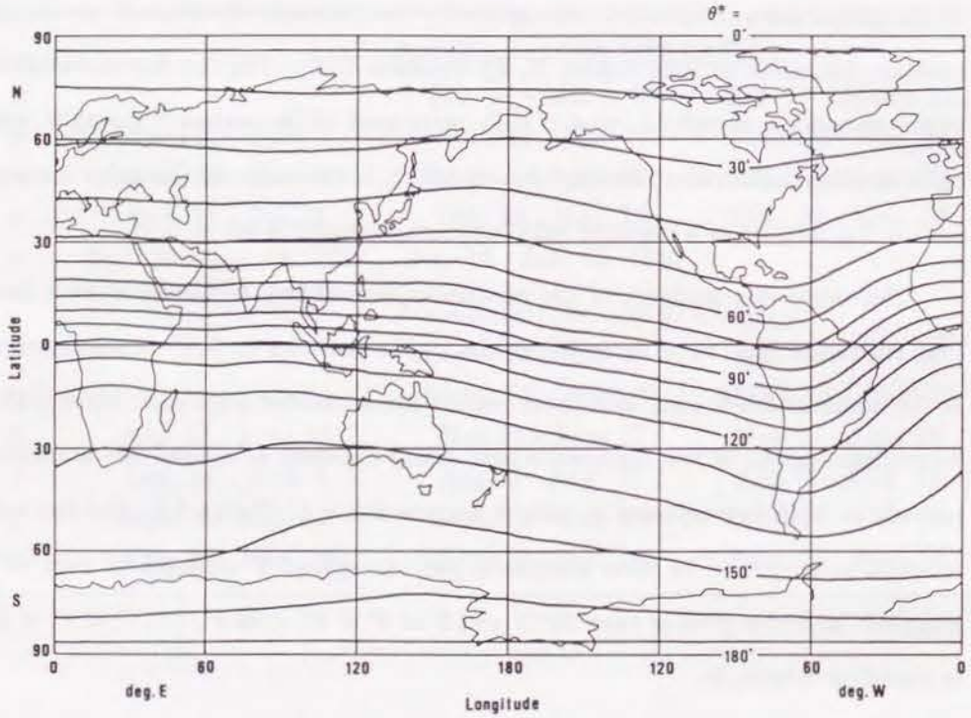

Fig. 2.13. Contours of constant modified colatitude.

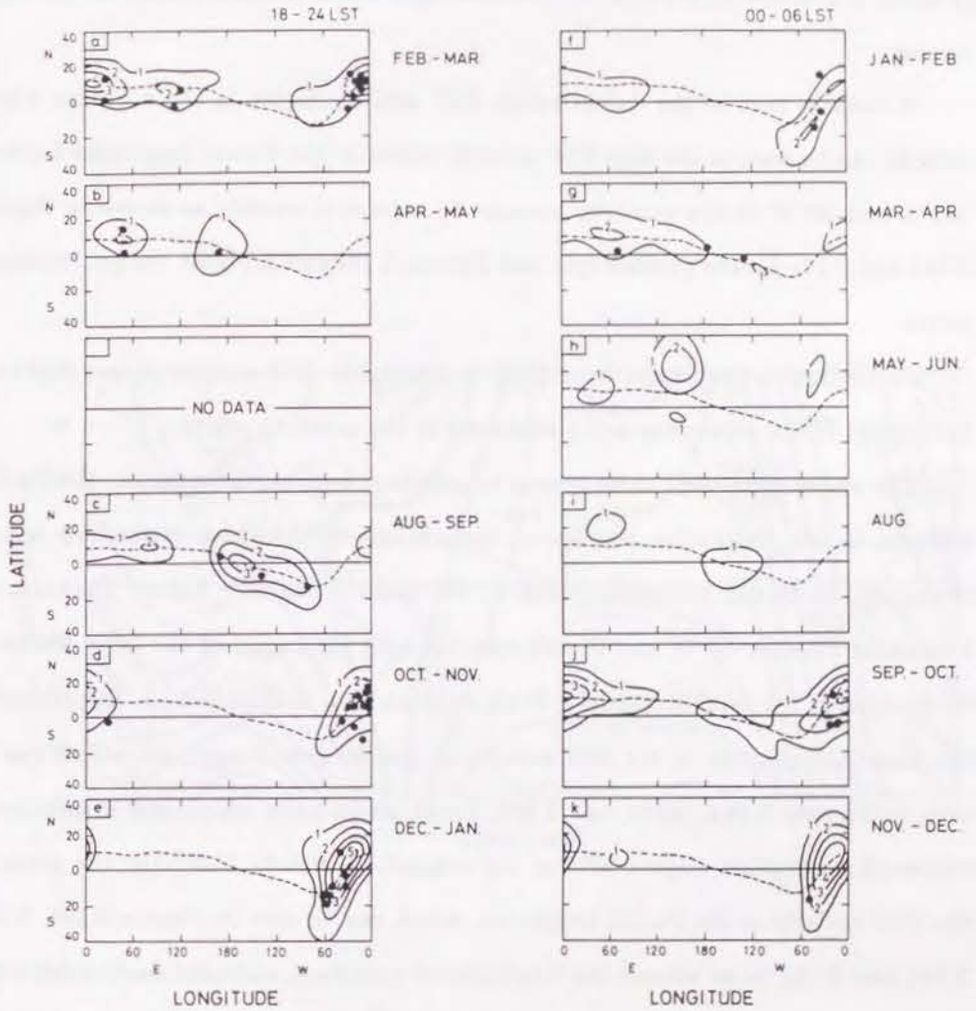

Fig. 2.14. Global distribution maps of ESF activity. Figures 2.14*a* - 2.14*k* correspond to the 11 data groups summarized in Table 2.3. The dashed curve represents the magnetic equator. Positions where plasma bubbles were observed are indicated by dots (for detail see section 2.6).

the longitudinal distributions of the ESF activity is seen between the premidnight (Figures 2.14*d* and 2.14*e*) and the postmidnight hours (Figure 2.14*k*) for the same season.

A counter part to the Atlantic high ESF activity region in the northern winter months can be seen as the high ESF activity region at the Pacific longitudes between 150°E and 90°W in the northern summer to autumnal months as shown in Figures 2.14*b* and 2.14*c* for the premidnight and Figures 2.14*i* and 2.14*j* for the postmidnight hours.

At the Indian longitudes from 60°E to 120°E the ESF activity shows slight enhancement in the equinoxes and a minimum in the northern winter.

The above mentioned three typical longitudinal regions, the Atlantic, the Pacific, and the Indian longitudes correspond respectively to the three distinctive regions characterized by the declination angle of the earth's magnetic fields. The Atlantic longitudes between 60°W and 0° well coincide with the region of the large westward declination of the earth's magnetic fields as illustrated in Figure 2.15. In particular, the longitudinal peaks of the ESF activity at the Atlantic longitudes, which can be seen in Figures 2.14*d*, 2.14*e* and 2.14*k*, lie at around the longitudes of maximum westward declination angle (-20°) at the magnetic equator. Similarly, the peaks of the ESF activity at the Pacific longitudes, which can be seen in Figures 2.14*b*, 2.14*c*, 2.14*i*, and 2.14*j*, lie at around the longitudes of maximum eastward declination angle (10°) at the magnetic equator. On the other hand, the Indian longitudes where the ESF activity tends to be enhanced in the equinoxes correspond to the region of small magnetic declination.

It is also interesting to see the annual variation in the zonal mean ESF activity. Shown in Figure 2.16 is the zonal mean activity at the magnetic equator that is given by $\sum A_{n0} P_n^0(0)$ based on the functional representation of equation (2.3), where the summation is taken for $n = 0, 2, 4$, and 6. In spite of that there exists quite high activity at the Atlantic longitudes in the northern winter, the zonal mean activity

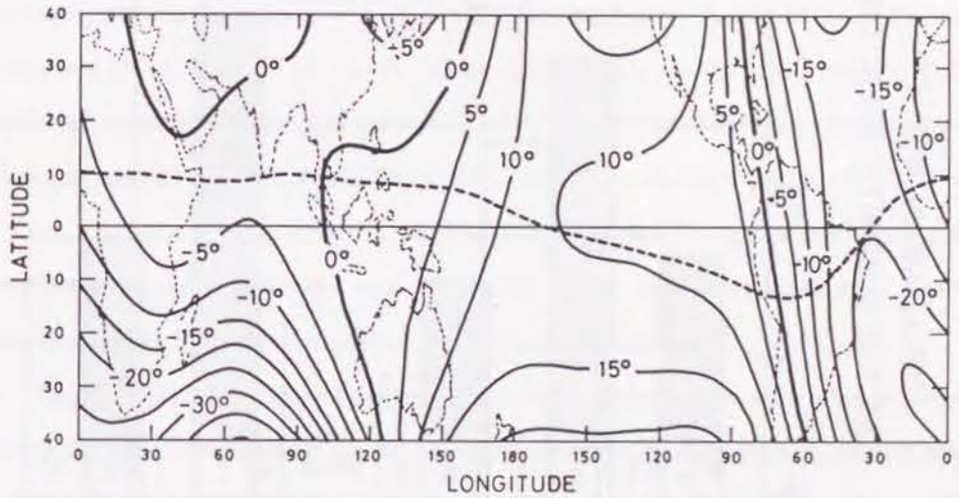

Fig. 2.15. Map of the magnetic declination angle calculated from IGRF 75 model. Positive values denote eastward declination and negative westward declination. Broken curve indicates the magnetic equator.

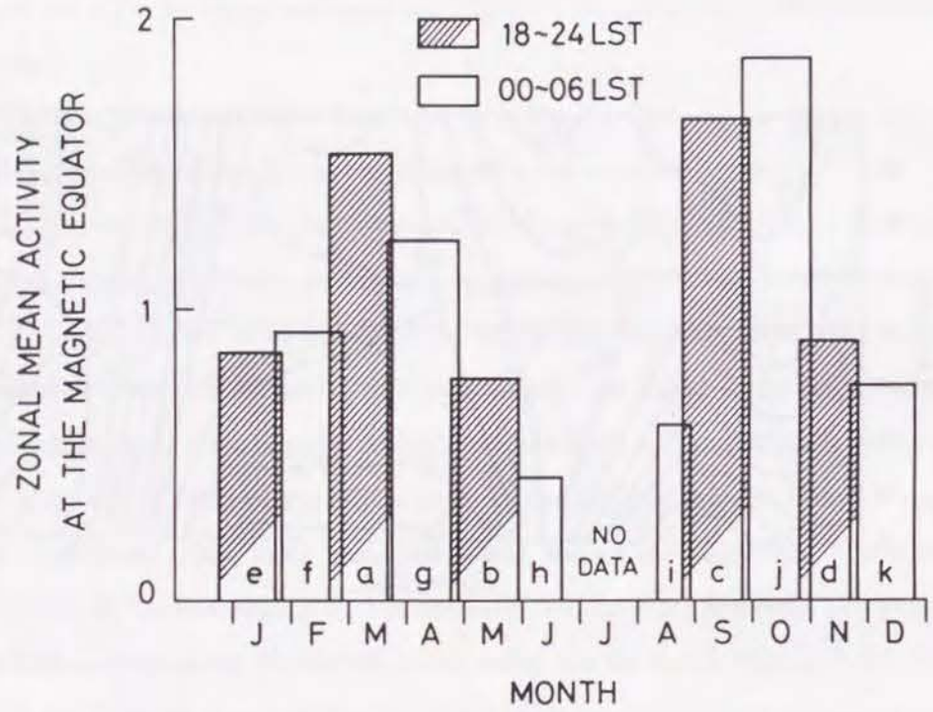

Fig. 2.16. Annual variation of zonal mean spread F activity at the magnetic equator. The mean values were calculated from the functional representation of ESF distribution maps. Width of each bar corresponds to the period of the data group in Table 2.3.

in Figure 2.16 shows maxima at the equinoctial periods. These maxima arise from the longitudinally wide-spread distribution of the ESF activity during the equinoctial periods.

2.6. Irregularities at the satellite heights

2.6.1. Plasma bubbles The most distinctive phenomena related directly to the equatorial spread F are upward moving plume-like structures detected by the radar backscatter observation at Jicamarca, Peru (Woodman and La Hoz, 1976), and the rising plasma bubbles or density depletions detected by the satellite in-situ measurements (McClure *et al.*, 1977). These observations are the manifestation of the nonlinear evolution of the gravitational Rayleigh-Taylor instability in the ionosphere (Kelley and McClure, 1981; Ossakow, 1981). An electron density depletion or a plasma bubble arising from the Rayleigh-Taylor instability grows initially on the bottomside of the F layer and rises up to the topside, producing small scale density irregularities as the source of spread F and radar backscatter.

Usually direct detection of plasma bubbles can be made by satellite-borne plasma probes with sufficient spatial resolution. Although spatial resolution is poor, topside sounders can detect plasma bubbles and provide important information such as a close relation between the plasma depletion and severe spread F at the satellite height due to density irregularities (Dyson and Benson, 1978). Muldrew (1980*b*) observed another feature of plasma bubbles by the Alouette 1 topside sounder, which is aspect sensitive scatter echoes from the bubble below the satellite altitude or remote detection of bubbles.

Plasma bubbles are detected by the ISS-b topside sounder too. Figure 2.17 shows consecutive ionograms indicating spread F traces near the magnetic equator in nighttime. The electron density at the satellite height can be scaled mainly from the cutoff frequency of extraordinary wave. To avoid the ambiguity due to the coarse frequency resolution, 100 kHz/step, the result is reexamined by scaling other plasma parameters

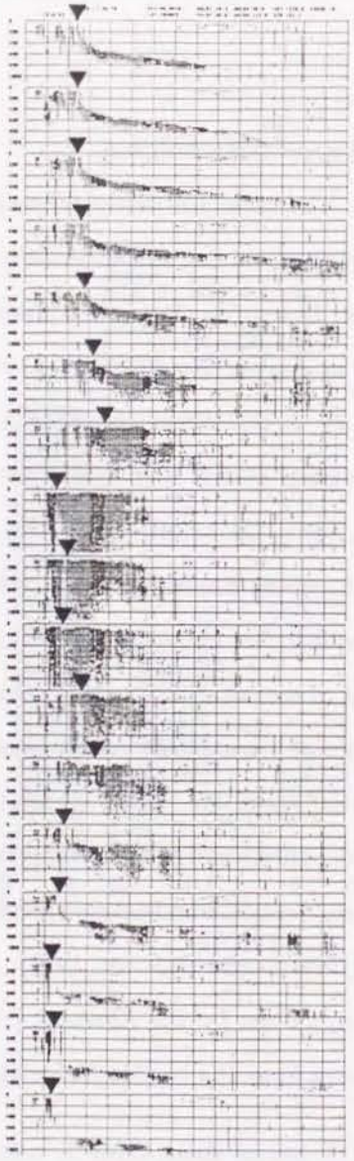

Fig. 2.17 Consecutive ionograms near the equatorial crossing. Cutoff frequencies of the extraordinary wave are shown by triangles at the zero rage.

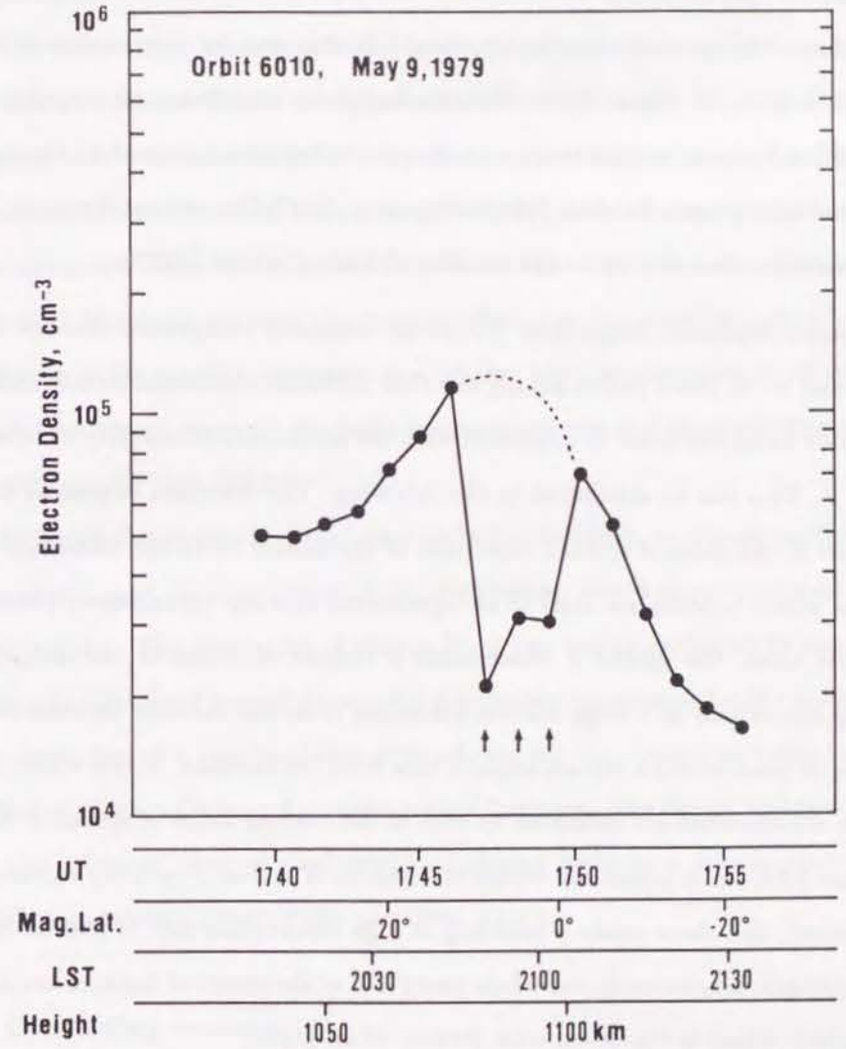

Fig. 2.18. Variation of electron density at the satellite heights determined from the ionograms shown in Figure 2.17.

like ion gyrofrequency, upper hybrid frequency, and model magnetic field strength until consistent results are obtained because these parameters are not independent to each other. The electron density determined in this way for the ionograms in Figure 2.17 is given in Figure 2.18. Density depletions are always accompanied with severe spread echoes at zero range and thought to have been caused by the satellite encounter with plasma bubbles (McClure *et al.*, 1977; Dyson and Benson, 1978), which moved sufficiently up to the satellite altitude of about 1100 km.

Density depletions larger than 30% of the estimated background electron density were found on 46 ISS-b passes among the 1700 nighttime equatorial passes examined. This value looks too small as compared with the occurrence probability of equatorial spread F. This can be attributed to the following: The detection of plasma bubbles is limited to the cases of upward movement of the bubble up to the altitude of about 1100 km where bubbles are close to an equilibrium altitude (Muldrew, 1980*b*). On the other hand, the spread F observation is remote detection of the irregularities existing somewhere in a large volume extending from the satellite altitude down to the F layer peak within a certain angle of view from the satellite. Points where plasma bubbles are observed are indicated by dots in the contour maps of spread F activity in Figure 2.14; those points are within the regions of spread F activity enhancement as expected, and there exists a tendency of high observation rate of plasma bubbles at the Atlantic longitudes in the whole year (70% of the observed bubbles are at these longitudes), which is consistent with Burke *et al.* (1980).

2.6.2. Plasma blobs The density depletions or plasma bubbles are always associated with severe backscatter echoes at zero range, zero range spread F, but the reverse is not true. There are many cases with no appreciable changes in electron density at the satellite height when zero range spread F is observed. This may be interpreted as that the satellite is very close to the plasma bubble but not within it. We discuss here is another case in which zero range spread F is observed in association with density enhancement at the satellite height or a plasma blob. Figure 2.19 is an example of plasma blobs.

The observation of plasma blobs by the ISS-b satellite is quite rare compared with plasma bubbles. This is strongly due to the method used. The frame rate of the ionogram is at one observation in every 64 sec or spatial resolution of 500 km along the satellite orbit. Any small scale density structure at the F region height is thought to be elongated along the magnetic field line. The observed scale of the structure depends on the angle between the magnetic field line and satellite trajectory. Thus the chance of the satellite encounter to a plasma blob, in particular at off-equatorial latitudes with large magnetic dip angle, becomes infrequent if the sizes of plasma blob are much smaller than 500 km.

Although the observation of plasma blobs is infrequent, we should not ignore this phenomenon, and theories of spread F irregularities would never complete without explaining this. The generation of plasma blobs can not be explained by any existing theories. In Chapter 5 we will discuss the mechanism responsible for the plasma blobs as an extension of a non-local theory developed for the equatorial latitudes, which will be described in Chapter 4, to sub-tropical latitudes. The theory will be compared with the extensive observational results of plasma blobs as a plasma probe aboard the Hinotori satellite (Watanabe and Oya, 1986).

2.7. Concluding remarks

The topside ionospheric sounding by the ISS-b satellite first allowed to investigate complete worldwide morphology of spread F. In particular at equatorial latitudes, longitudinal and seasonal dependence of spread F activity could be examined extensively, and we obtained fairly clear picture of a coupled seasonal-longitudinal effect of ESF as follows: During northern winter season the ESF activity is high at the Atlantic longitudes where the geomagnetic fields have large westward declination; during northern summer season the longitudinal peak of ESF activity moves to the

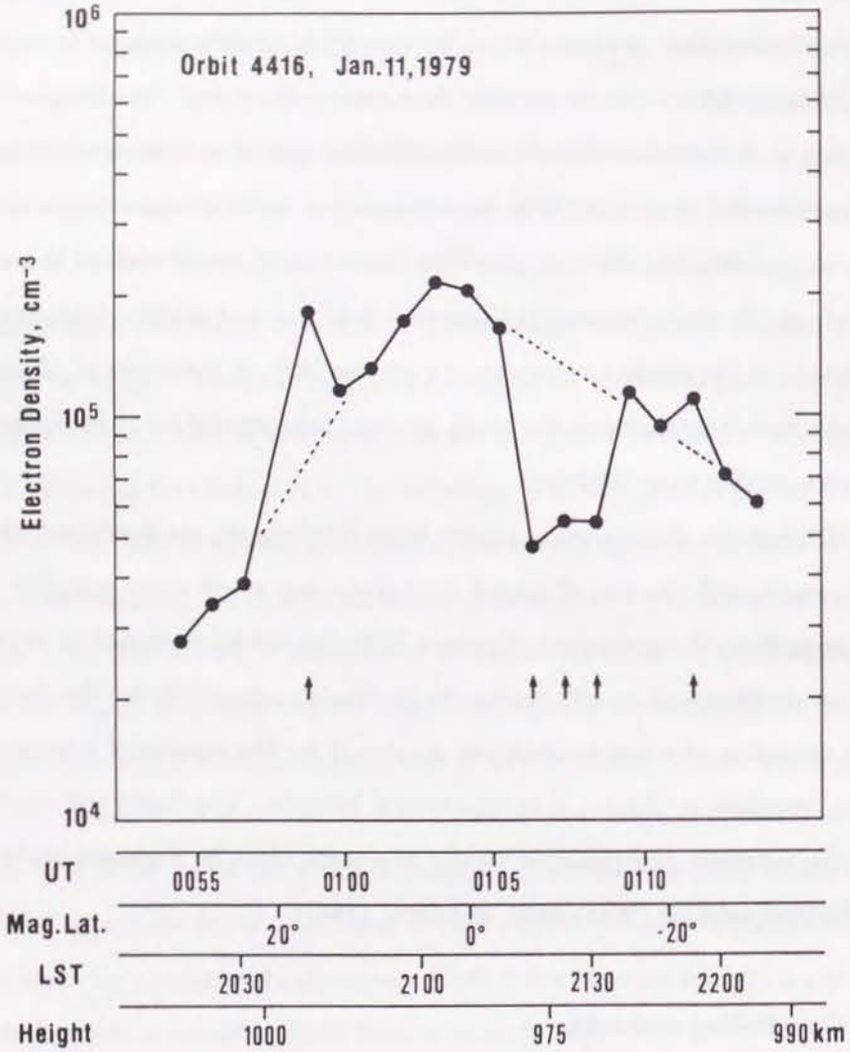

Fig. 2.19. Variation of electron density at the satellite heights showing abrupt density enhancement and depletion.

Pacific longitudes where the geomagnetic fields have large eastward declination; and during the equinoxes the ESF activity is high at the Indian longitudes where the magnetic declination angle is small.

Also revealed from the ionograms are the abrupt plasma depletions associated with severe backscatter echoes at the zero range, which are ascribed to the satellite encounter with a plasma bubble. The plasma bubbles are the results of nonlinear evolution of the Rayleigh-Taylor instability that is considered to be a primary mechanism to generate equatorial spread F. The positions of the detected plasma bubbles are within the area of high ESF activity. Another plasma irregularities at the satellite height are plasma enhancements or blobs. The number of example of the plasma blobs is very small, but we should not ignore this phenomenon because the generation of plasma blobs can not be explained by any existing theories; any theories would never complete without explaining this.

Chapter 3: Large-Scale Ionospheric Structure

3.1. Introduction

In the previous chapter we have found a combined seasonal-longitudinal effect of ESF. So far seasonal and/or longitudinal variations of ESF irregularities have been discussed to some extent. However, some of them are based on the observations in limited seasonal and longitudinal conditions. The global morphology of ESF presented in Chapter 2 is much more advanced observations such that global distribution maps of ESF activity are derived for various seasons, which allowed to separate the seasonal and longitudinal variations. It also rules out some mechanisms to explain longitudinal effect of ESF previously proposed, although those effects are not necessarily completely denied.

For example, BURKE *et al.* (1980) related the high occurrence probability of topside spread F irregularities in the American longitude sector to the weakest magnetic field at those longitudes of all others. Their discussion is based on the data obtained during September by the DMSP satellite and on other published results that are also obtained during northern winter season (BASU *et al.*, 1976; BURKE *et al.*, 1979). Apparently, any effect based on the magnetic field configuration alone cannot explain the annual migration of the longitude of high ESF activity as realized in Figure 2.14.

Another discussion of seasonal-longitudinal effect of plasma bubble is made by MULDREW (1980*a*, *b*). He used Alouette 2 topside ionograms recorded by the telemetry stations at Quito, Ecuador (78.6°W, 0.6°S) and Singapore (103.8°E, 1.4°N). These stations are in the meridian where the displacement of the magnetic equator is large. He suggests that the displacement of the magnetic and geographic equators plays an important role in the initiation of ESF and bubbles. Accordingly, the ESF activity is high in the December solstice at the American longitudes where the magnetic equator is largely displaced to the south while in the June solstice at the longitudes where the magnetic equator is largely displaced to the north. Unlike this, the observations

shown in Figures 2.14*e* and 2.14*k* demonstrate the highest ESF activity at around 30°W, where both equators coincide. Thus the displacement of the magnetic equator may not be a control factor.

To find mechanism(s) controlling the seasonal-longitudinal effect of ESF we investigate the background ionosphere; it is quite natural to suppose that there are changes in the large-scale ionospheric structure related to the stability of the ionosphere. In section 3.2 the ionospheric electron density at the satellite heights is examined. The results are interpreted in terms of transequatorial thermospheric winds in section 3.3. In section 3.4 a possible connection between the large-scale ionospheric structure, which is the manifestation of the thermospheric winds, and plasma instability is discussed.

3.2. Electron density at the satellite heights

3.2.1. North/south asymmetry There are two major factors affecting the large-scale ionospheric structure at low latitudes; zonal electric fields and thermospheric neutral winds. Zonal electric fields push up or down the ionosphere in the $\boldsymbol{E} \times \boldsymbol{B}$ direction depending on the field direction. Since the magnetic field lines are considered to be equipotentials at the F region heights, the electric field effect is symmetrical with respect to the magnetic equator in the magnetic meridional plane. Thermospheric winds cause the flow of plasma along the magnetic field line through the momentum transfer to the ions. Resultant redistribution of ionization appears in the magnetic meridional plane. Therefore, it is convenient to examine the large-scale ionospheric structure along the magnetic meridional plane to separate any possible local time and/or longitudinal dependence of the ionospheric properties.

As a preliminary examination, electron density along the satellite orbit was examined from the consecutive ionograms. The orbital inclination angle of ISS-b is about 70°. On the other hand, the declination angle of earth's magnetic fields is about 15-20°W at the Atlantic longitudes, and about 10 °E at the Pacific longitudes.

Therefore the orbital plane of the satellite is nearly parallel to the magnetic meridional plane at the Atlantic longitudes for the southbound passes and at the Pacific longitudes for the northbound passes. These longitude regions are characterized as two extremes of equatorial spread F activity during northern winter season as we have found in the previous chapter.

Shown in Figure 3.1 are the latitudinal variations of the electron density at the satellite heights determined from the ionograms by the method described in 2.6.1. The electron density distributions in Figure 3.1*a* are obtained from southbound passes crossing the magnetic equator in the direction almost parallel to the magnetic meridians at the Atlantic longitudes between 34°W and 57°W, where the extremely large ESF activity was seen in Figure 2.14*e*. In contrast to this, the electron density distributions shown in Figure 3.1*b* are obtained from northbound passes crossing the magnetic equator in the direction nearly parallel to the magnetic meridians at the Pacific longitudes between 162°E and 107°W, where the ESF activity was quite low as seen in Figure 2.14*d*.

When the ionogram exhibits severe spread F echoes at the zero range, the electron density is denoted by open circles and when the ionogram does not exhibit such zero range echoes it is denoted by dots in the figure. The latitude regions in which spread F was observed are indicated by shaded strips below each curve. It is noted that spread F is observed for most orbits in Figure 3.1*a*, but not observed for any orbits in Figure 3.1*b*.

A very significant difference is noticed between Figures 3.1*a* and 3.1*b*; when spread F appears (Figure 3.1*a*), latitudinal distribution of the background electron density is always symmetric with respect to the magnetic equator, while when spread F is not observed, the electron density distribution is strongly asymmetric with respect to the magnetic equator. In other words, there is a large latitudinal gradient in background electron density distribution when ESF is not observed.

The exception is observed in orbit 4376 in Figure 3.1*a*, where spread F is not

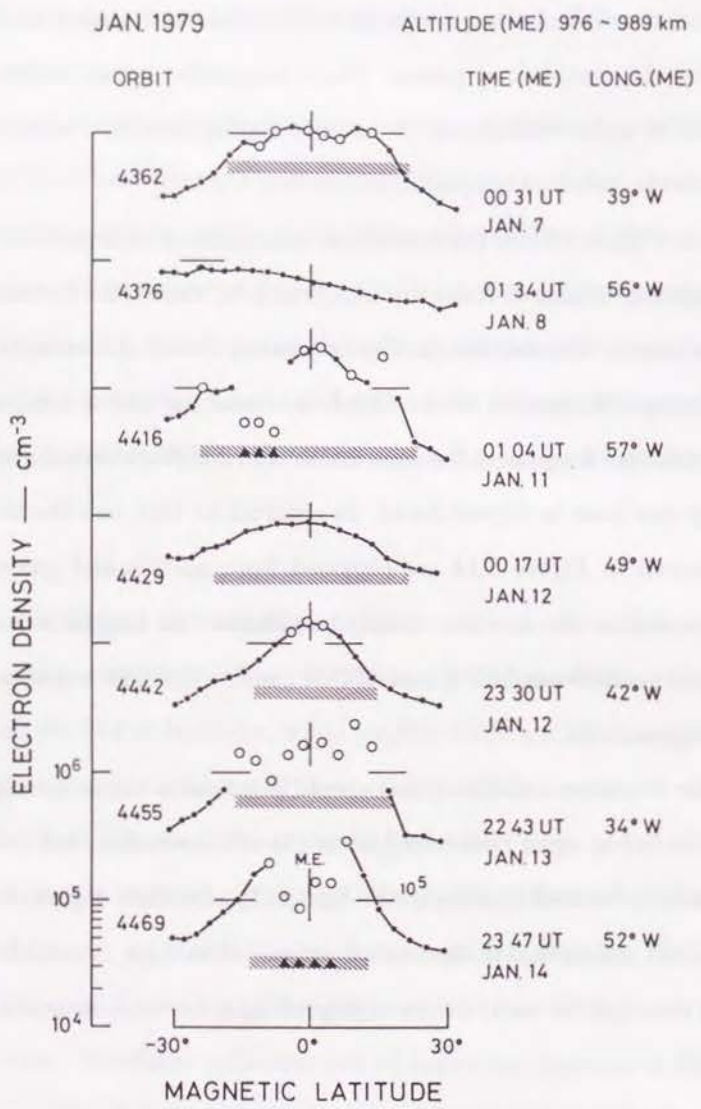

Fig. 3.1*a*. Electron density at the satellite heights determined from the ionograms obtained at the Atlantic longitudes. Open circles denote the existence of zero range spread echoes. Density scale of the successive curves should be displaced by one order as density of 10^5 cm^{-3} is denoted by the horizontal bar(s) on each curve. The vertical bars indicate the magnetic equator. Values on the right-hand side of each curve give universal time (UT) and geographic longitude at the magnetic equator (M.E.). The regions of spread F are indicated by shaded strips and abrupt density depletions by triangles in the strips.

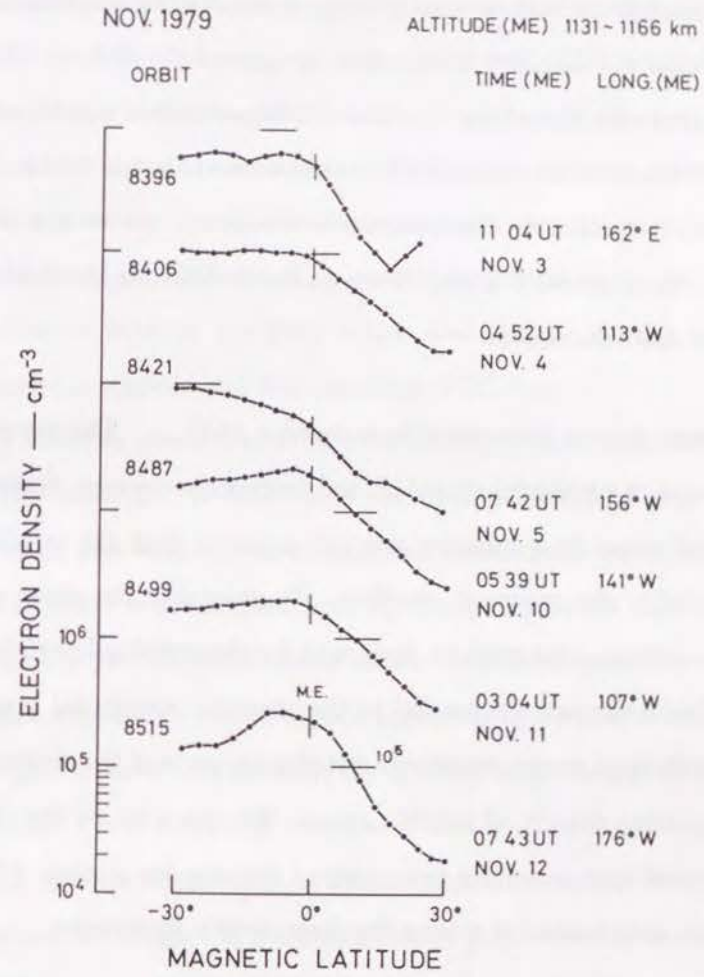

Fig. 3.1 *b*. Same as Figure 3.1*a* but for the Pacific longitudes. No spread F is observed.

observed but the electron density distribution is not very much asymmetric like the passes in Figure 3.1*b*. The difference of orbit 4376 from the other orbits in same longitude region is the lack of density bulge at around the magnetic equator, which may imply that the eastward electric field or upward $\boldsymbol{E} \times \boldsymbol{B}$ drift velocity was very small compared with the others. The lack of ESF and lack of equatorial density bulge in orbit 4376 invoke some contribution of the eastward electric field to the generation of the plasma irregularities. However, the reverse is not true as seen in orbit 8515 in Figure 3.1*b*, where spread F is not observed nevertheless an appreciable density bulge exists at the magnetic equator.

3.2.2. Electron density determined from sounder AGC The connection between the occurrence of equatorial spread F and large-scale electron density structure is demonstrated above by examining selected passes so that the satellite orbits were nearly parallel to the magnetic meridian. To generalize the above results a large number of ionogram data must be dealt with for the statistical confidence. However, most satellite orbits are not parallel to the magnetic meridional plane. Instead of analyzing individual passes, worldwide distribution maps of the electron density were obtained by using data in all satellite passes. For this purpose the electron density was determined by a computer processing of the sounder receiver AGC (automatic gain control) data instead of scaling the characteristic frequencies.

The AGC voltage data of the ISS-b sounder receiver are available at the time just before the pulse transmission. The interval between consecutive pulses is 0.111 sec (pulse repetition rate of 9 Hz), which is sufficiently long to decay the pulse-stimulated plasma waves (Benson, 1977, 1982). At frequencies between the plasma frequency at the satellite height and the ionospheric critical frequency (f_oF_2) below the satellite, the AGC voltage gives the intensity of cosmic radio noise (CRN) without any effects of the pulse transmission and interferences from the transmission on the ground (Hartz, 1969). Near the plasma frequency, however, the received intensity

of CRN gradually decreases with lowering the frequency by propagation effects in the topside ionosphere (Hartz and Roger, 1964). Thus the cutoff frequency of CRN determined from the AGC data provides a measure of electron density at the satellite height. In the actual receiving system, however, CRN cutoff is a function of the electron density, antenna gain and direction, ionospheric scale height, and CRN strength at the top of the ionosphere. While, there are large difficulties in the theoretical determination of the quantitative relation between the cutoff frequency and each factor that affects the CRN cutoff. Instead of theoretical model, we have derived an empirical relation between the AGC output and electron density by examining about 300 sampled ionograms and corresponding AGC data.

Figure 3.2 shows an example of AGC data and scaled plasma parameters for one revolution of the satellite. The AGC data are represented by the gray scale in the upper panel; white area corresponds to zero and darker areas correspond to higher AGC levels. The figure is constructed from 104 ionograms or 104 CRN spectra, and only lower frequency part (0.5-8.5 MHz) is shown. At frequencies of 3.8, 5.8, 5.9, 6.0, 7.6, and 7.8 MHz, continuous intense signals appearing as horizontal lines are due to instrumental spurious noise. Fortunately, the spurious noise disappears at frequency just below the CRN cutoff frequency; therefore it does not affect the determination of electron density. Intense interferences of ground transmissions are recognized at the upper right portion of the figure at frequencies above f_oF_2 shown by the solid line. At the lower frequency region centered 1.0 MHz, fairly intense AGC levels are recorded, which are presumably due to instrumental effects but details are unknown. In the lower panel, CRN cutoff (f_{CN0}), ordinary wave cutoff (f_N), and extraordinary wave cutoff (f_X) frequencies are shown by dots, solid line, and dashed line, respectively.

Scatter plots of AGC and plasma parameter are shown in Figures 3.3*a*-3.3*c*. The ordinates are AGC level of the raw 8-bit telemetry data format for all figures. The abscissas are ordinary wave cutoff (3.3*a*), extraordinary wave cutoff (3.3*b*), and upper hybrid resonance (3.3*c*) frequencies determined from the ionograms. Curve

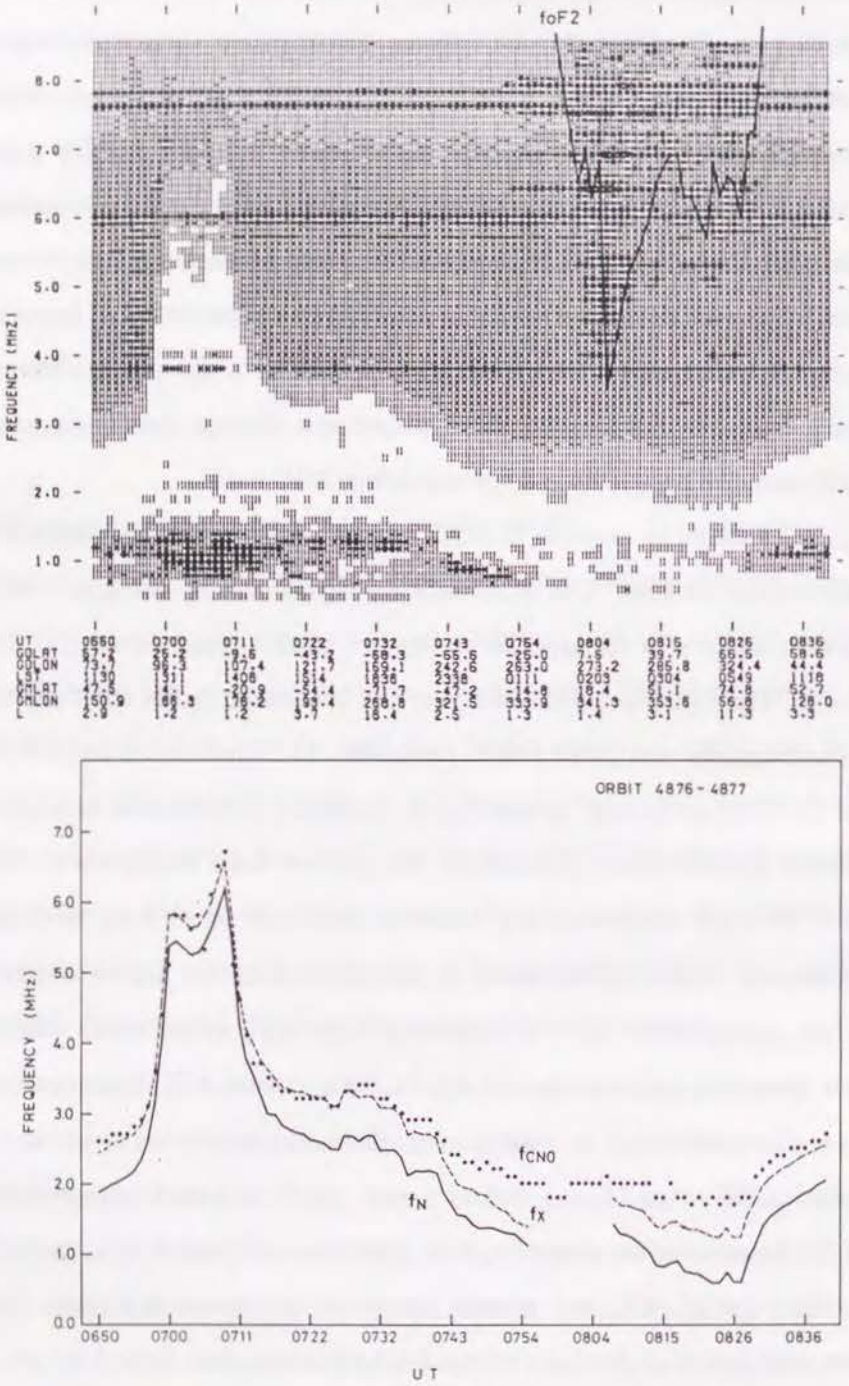

Fig. 3.2. AGC intensity map (top) and scaled plasma parameters (bottom).

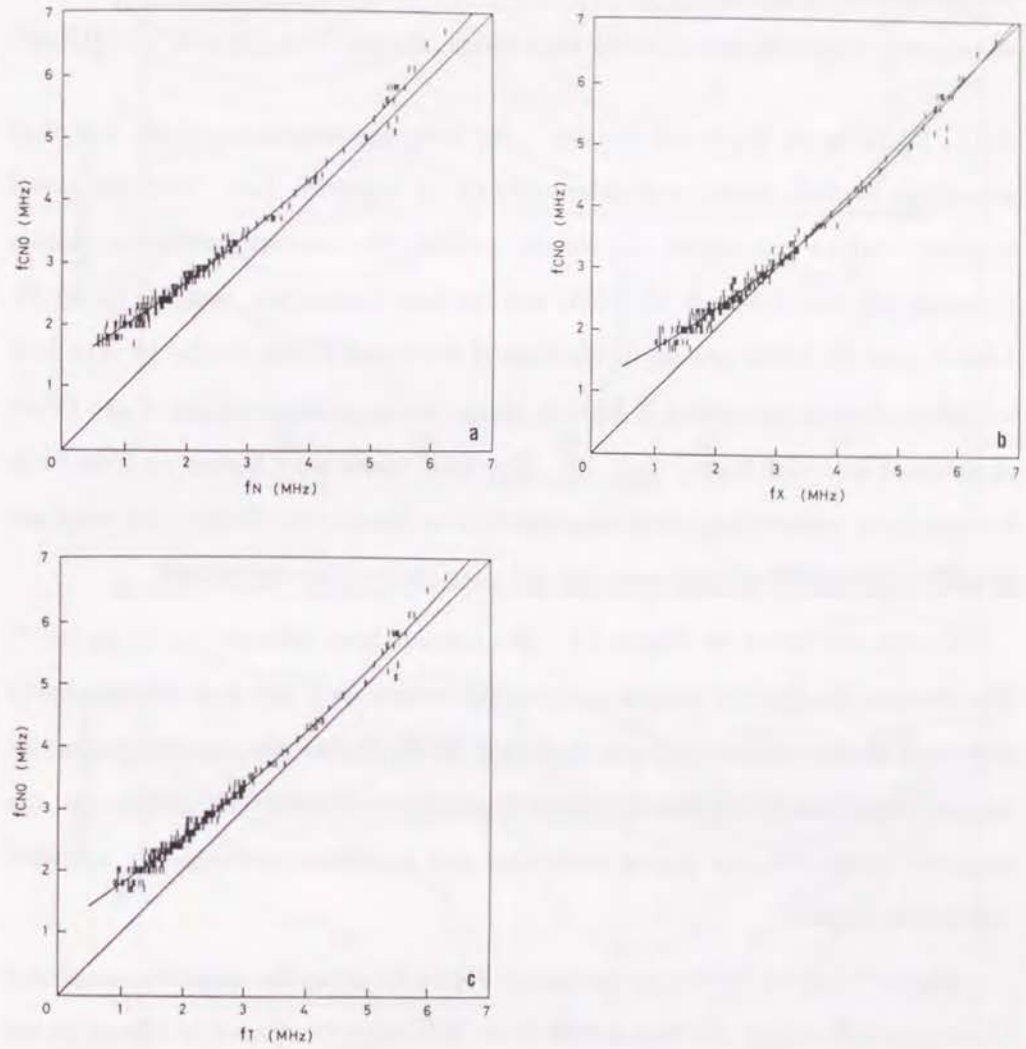

Fig. 3.3. Empirical relations between CRN cutoff and plasma parameters; ordinary wave cutoff (*a*), extraordinary wave cutoff (*b*), and upper hybrid resonance (*c*) frequencies.

fittings were made with parabola. The ordinary wave cutoff frequency exhibits best correlation with f_{CNO}, though other two also exhibit fairly good correlation. Electron density, N_e, is directly calculated by the relation, $N_e(\mathrm{cm}^{-3}) = 1.24 \times 10^4 [f_N(\mathrm{MHz})]^2$.

3.2.3. Global maps of electron density By using the empirical relation described above, the electron density was determined for all ionogram data. Then the global mapping analysis was carried out for two periods, the northern hemisphere winter (October 24, 1979-February 18, 1980) and northern hemisphere summer (April 21, 1980-August 22, 1980) seasons in the form of functional fitting similar to that used for the analysis of the spread F activity except for no artificial setting of the values at modified latitudes higher than 40°. The local times were limited to 2000-2400, because there exists a large local time variation in the electron density; the maps are so-called constant-local time maps but not snap shots of the ionosphere.

Results are shown in Figure 3.4. The contour lines indicate $\log N_e$ in cm^{-3}. The electron density distribution is somewhat complicated, and it is not necessarily maximum at the magnetic equator indicated by the dashed line nor the geographic equator. The dash-dotted lines are drawn in parallel to the magnetic meridians at the magnetic equator for two typical longitudes with maximum eastward and westward declination angles.

Figure 3.5 shows latitudinal sections of Figure 3.4 along the magnetic meridional plane approximated by the dash-dotted lines. The upper two panels in Figure 3.5 are for the northern winter period and lower two are for the northern summer period; and the left two panels are for 30°W longitude (Atlantic region) and the right two are for 150°W longitude (Pacific region). A systematic change in the shape of the magnetic meridional distributions of the electron density can be seen depending both upon the longitudes and seasons. The electron density distribution is symmetric with respect to the magnetic equator both at the Atlantic longitude in the northern winter period and at the Pacific longitude in the northern summer, where and when the ESF

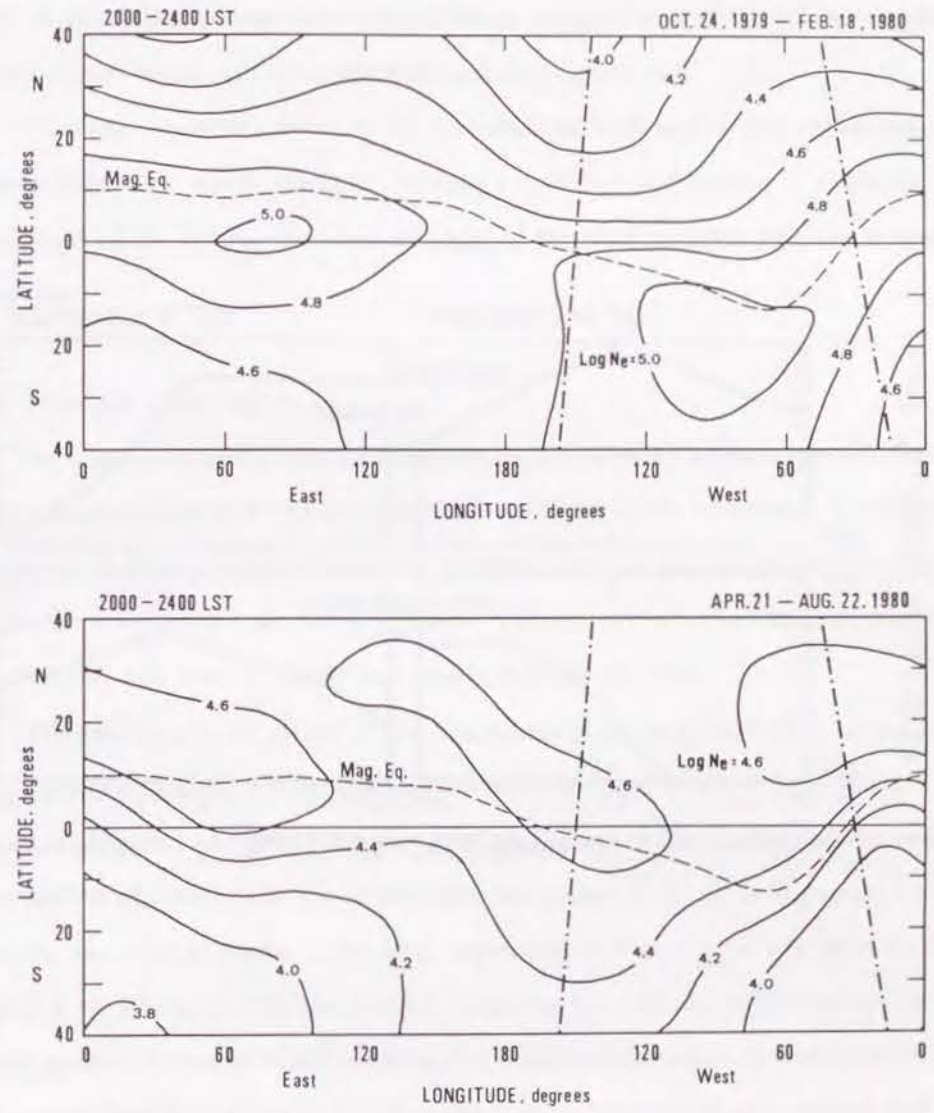

Fig. 3.4. Contour plots of logarithm of electron density at the satellite heights for northern winter (upper panel) and northern summer (lower panel) seasons. The dashed curve indicates the magnetic equator, and dash-dotted lines are the tangents to the magnetic meridional plane at the magnetic equator for two typical cases; longitudes of maximum eastward and westward declination angles.

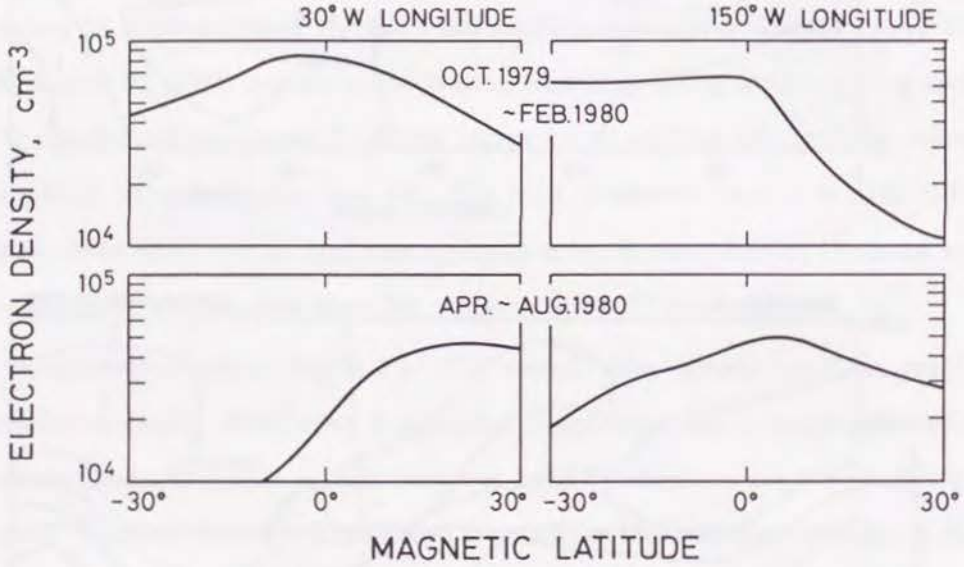

Fig. 3.5. Latitudinal distribution of electron density at the satellite heights along the dash-dotted lines in Figure 3.4. The upper two panels are for the northern winter season and the lower two are for the northern summer season. The left two panels are for the Atlantic region and the right two are for the Pacific region.

activity is high. In contrast to this, the electron density distribution is asymmetric both at the Atlantic longitude in the northern summer and at the Pacific longitude in the winter, where and when the ESF activity is quite low.

Thus the connection between the occurrence of ESF and large-scale ionospheric density structure, which was first obtained for the selected passes, is confirmed independent of the orbital condition or angle of the satellite orbit with the magnetic meridian.

3.3. Neutral wind effect

We have discussed in the previous section north/south asymmetric distribution of the electron density at the satellite heights relating to the occurrence of equatorial spread F. It is essential to investigate, however, the distribution of electron density below the satellite altitude, because plasma bubbles are formed on the bottomside of the F layer, and then rise up to the topside (Ossakow, 1981).

The real height reduction of the ionograms gives us information on the electron density distribution from the satellite altitude down to the F layer peak. Two-dimensional structure in the magnetic meridional plane of the topside electron density distribution obtained from the consecutive ionograms is shown in Figures 3.6*a* and 3.6*b* for two typical passes, orbit 4442 appearing in Figure 3.1*a* and orbit 8421 in Figure 3.1*b*. In Figure 3.6*a* the electron density at the altitudes below the letters "**F**" could not be determined from the ionograms because of the severe spread F condition. The upper boundary of the region of spread F irregularities is closely aligned with the magnetic field line denoted by the broken curve crossing the equator at 1000 km, being symmetric with respect to the magnetic equator. In the region outside the spread F irregularity zone evidently the contours of electron density up to the satellite altitude from the F layer peak show striking similarity in pattern between both hemispheres notwithstanding nearly solstitial conditions. Another important point to be noted here is a symmetric pattern of the F layer peak altitudes in both hemispheres de-

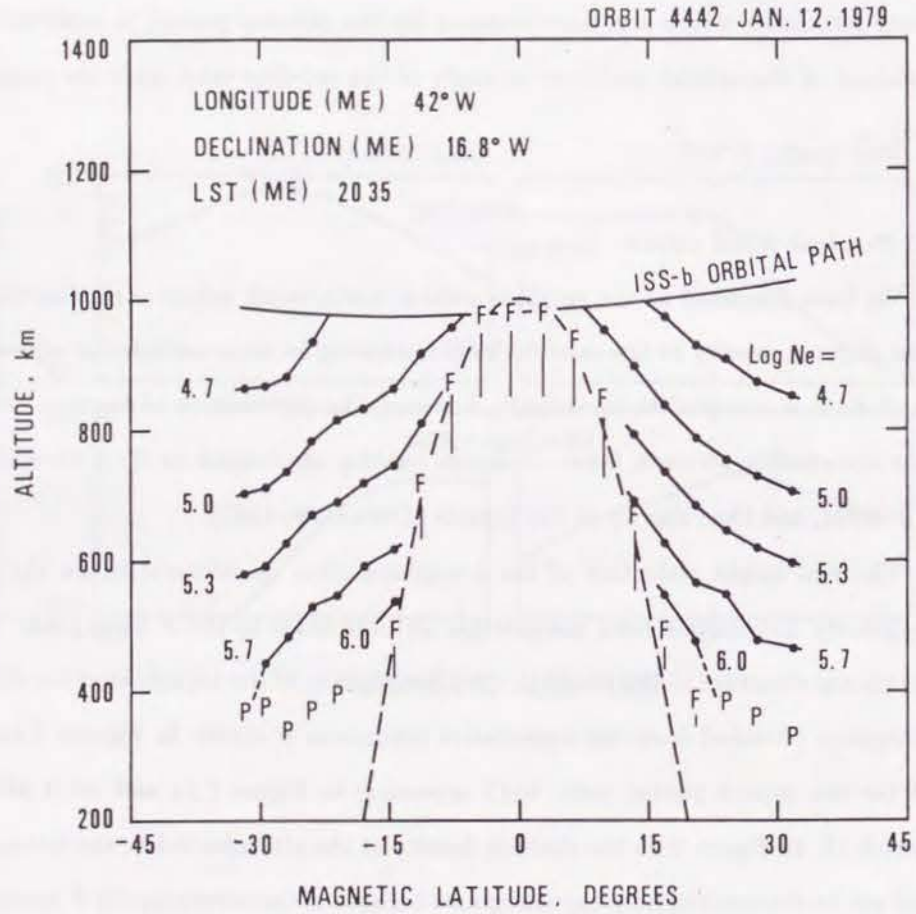

Fig. 3.6*a*. Contour plots of logarithm of electron density in the plane parallel to the satellite trajectory. The orbit crosses the magnetic equator at 42° W longitude (over the Atlantic Ocean). The vertical electron density profiles are derived by the real height analysis of the consecutive ionograms along the orbital path. The letter "**P**" denotes the *F* layer peak. Spread *F* traces appear in the region below the letters "**F**". The magnetic field line crossing the magnetic equator at 1000 km is shown by the broken curve.

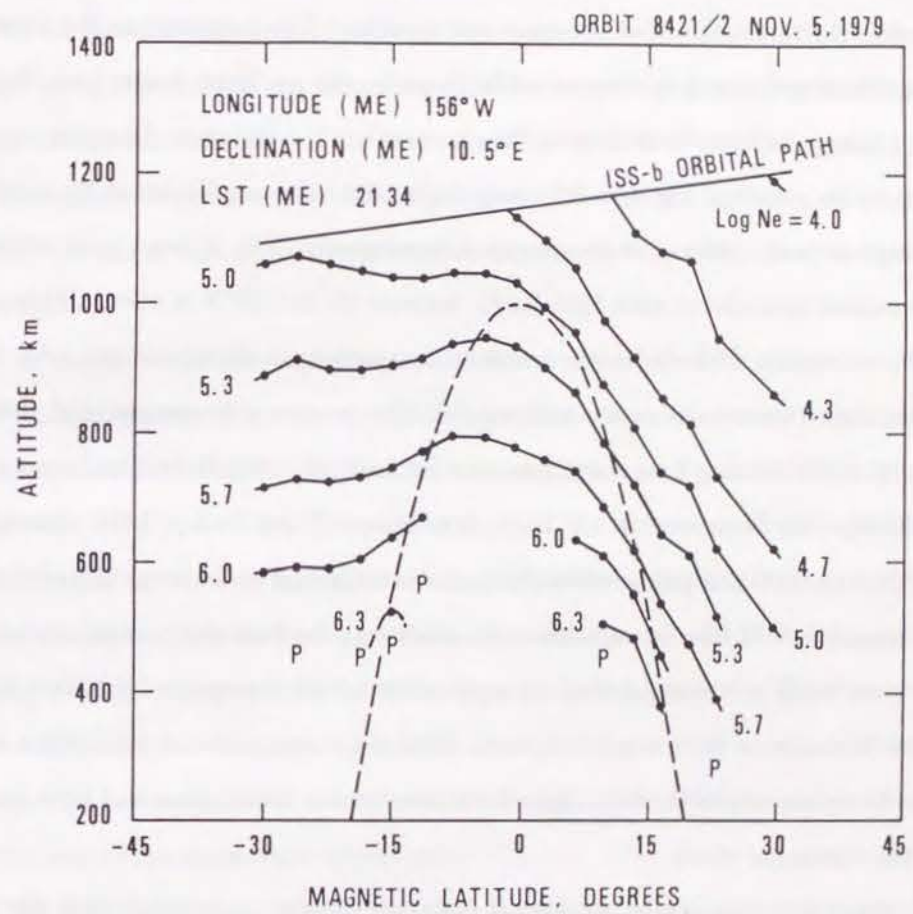

Fig. 3.6*b*. Same as Figure 3.6*a* but at the longitude of 156° W (over the Pacific Ocean). No spread *F* is observed.

noted by the letters "**P**" in the figure, which may imply that the thermospheric wind component in the magnetic meridional plane is divergence/convergence wind with respect to the magnetic equator and transequatorial wind is weak.

In contrast to above, in Figure 3.6*b*, the electron density distribution is quite asymmetric with respect to the magnetic equator. The contours in the southern hemisphere are nearly horizontal while those in the northern hemisphere decline. Considering magnetic field aligned density profiles, the distances from the equator down to the points of $\log N_e = 5.3$ along the broken curve are 630 km in the southern hemisphere and 1300 km in the northern hemisphere. The F layer peak altitudes also exhibit asymmetry such that $h_m F_2$ between 20 and 25°N is about 280 km and $h_m F_2$ at similar latitude in the southern hemisphere is about 450 km. All these asymmetric characteristics are well attributable to strong transequatorial thermospheric winds blowing from south (summer hemisphere) to north (winter hemisphere) as follows (BITTENCOURT *et al.*, 1976; BITTENCOURT and SAHAI, 1978; ANDERSON and ROBLE, 1981): A poleward wind transports ionization to the lower altitudes along the magnetic field line through the momentum transfer from the neutral particles to the ions, while at the same time an equatorward wind transports ionization to the higher altitudes in the other hemisphere. Thus the transequatorial wind yields hemispheric asymmetry in the field aligned electron density distribution and layer heights off the equatorial plane.

These two examples of meridional structure allow us to conclude that the symmetry/asymmetry in the distributions shown in Figures 3.1 and 3.5, which are statistically reliable results, may extend down to the whole F region and may reflect the effects of the transequatorial winds.

The horizontal component of the thermospheric pressure gradient is the major driving force for the winds in the ionospheric F region (RISHBETH, 1972), and Coriolis force vanishes at the geographic equator. The driving force at the geographic equator and at altitude of 300km is computed from the neutral air density and neutral

temperature based on the MSIS (mass spectrometer and incoherent scatter) empirical thermospheric model (HEDIN *et al.*, 1977a, b) by using a value of $F_{10.7}$ flux at 170 to be adequate to the period of the ISS-b observation, and a value of A_p index at 4. Figure 3.7 shows annual variations of two components of the driving force per unit mass of the air parallel and perpendicular to the magnetic field computed for 1900 LST which is slightly early to the time when ESF is first observed, and for three cases in which the declination angles of the magnetic field are -20°, -2°, and 10°corresponding to the equatorial points at the Atlantic, Indian, and Pacific longitudes, respectively. Where the minus sign denotes westward declination and the plus sign does eastward declination.

In the figure the plus sign means eastward and northward for the perpendicular and parallel components, respectively. The perpendicular components do not change very much with seasons, but the parallel components are very variable not only in the amplitude but also the sign. The parallel components become small during northern winter period for the field line of -20°declination, which represents the Atlantic longitudes, during northern summer period for 10°declination, the Pacific longitudes, and during two equinoctial periods for -2°declination, Indian longitudes. In other words, thermospheric winds are expected to blow in perpendicular to the magnetic field line in the three cases described above, and the strong transequatorial wind is expected for the rest of the above three conditions.

By these calculations, we conclude that the symmetric and asymmetric structure of the electron density distribution in the magnetic meridians, which we have seen in Figures 3.4 and 3.5, is due to the transequatorial component of thermospheric winds.

3.4. A possible connection between ESF and the large-scale structure

As we have briefly mentioned in 2.6.1, equatorial spread F is due to small-scale density irregularities which are generated in association with the nonlinear evolution of the gravitational Rayleigh-Taylor instability. An electron density depletion or a

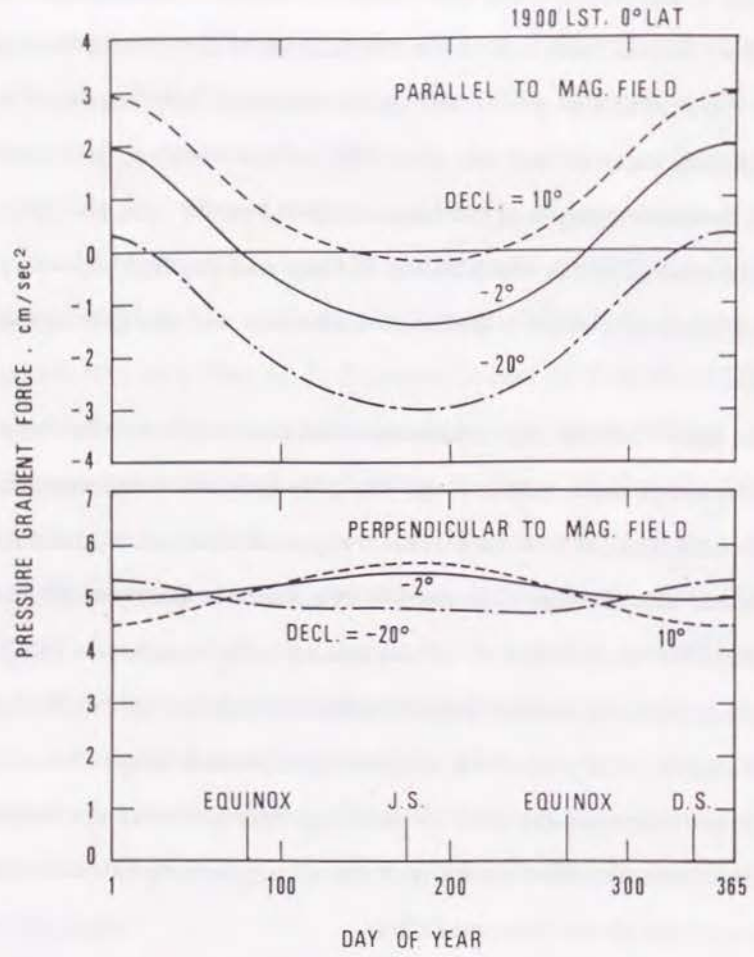

Fig. 3.7. Driving forces based on the MSIS empirical thermospheric model: components parallel to the magnetic field (upper panel) and perpendicular to it (lower panel) for a variety of magnetic declination angles; 10°, -2°, and -20°, which represent the Pacific, Indian, and Atlantic longitudes at the magnetic equator, respectively. Positive forces denote eastward for the perpendicular component and northward for the parallel component.

plasma bubble arising from the Rayleigh-Taylor instability grows initially on the bottomside of the F layer, and rises up to the topside, producing small scale density irregularities as the source of spread F. Although a numerous number of observations, theories, and numerical calculations support the above fundamental process as a cause of equatorial spread F, none of the existing theory may explain the seasonal-longitudinal effect found in Chapter 2. In this section we attempt to connect the large-scale ionospheric structure and the plasma instability.

Recently, many researchers discussed thermospheric wind effects on the generation of Rayleigh-Taylor bubbles (Chiu and Straus, 1979; Kelley *et al.*, 1981; Guzdar *et al.*, 1982; Anderson *et al.*, 1982; and Tsunoda, 1983) and on the evolution of the bubble (Zalesak *et al.*, 1982; and Anderson and Mendillo, 1983). The above authors discussed a zonal component of the winds which takes part in the generation of bubbles through additional destabilization or seeding of the gravity driven Rayleigh-Taylor instability. What we suggest here on the basis of the ISS-b observations is another possible effect of the neutral wind such as stabilization of the instability by the transequatorial thermospheric wind.

As mentioned already, effects of the transequatorial thermospheric wind on the ionospheric plasma distribution at low latitudes are as follows: A poleward wind lowers ionization along the magnetic field line and, in the other hemisphere, an equatorward wind raises ionization to the higher altitudes. Thus the transequatorial wind yields hemispheric asymmetry in the layer heights off the equatorial plane.

Turning to the instability problem, before discussing the transequatorial wind effects, most theoretical and numerical studies are made with two-dimensional approximation concerning the ionospheric parameters in the equatorial plane. There also have been some efforts to investigate the ionospheric instability taking the contribution of plasma away from the equator into consideration. Haerendel (1973) pointed out that the growth of the Rayleigh-Taylor instability at the equatorial latitudes should be discussed as an instability problem for the magnetic line of tube

through the whole F region. In this case the important quantities are the electron contents integrated in the magnetic flux tube and the field line-integrated Pedersen conductivity (see also ANDERSON and HAERENDEL, 1979), instead of local quantities at the magnetic equator. At any rate, irrespective of the approximation, the large Pedersen conductivity causes shortcircuiting of the polarization electric fields arising from the instability process. Therefore the Rayleigh-Taylor instability is suppressed by the increase of Pedersen conductivity.

HAERENDEL considered only electron density distribution that is symmetric with respect to the magnetic equator. The redistribution of the ionospheric plasma owing to the transequatorial wind, however, makes a finite contribution to the changes of the field line-integrated Pedersen conductivity since the collision frequency varies in an exponential way in altitude as schematically shown in Figure 3.8. We consider a case in which the magnitudes of the rise and fall of the F layer at the conjugate points are equal and greater than the scale height of the collision frequency ($\sim$50 km) (OSSAKOW *et al.*, 1979). The net increase of the line-integrated Pedersen conductivity may be appreciable because of the larger contribution from the plasma on the lee side than the opposite contribution from the plasma on the windward side.

BITTENCOURT and SAHAI (1978) calculated that the transequatorial wind with velocity of 200 m/sec produces a difference of 120 km in the F peak heights between the conjugate points at 15° in magnetic latitude. Thus it is reasonable to postulate that an intense transequatorial wind changes the integrated Pedersen conductivity, which results in the suppression of the growth of plasma instability. Many observed aspects of the seasonal-longitudinal effect of ESF and electron density distribution are well accounted for by this mechanism. The discussion so far, however, is quite speculative, so we need more theoretical and numerical elaboration of this idea, which will be described in the next chapter.

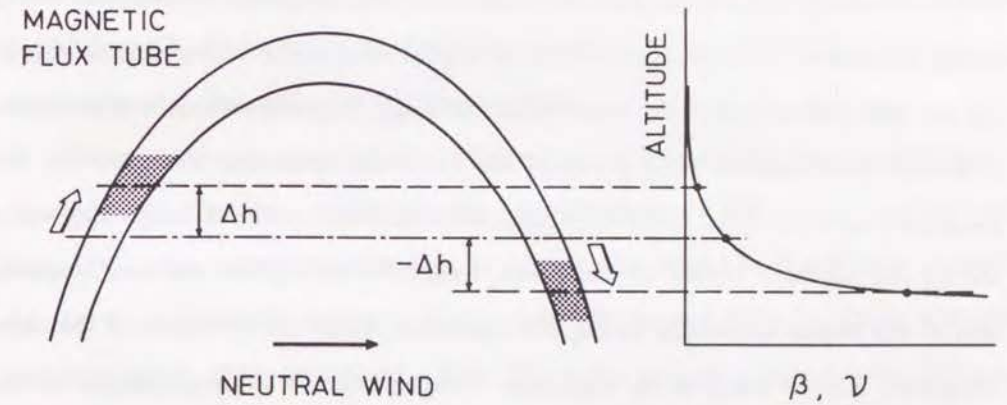

Fig. 3.8. Schematic illustration showing the effect of a transequatorial component of thermospheric winds on the redistribution of the ionosphere and the stability.

3.5. Concluding remarks

It was found that the electron density distribution in the magnetic meridional plane is symmetric with respect to the magnetic equator when and where the ESF activity enhancement is seen, while it is asymmetric when and where the ESF activity is low. This morphological connection between the large-scale structure and ESF suggests that a transequatorial component of the thermospheric winds in the magnetic meridional plane plays a role in suppression of the growth of the gravitational Rayleigh-Taylor instability and therefore the ESF activity. A plausible mechanism of the instability suppression is the shortcircuiting of polarization electric field owing to the increase of Pedersen conductivity by the lowering of the ionospheric heights in the lee side hemisphere of the transequatorial wind. Therefore absence of a transequatorial thermospheric wind is one of the important necessary conditions for the generation of ESF. Such condition tends to be satisfied at the Atlantic longitudes during the northern winter, at the Pacific longitudes during the northern summer, and at the Indian longitudes during the equinoxes, where the directions of the thermospheric diurnal winds in the nighttime F region tend to be perpendicular to the magnetic meridians following the seasonal migration of the thermospheric pressure bulge.

Chapter 4: Theoretical Calculation of ESF

4.1. Introduction

We have found a significant longitudinal-seasonal effect of equatorial spread F (ESF) in Chapter 2. This effect is shown to be connected with the change in large-scale ionospheric structure due to the transequatorial thermospheric wind in Chapter 3. Furthermore it is proposed that the redistribution of plasma along the magnetic field line due to the transequatorial wind, which is the cause of the change in large-scale ionospheric structure, plays an important role in the growth of the plasma instability. The discussion presented there, however, is very speculative; therefore we need numerical elaboration of this mechanism.

Recent extensive experimental, theoretical, and numerical studies allow us to conclude that the basic mechanism for the generation of ESF is the gravitational Rayleigh-Taylor instability operating in combination with the $\boldsymbol{E}\times\boldsymbol{B}$ drift instability due to an ambient eastward electric field (Basu and Kelley, 1979; Kelley and McClure, 1981; Ossakow, 1981). Up to the present a large number of theoretical and numerical studies of the Rayleigh-Taylor instability have been made, but most of them are based on the two-dimensional approximation that considers only plasma in the magnetic equatorial plane. However, in the mechanism proposed in Chapter 3 to suppress the plasma instability, plasma away from the magnetic equator is important. Thus the existing two-dimensional theory cannot be applied to the current problem or transequatorial wind effect on the plasma instability and the seasonal-longitudinal effect of ESF.

In this chapter a non-local theory of instability model for the gravitational Rayleigh-Taylor and $\boldsymbol{E}\times\boldsymbol{B}$ drift modes is developed. The instability model includes the contributions from plasma away from the magnetic equatorial plane. In section 4.2 theoretical expression of the linear growth rate of the instability is derived. The growth rate of the instability is evaluated using the ion density distribution obtained

by solving the ion continuity equations including dynamics for O^+, NO^+, O_2^+, and N_2^+ ions under the influence of electric fields and neutral winds. In section 4.3 the mathematical formulation for the ionospheric modeling, electric field model, and neutral wind model are described. In section 4.4 the results are shown, and the effects of the transequatorial component of the thermospheric wind and the $\boldsymbol{E} \times \boldsymbol{B}$ drift are discussed.

4.2. Non-local theory of plasma instability

4.2.1. Preliminary discussion There has been a great advance in the theoretical and numerical studies on the instability relating with ESF, and we have a fairly clear picture of the problem (OSSAKOW, 1981). Most theories and numerical simulations have been developed on the basis of two-dimensional approximation, in which only characteristic values in the magnetic equatorial plane are considered. In the ionospheric F region the diffusion is allowed only along the magnetic field line because the ion-neutral collision frequency is very low in comparison with the ion gyrofrequency. On the other hand, the magnetic field lines are assumed to be horizontal in a wide latitudinal extent around the magnetic equator. Thus the ionospheric parameters relevant to the instability do not change very much in the direction of the magnetic field line (HANSON *et al.*, 1986), and the two-dimensional approximation may be pertinent to the problems in many cases.

Figure 4.1 schematically illustrates bottomside of the equatorial ionospheric F region. In the figure $\boldsymbol{B}$, $\boldsymbol{E}$, and g represent earth's magnetic field, ambient eastward electric field, and gravitational force, respectively. In the ionospheric F region gravitational ($en(g \times \hat{z})/\Omega_i$) and Pedersen ($\sigma_p \boldsymbol{E}$) currents flow (cgs system is used throughout the paper). Where e is the charge of the ion, n is the ion density, $\hat{z}$ is the unit vector parallel to $\boldsymbol{B}$, Ω_i is the ion gyrofrequency, and σ_p is the Pedersen conductivity as defined later. These currents are carried by the ions. When there exists unduration, the currents cause charge accumulation. The resultant polarization

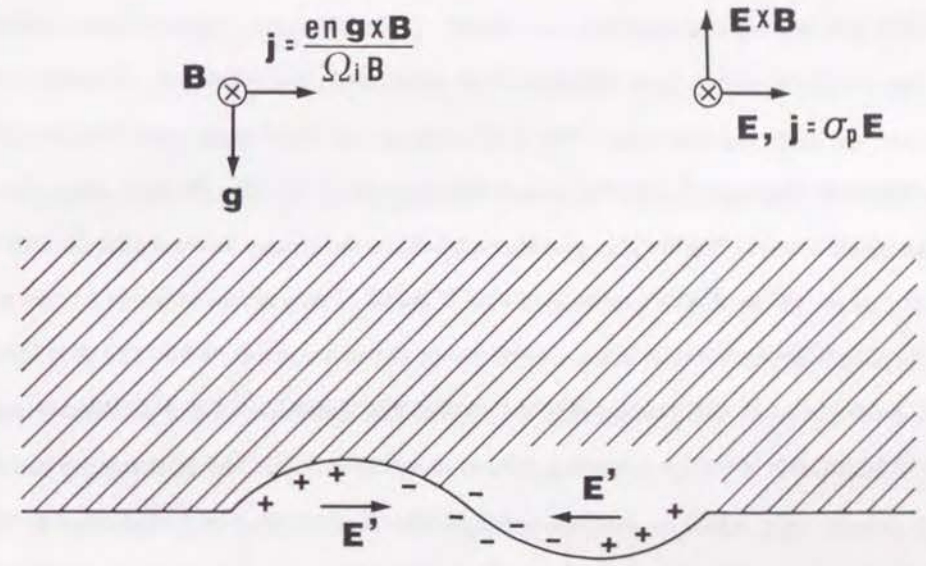

Fig. 4.1. Schematic illustration showing linear instability at the bottomside of the equatorial ionospheric F region for two-dimensional approximation. Shown is the zonal plane: the earth's magnetic field ($\boldsymbol{B}$) is perpendicular to the plane, and the ambient zonal electric field ($\boldsymbol{E}$) and the gravitational force (g) are parallel to it. The polarization electric fields ($\boldsymbol{E}'$)due to the small density perturbation cause the perturbation to grow.

electric fields, $\boldsymbol{E}'$, operate in such a way that the perturbation drifts, $\boldsymbol{E}' \times \boldsymbol{B}$, cause the undulation to grow.

The linear growth rate of the instability for the above system is well examined and given by (e.g., SCANNAPIECO and OSSAKOW, 1976; OTT, 1978)

$$\gamma = \frac{\nabla n}{n}\left(\frac{g}{\nu_{in}} + c\frac{E}{B}\right) \tag{4.1}$$

where ∇n is the upward-directed ion density gradient, ν_{in} is the ion-nutral collision frequency, and c is the light velocity. The ambient electric field, E, is taken to be positive for eastward direction. The first term in the right-hand side of (4.1) is the gravitational Rayleigh-Taylor term and the second is the $\boldsymbol{E}\times\boldsymbol{B}$ drift term due to an ambient electric field. The gravitational force is always antiparallel to the ion density gradient on the bottomside of the F layer. Thus, in equation (4.1), we note the Rayleigh-Taylor term is always unstable at the bottomside; while the $\boldsymbol{E}\times\boldsymbol{B}$ drift term is unstable at the bottomside only when the direction of the ambient electric field is eastward. A steep upward gradient in ion density at the bottomside yields a large growth rate, which is attained at night due to the rapid recombination process and the lack of photoionization in consistent with the fact that ESF is intrinsically a nighttime phenomenon as shown in Chapter 2. For the Rayleigh-Taylor term, the collision frequency, ν_{in}, in (4.1) is related with the Pedersen conductivity as

$$\sigma_p = \frac{cen}{B}\frac{\nu_{in}}{\Omega_i} \tag{4.2}$$

When the layer is high, or ν_{in} is small, the Pedersen conductivity is small and the shortcircuiting of the polarization field due to the gravitational force is not very efficient. KELLEY and MARUYAMA (1991) calculate instability growth rate using the vertical drift velocity (equivalent to the zonal electric field) observed at Jicamarca, Peru, and compared with the occurrence of severe spread F. They show that the eastward electric field is by itself not sufficient for severe spread F, and layer must be transported to a high enough altitude that the gravitational term becomes strong. Thus the Pedersen conductivity seems to be the crucial parameter for the instability.

Although a consensus has been reached that the basic Rayleigh-Taylor instability process in conjunction with the $\boldsymbol{E}\times\boldsymbol{B}$ drift instability accounts for ESF generation based on the two-dimensional approximation, there remain some observational aspects of ESF and bubbles not clearly explained with the two-dimensional model. For example, in Chapter 3, we have argued a role of the plasma away from the magnetic equator in the suppression of instability to explain the seasonal-longitudinal effect of ESF, where the change in the integrated Pedersen conductivity is important.

ZALESAK *et al.* (1982) developed a three-layer model for numerical simulations of the effects of zonal neutral winds and background Pedersen conductivity on the nonlinear evolution of plasma bubbles. This model considers the effect of the plasma away from the equator. Their layer 2 represents an equatorial plane and layers 1 and 3 simulate the E layer with large Pedersen conductivity away from the equatorial plane. Three layers are electrically connected with each other via a conducting magnetic field line, but particle flows between the layers are inhibited.

There is another effort to investigate the ionospheric instability taking the contribution of plasma away from the equatorial plane into consideration. BALSLEY *et al.* (1972) pointed out that the quantities in (4.1) have to be replaced by those averaged along the magnetic field line. They demonstrate that the plasma is unstable just above the F layer peak at the equator where the integrated electron content has upward gradient. HAERENDEL (1973) derived a growth rate of the Rayleigh-Taylor instability in terms of the above mentioned field-line averaged parameters.

The present work differs from that of HAERENDEL (1973) in the following way: (1) In the present instability model we consider the electron density gradient which changes as a function of position on the magnetic field line, while HAERENDEL considers the gradient of the integrated electron content; and (2) the ambient electric fields

are included in the present model, but not in the model of HAERENDEL, which is important for the application of the theory to the actual problem because the $\boldsymbol{E}\times\boldsymbol{B}$ drift term is equally important to the gravitational Rayleigh-Taylor term in the instability as we will see later. The linear instability model we are developing here may be considered as an extension of the three-layer model described by ZALESAK *et al.* (1982) to a multilayer model.

The numerical calculations with non-local instability model include not only O^+ ions but also molecular ions by two reasons. First, the ion-neutral collision frequency is extremely high at the lower altitudes where the molecular ions might be the dominant ion species. Therefore the Pedersen conductivity in the molecular ion-dominated region away from the magnetic equator, but electrically connected with the equatorial ionosphere, may have an appreciable contribution to the instability even if the O^+ is major ion species in the magnetic flux tube. Second, preliminary model calculations showed that the O^+ density after the sunset rapidly dropped to zero with decreasing altitude on the bottomside of the F layer by the recombination process. The vertical electron density gradient became extremely large near the altitude of zero density. Thus the growth rate of the instability reaches the maximum value there. On the other hand, rocket experiments (MORSE *et al.*, 1977) show relatively constant valley electron density of $10^3 \sim 10^4\,\mathrm{cm}^{-3}$ in the bottomside, in which molecular ions are considered to be dominant ion species. Therefore the above maximum growth rate at the altitude of $n(O^+) \sim 0$ is unrealistic and including the molecular ions is indispensable for the quantitative analysis of the instability.

4.2.2. Coordinate system In the computation of the parameters pertinent to the instability growth rate the magnetic field line is supposed to be in a dipole geometry and to be an equipotential. We use the orthogonal coordinate system (p, q, ψ) which is often used in a problem that includes a dipole magnetic field (see MURPHY *et al.*, 1983), where ψ is longitude, and p and q are defined as follows from the polar

coordinate r (geocentric distance) and θ (colatitude), and earth's radius r_0

$$p = \frac{r}{r_0 \sin^2\theta} \tag{4.3a}$$

$$q = \frac{r_0^2 \cos\theta}{r^2} \tag{4.3b}$$

Magnetic field lines are provided as p =constant. Considering a plane that is perpendicular to the magnetic field line, we determine unit vectors $\hat{x}$, $\hat{y}$, and $\hat{s}$ as $\hat{x}$ directs east and $\hat{y}$ directs up, both in this plane, and as $\hat{s}$ directs south along the magnetic field line. Scale factors are

$$h_1 = \frac{\partial \hat{x}}{\partial \psi} = p r_0 \sin^3\theta \tag{4.4a}$$

$$h_2 = \frac{\partial \hat{y}}{\partial p} = \frac{r_0 \sin^3\theta}{\Delta} \tag{4.4b}$$

$$h_3 = \frac{\partial \hat{s}}{\partial q} = -\frac{p^3 r_0 \sin^6\theta}{\Delta} \tag{4.4c}$$

where $\Delta \equiv (1+3\cos^2\theta)^{1/2}$. The magnetic field lines are assumed to be equipotentials ($= \phi$), and the eastward electric field component at a given point on the field line, E_x, is connected with that at the equator on the same field line, E_x^{eq}, as follows:

$$E_x = -\frac{1}{h_1}\frac{\partial \phi}{\partial \psi} = \frac{1}{\sin^3\theta} E_x^{eq} \tag{4.5}$$

The strength of magnetic induction, B, of dipole field is represented as

$$B = \frac{\Delta}{p^3 \sin^6\theta} B_0 \tag{4.6}$$

where B_0 is the strength of magnetic induction on the earth's surface at the equator. Thus the $\boldsymbol{E}\times\boldsymbol{B}$ drift velocity due to an eastward electric field, $v_\perp$, is connected with the equatorial values on the same field line, v_p,

$$v_\perp = \frac{cE_x}{B} = \frac{\sin^3\theta}{\Delta} v_p \tag{4.7}$$

4.2.3. Linear growth rate of non-local theory The instability model includes not only O^+ ions but also molecular ions by the reasons described in 4.2.1. The continuity equation for the i-th ion species (i=1, 2, 3, and 4 for O^+, NO^+, O_2^+, and N_2^+) is given by

$$\frac{\partial n_i}{\partial t} + \nabla\cdot(n_i v_i) = P_i - L_i \tag{4.8}$$

where n_i is the ion density, v_i is the ion velocity, P_i and L_i are the rates of ion production and loss, and the subscript i denotes the i-th ion species. The second term on the left-hand side of the equation is rewritten as follows:

$$\nabla\cdot(n_i v_i) = \nabla_\perp\cdot(n_i v_{\perp i}) + \frac{1}{A}\frac{\partial(A n_i v_{\parallel i})}{\partial s}$$

where $A = \sin^6\theta/\Delta$ is the ratio of a cross sectional area of the magnetic flux tube at a given point to that at the equator, and $v_{\parallel i}$ is a field aligned velocity of the i-th ion species. Equation (4.8) is rewritten

$$\frac{\partial n_i}{\partial t} + \nabla_\perp\cdot(n_i v_{\perp i}) = P_i - L_i - \frac{1}{A}\frac{\partial(A n_i v_{\parallel i})}{\partial s} \tag{4.9}$$

In the nighttime equatorial F region the background ionosphere is assumed to be in a quasi-equilibrium, and the right-hand side of the above is neglected;

$$\frac{\partial n_i}{\partial t} + \nabla_\perp\cdot(n_i v_{\perp i}) = 0 \tag{4.10}$$

Perpendicular components of the ion and electron velocities under the influence of an electric field $\boldsymbol{E}$ and the gravity g are given as

$$v_{\perp i} = \frac{\nu_{in}^2}{\nu_{in}^2+\Omega_i^2}\left(\frac{e\boldsymbol{E}}{m_i\nu_{in}} - \frac{g\cos I}{\nu_{in}}\hat{y}\right) + \frac{\nu_{in}\Omega_i}{\nu_{in}^2+\Omega_i^2}\left(\frac{-e\boldsymbol{E}\times\hat{s}}{m_i\nu_{in}} + \frac{g\cos I}{\nu_{in}}\hat{x}\right) \tag{4.11}$$

$$v_{\perp e} = \frac{\nu_{en}^2}{\nu_{en}^2+\Omega_e^2}\left(\frac{-e\boldsymbol{E}}{m_e\nu_{en}} - \frac{g\cos I}{\nu_{en}}\hat{y}\right) - \frac{\nu_{en}\Omega_e}{\nu_{en}^2+\Omega_e^2}\left(\frac{e\boldsymbol{E}\times\hat{s}}{m_e\nu_{en}} + \frac{g\cos I}{\nu_{en}}\hat{x}\right) \tag{4.12}$$

where ν_{in} and ν_{en} are the collision frequencies with neutral particles for ions and electrons, Ω_i and Ω_e are the ion and electron gyrofrequencies, m_i and m_e are the ion and electron masses, $g = |\,\boldsymbol{g}\,|$, e is the magnitude of the charge on the particles, and I is the magnetic dip angle. In the ionospheric F region the ratios of collision frequency and gyrofrequency are $1/\kappa_i = \nu_{in}/\Omega_i \ll 1$ for ions and $1/\kappa_e = \nu_{en}/\Omega_e \approx 0$ for electrons. Thus the above equations are approximated by

$$v_{\perp i} = \frac{c\boldsymbol{E}}{\kappa_i B} - \frac{c\boldsymbol{E}\times\hat{s}}{B} + \frac{g\cos I}{\Omega_i}\hat{x} \tag{4.13}$$

$$v_{\perp e} = -\frac{c\boldsymbol{E}\times\hat{s}}{B} \tag{4.14}$$

Here we define the following quantity:

$$\begin{aligned} j_{\perp i} &= en_i(v_{\perp i} - v_{\perp e}) \\ &= \frac{cen_i\boldsymbol{E}}{B\kappa_i} + eg\cos I\frac{n_i}{\Omega_i}\hat{x} \end{aligned} \tag{4.15}$$

Substituting (4.13) and (4.15) into (4.10) we have

$$\frac{\partial n_i}{\partial t} - c\,\nabla_\perp\cdot\left(n_i\frac{\boldsymbol{E}\times\hat{s}}{B}\right) + \frac{1}{e}\nabla_\perp\cdot j_{\perp i} = 0 \tag{4.16}$$

We suppose $\boldsymbol{E} = \boldsymbol{E}_0 + \boldsymbol{E}_1$ where $\boldsymbol{E}_0$ and $\boldsymbol{E}_1$ are background and perturbed states, respectively. The ambient $\boldsymbol{E} \times \boldsymbol{B}$ drift velocity is defined by $v_{E\times B} = -c(\boldsymbol{E}_0 \times \hat{s})/B$. Thus (4.16) is

$$\frac{\partial n_i}{\partial t} + v_{E\times B} \cdot \nabla n_i = c\,\nabla_\perp \cdot \left(n_i \frac{\boldsymbol{E}_1 \times \hat{s}}{B} \right) - \frac{1}{e} \nabla_\perp \cdot j_{\perp i} - n_i\, \nabla_\perp \cdot v_{E\times B} \tag{4.17}$$

The last term on the right-hand side of (4.17) is neglected since $\nabla_\perp \cdot v_{E\times B} \sim | v_{E\times B} | /r_0 \lesssim 10^{-5}\,\mathrm{sec}^{-1}$. The left-hand side of (4.17) denotes the change of the ion density in the frame moving with $v_{E\times B}$,

$$\frac{dn_i}{dt} = \frac{\partial n_i}{\partial t} + v_{E\times B} \cdot \nabla n_i \tag{4.18}$$

We assume $\boldsymbol{E}_0 = -\nabla\phi_0$, $\boldsymbol{E}_1 = -\nabla\phi_1$, and $\phi = \phi_0 + \phi_1$, and obtain

$$\frac{dn_i}{dt} = -\frac{cp^2}{r_0^2 B_0} \frac{\partial}{\partial\psi} \left(\frac{\partial\phi_1}{\partial p} n_i \right) + \frac{cp^2}{r_0^2 B_0 \zeta} \frac{\partial}{\partial p} \left(\zeta \frac{\partial\phi_1}{\partial\psi} n_i \right) - \frac{1}{e} \nabla_\perp \cdot j_{\perp i} \tag{4.19}$$

where $\zeta \equiv p^6 \sin^{12}\theta/\Delta^2$. The last term of (4.19) is

$$\frac{1}{e} \nabla_\perp \cdot j_{\perp i} = -\frac{cp}{r_0^2 \Delta B_0} \frac{\partial}{\partial\psi} \left(\frac{\partial\phi}{\partial\psi} \frac{n_i}{\kappa_i} \right) - \frac{cp^3\Delta}{r_0^2 B_0 \xi} \frac{\partial}{\partial p} \left(\xi \frac{\partial\phi}{\partial p} \frac{n_i}{\kappa_i} \right) + \frac{g\cos I}{p r_0 \sin^3\theta} \frac{\partial}{\partial\psi} \left(\frac{n_i}{\Omega_i} \right) \tag{4.20}$$

where $\xi \equiv p^7 \sin^{12}\theta/\Delta$.

We will investigate instability for the equation set (4.19) and (4.20) with the current conservation equation. Because the field aligned current vanishes at the ends of the magnetic field line, the current conservation equation is given as follows by integrating over the entire magnetic flux tube and taking summation for all ion species

$$0 = \sum_i \int (\nabla_\perp \cdot j_{\perp i})\, A ds \tag{4.21}$$

A Fourier analysis in ψ and t is applied for the perturbed states,

$$\phi_1 = \tilde{\phi}_1 \exp(i\omega t - im\psi) \tag{4.22}$$

$$n_i = n_{i0} + \tilde{n}_{i1} \exp(i\omega t - im\psi) \tag{4.23}$$

where n_{i0} is the background ion concentration. The ambient electric field, which has an equatorial strength of E_0^{eq}, is assumed to be eastward and to be independent of longitude,

$$E_0^{eq} = -\frac{1}{p r_0} \frac{\partial\phi_0}{\partial\psi} \qquad \frac{\partial\phi_0}{\partial p} = 0$$

$$\frac{\partial E_0^{eq}}{\partial\psi} = 0$$

The ion density is also assumed to be independent of longitude and in a quasi-equilibrium in the frame moving with $v_{E_0\times B}$,

$$\frac{\partial n_{i0}}{\partial\psi} = 0 \qquad \frac{dn_{i0}}{dt} = 0$$

Substituting (4.22) and (4.23) into (4.19) and (4.20) and neglecting higher order terms we have

$$i\omega\tilde{n}_{i1} = -\frac{icp^2 m\tilde{\phi}_1}{r_0^2 B_0 \zeta} \frac{\partial}{\partial p}(\zeta n_{i0}) - \frac{1}{e}(\nabla_\perp \cdot j_{\perp i}) \exp(-i\omega t + im\psi) \tag{4.24}$$

$$\frac{1}{e} \nabla_\perp \cdot j_{\perp i} \exp(-i\omega t + im\psi) = -\frac{imv_p}{p r_0 \Delta} \frac{\tilde{n}_{i1}}{\kappa_i} + \frac{cpm^2\tilde{\phi}_1}{r_0^2 \Delta B_0} \frac{n_{i0}}{\kappa_i} - \frac{img\cos I}{p r_0 \sin^3\theta} \frac{\tilde{n}_{i1}}{\Omega_i} \tag{4.25}$$

where $v_p = (cp^3 E_0^{eq})/B_0$ is the ambient $\boldsymbol{E} \times \boldsymbol{B}$ drift velocity at the equator. We define X, Y, Φ, and R_i by

$$X = \frac{cp^2}{r_0^2 B_0} \qquad Y = \frac{cp}{r_0^2 B_0}$$

$$\Phi = \exp(-i\omega t + im\psi)$$

$$R_i = \frac{v_p}{pr_0\Delta\kappa_i} + \frac{g\cos I}{pr_0\sin^3\theta\Omega_i}$$

Equations (4.24) and (4.25) are rewritten as follows,

$$i\omega\tilde{n}_{i1} = -im\tilde{\phi}_1 X\frac{1}{\zeta}\frac{\partial}{\partial p}(\zeta n_{i0}) - \frac{1}{e}(\nabla_\perp\cdot j_{\perp i})\Phi \tag{4.26}$$

$$\frac{1}{e}(\nabla_\perp\cdot j_{\perp i})\Phi = -imR_i\tilde{n}_{i1} + m^2\tilde{\phi}_1\frac{Y}{\Delta}\frac{n_{i0}}{\kappa_i} \tag{4.27}$$

Equations (4.21) and (4.27) yield

$$-i\sum_i\int R_i\tilde{n}_{i1}Ads + m\tilde{\phi}_1 Y\sum_i\int\frac{n_{i0}}{\Delta\kappa_i}Ads = 0 \tag{4.28}$$

To calculate the first term on the left-hand side of (4.28), we multiply both sides of (4.26) by R_i, then take integral over the flux tube and summation for all ion species,

$$i\omega\sum_i\int R_i\tilde{n}_{i1}Ads = -im\tilde{\phi}_1 X\sum_i\int\frac{R_i}{\zeta}\frac{\partial}{\partial p}(\zeta n_{i0})Ads - \frac{1}{e}\Phi\sum_i\int R_i(\nabla_\perp\cdot j_{\perp i})Ads \tag{4.29}$$

Although the current conservation (4.21) is satisfied, the second term on the right-hand side in (4.29) is not necessary zero. We carry out the same process against (4.27) and obtain

$$\frac{1}{e}\Phi\sum_i\int R_i(\nabla_\perp\cdot j_{\perp i})Ads = -im\sum_i\int R_i^2\tilde{n}_{i1}Ads + m^2\tilde{\phi}_1 Y\sum_i\int\frac{R_i n_{i0}}{\Delta\kappa_i}Ads \tag{4.30}$$

If $\ell = 1, 2, 3, \cdots$, we have general forms,

$$i\omega\sum_i\int R_i^\ell\tilde{n}_{i1}Ads = -im\tilde{\phi}_1 X\sum_i\int\frac{R_i^\ell}{\zeta}\frac{\partial}{\partial p}(\zeta n_{i0})Ads - \frac{1}{e}\Phi\sum_i\int R_i^\ell(\nabla_\perp\cdot j_{\perp i})Ads \tag{4.31}$$

$$\frac{1}{e}\Phi\sum_i\int R_i^\ell(\nabla_\perp\cdot j_{\perp i})Ads = -im\sum_i\int R_i^{\ell+1}\tilde{n}_{i1}Ads + m^2\tilde{\phi}_1 Y\sum_i\int\frac{R_i^\ell n_{i0}}{\Delta\kappa_i}Ads \tag{4.32}$$

Substituting (4.31) and (4.32) into (4.27) and setting $\gamma = i\omega$ we have

$$-X\sum_i\int\left[\left(\frac{mR_i}{\gamma}\right) + i\left(\frac{mR_i}{\gamma}\right)^2 - \left(\frac{mR_i}{\gamma}\right)^3 - \cdots\right]\frac{1}{\zeta}\frac{\partial}{\partial p}(\zeta n_{i0})Ads$$

$$+mY\sum_i\int\left[1 + i\left(\frac{mR_i}{\gamma}\right) - \left(\frac{mR_i}{\gamma}\right)^2 - \cdots\right]\frac{n_{i0}}{\Delta\kappa_i}Ads = 0 \tag{4.33}$$

We now estimate the small parameter mR_i/γ. R_i is less than $5\times10^{-8}\,\mathrm{sec}^{-1}$ because $|v_p| \lesssim 3\times10^3\,\mathrm{cm/sec}$, $r_0 \sim 6\times10^8\,\mathrm{cm}$, $g \sim 10^3\,\mathrm{cm/sec}^2$, $\kappa_i \gtrsim 100$, and $\Omega_i \sim 3\times10^2\,\mathrm{sec}^{-1}$ (O^+ ion at 250 km). If γ is the order of 1×10^{-3}, then for perturbations with scale lengths λ satisfying $\lambda = 2\pi r_0/m \gg 2\,\mathrm{km}$, higher order term of mR_i/γ can be neglected. Equation (4.33) is solved with respect to γ

$$\gamma = \frac{X\sum_i\int R_i\frac{1}{\zeta}\frac{\partial}{\partial p}(\zeta n_{i0})Ads}{Y\sum_i\int\frac{n_{i0}}{\Delta\kappa_i}Ads} \tag{4.34a}$$

or

$$= \frac{1}{\sum_i\int\frac{n_{i0}}{\Delta\kappa_i}Ads}\times$$

$$\left[\frac{v_p}{r_0}\sum_i\int\frac{1}{\Delta\kappa_i}\frac{1}{\zeta}\frac{\partial}{\partial p}(\zeta n_{i0})Ads + \frac{1}{r_0}\sum_i\int\frac{g\cos I}{\sin^3\theta\Omega_i}\frac{1}{\zeta}\frac{\partial}{\partial p}(\zeta n_{i0})Ads\right] \tag{4.34b}$$

4.3. Numerical computations

4.3.1. Mathematical formulation To calculate each term in (4.34), we obtain the unperturbed state of the ion distribution for O^+ and molecular ions by solving the ion continuity equation (4.8) incorporating an ambient electric field $\boldsymbol{E}_0$ and thermospheric winds in the magnetic meridional plane. Equation (4.8) is solved without neglecting any term in a reference frame moving with $\boldsymbol{E}\times\boldsymbol{B}$ drift velocity $v_{E\times B}$,

$$\frac{dn_i}{dt} = P_i - L_i - \frac{1}{A}\frac{\partial(An_i v_{\parallel i})}{\partial s} - n_i \nabla_\perp \cdot v_{E\times B} \tag{4.35}$$

where notations are the same as those appear in section 4.2. The last term on the right-hand side in (4.35) is given by (MURPHY *et al.*, 1983)

$$\nabla_\perp \cdot v_{E\times B} = \frac{6\sin^4\theta(1+\cos^2\theta)}{r(1+3\cos^2\theta)^2} v_p \tag{4.36}$$

where v_p is the $\boldsymbol{E}\times\boldsymbol{B}$ drift velocity at the equator that is given by a model based on observations and described later.

The field aligned ion velocity $v_{\parallel i}$ including diffusion and neutral wind effects is determined from the momentum equation,

$$-g\sin I - \frac{k_B T}{m_i n_i}\frac{\partial n_i}{\partial s} - \frac{k_B T}{m_i n_e}\frac{\partial n_e}{\partial s} - \frac{2k_B}{m_i}\frac{\partial T}{\partial s}$$

$$-\nu_{ij}(v_{\parallel i} - v_{\parallel j}) - \nu_{in}(v_{\parallel i} - v_n \cos I) = 0 \tag{4.37}$$

where ion and electron temperatures are assumed to be same as the neutral temperature described later ($T = T_i = T_e = T_n$) , k_B is Boltzmann's constant, ν_{ij} is the collision frequency between the i-th and the j-th ion species, ν_{in} is the collision frequency between i-th ion and neutral species, v_n is the magnetic meridional component of the neutral wind velocity given a model described later. The ion-neutral collision frequencies are given by (STUBBE, 1968; RAITT *et al.*, 1975)

$$\begin{aligned}
\nu_{O^+n} &= 3.42\times10^{-11} n(\mathrm{O}) T^{0.5}[1.04 - 0.064\log T]^2 \\
&\quad + 6.66\times10^{-10} n(\mathrm{O_2}) + 6.87\times10^{-10} n(\mathrm{N_2}) \\
&\quad + 1.29\times10^{-10} n(\mathrm{H}) + 1.32\times10^{-10} n(\mathrm{He}) \\
\nu_{H^+n} &= 6.61\times10^{-11} n(\mathrm{O}) T^{0.5}[1.0 - 0.047\log T]^2 \\
&\quad + 3.20\times10^{-9} n(\mathrm{O_2}) + 3.36\times10^{-9} n(\mathrm{N_2}) \\
&\quad + 1.37\times10^{-10} n(\mathrm{H}) T^{0.5}[1.4 - 0.117\log T]^2 \\
&\quad + 1.06\times10^{-9} n(\mathrm{He}) \\
\nu_{NO^+n} &= 2.64\times10^{-10} n(\mathrm{O}) + 4.28\times10^{-10} n(\mathrm{O_2}) + 4.34\times10^{-10} n(\mathrm{N_2}) \\
\nu_{O_2^+n} &= 2.50\times10^{-10} n(\mathrm{O}) \\
&\quad + 8.46\times10^{-11} n(\mathrm{O_2})[1.0 + 0.28\log T + 0.039(\log T)^2 + 0.0037(\log T)^3] \\
&\quad + 4.15\times10^{-10} n(\mathrm{N_2}) \\
\nu_{N_2^+n} &= 4.23\times10^{-10} n(\mathrm{O_2}) \\
&\quad + 7.64\times10^{-11} n(\mathrm{N_2})[1.0 + 0.38\log T + 0.072(\log T)^2 + 0.0091(\log T)^3]
\end{aligned}$$

To solve the equation set (4.35) and (4.37) we use the orthogonal coordinate system (p, q) defined by (4.3). The transformed diffusion equations for the four ion species are solved by an implicit finite difference method in the order of O^+, NO^+, O_2^+ and N_2^+ by using mathematical techniques which have been described by several authors (see BAILEY, 1983). In the calculation of the i-th ion species, because the equations are coupled to each other, the ion density and velocity of the j-th ion species at $t = t_1$ are replaced by the values calculated at the previous time step, $t = t_0$. After the evaluation of all ion species, the i-th ion density is recalculated using the coefficients involving the parameters for the j-th ion species at $t = t_1$. The calculations are continued until a consistent solution is obtained.

The equation set (4.35) and (4.37) only gives the one dimensional ion distribution along the particular magnetic field line that drifts with $v_{E\times B}$. We solve the same

equation set for magnetic field lines separated by 10 km in altitude at the equator.

4.3.2. Chemical reactions and parameters of neutral species In equation (4.35) the ion production rate P_i includes photoionization and charge exchange with the other ions, the ion loss rate L_i includes charge exchange and recombination. Chemical reactions relevant to the above productions and losses are summarized in Table 4.1. The photoionization rates for O^+, $O_2{}^+$ and $N_2{}^+$ at the top of the ionosphere (p_1, p_3, and p_4, respectively) are obtained by interpolating the results of TORR and TORR (1985) to an $F_{10.7}$ flux index of 200, where solar maximum conditions are assumed. For the photoionization rate for NO^+, p_2, the value used by ANDERSON and RUSCH (1980) is multiplied by 5.3 in accordance with $p_1 = 5.9 \times 10^{-7}\,\mathrm{sec}^{-1}$. The other reaction rates are similar to those used by ANDERSON and RUSCH (1980). Density of neutral species, $n(O)$, $n(N_2)$, $n(O_2)$, $n(H)$, and $n(He)$ is calculated from the empirical thermospheric model based on the mass spectrometer and incoherent scatter data (MSIS83) (HEDIN, 1983) with $F_{10.7} = 200$ and $A_p = 4$. The density of NO, $n(NO)$, which is not available from the MSIS83 model, is determined by the empirical relation (STUBBE, 1970)

$$n(\mathrm{NO}) = 2 \times 10^2 \exp(-3300/T_n) n(\mathrm{O_2}) + 5 \times 10^{-7} n(\mathrm{O})$$

where T_n is the neutral temperature determined from the MSIS83 model. The density of atomic nitrogen, $n(N)$, which is also unavailable from the model, is important to determine the NO^+ density since O_2^+ is converted to NO^+ through chemical reactions that include N (ANDERSON and RUSCH, 1980). However, $n(N)$ is neglected because we are not interested in the particular ion species but in the quantities appear in equation (4.34), and neglecting $n(N)$ does not yield a significant error in those quantities.

4.3.3. Vertical $\boldsymbol{E} \times \boldsymbol{B}$ drift velocity It is well known that the appearance of equatorial spread F highly depends on the layer height in the post sunset hours, which

TABLE 4.1. Reactions and Rate Coefficients

$O + h\nu$	$\longrightarrow$	$O^+ + e$	$p_1 = 5.9 \times 10^{-7}\,\mathrm{sec}^{-1}$
$NO + h\nu$	$\longrightarrow$	$NO^+ + e$	$p_2 = 2.7 \times 10^{-7}\,\mathrm{sec}^{-1}$
$O_2 + h\nu$	$\longrightarrow$	$O_2^+ + e$	$p_3 = 1.1 \times 10^{-6}\,\mathrm{sec}^{-1}$
$N_2 + n\nu$	$\longrightarrow$	$N_2^+ + e$	$p_4 = 7.4 \times 10^{-7}\,\mathrm{sec}^{-1}$
$O^+ + N_2$	$\longrightarrow$	$NO^+ + N$	$k_1 = 7.0 \times 10^{-13}\,\mathrm{cm}^3/\mathrm{sec}$
$O^+ + O_2$	$\longrightarrow$	$O_2^+ + O$	$k_2 = 2.0 \times 10^{-11}(300/T)^{0.5}\,\mathrm{cm}^3/\mathrm{sec}$
$O_2^+ + NO$	$\longrightarrow$	$NO^+ + O_2$	$k_3 = 4.4 \times 10^{-10}\,\mathrm{cm}^3/\mathrm{sec}$
$N_2^+ + O$	$\longrightarrow$	$NO^+ + N$	$k_4 = 1.4 \times 10^{-10}(300/T)\,\mathrm{cm}^3/\mathrm{sec}$
$N_2^+ + O_2$	$\longrightarrow$	$O_2^+ + N_2$	$k_5 = 1.0 \times 10^{-10}\,\mathrm{cm}^3/\mathrm{sec}$
$O_2^+ + e$	$\longrightarrow$	$O + O$	$\alpha_1 = 1.1 \times 10^{-5} T^{-0.7}\,\mathrm{cm}^3/\mathrm{sec}$
$NO^+ + e$	$\longrightarrow$	$N + O$	$\alpha_2 = 4.2 \times 10^{-7}(300/T)^{0.85}\,\mathrm{cm}^3/\mathrm{sec}$
$N_2^+ + e$	$\longrightarrow$	$N + N$	$\alpha_3 = 1.8 \times 10^{-7}\,\mathrm{cm}^3/\mathrm{sec}$

is caused by the pre-reversal enhancement of the upward $\boldsymbol{E}\times\boldsymbol{B}$ drift velocity (e.g. FARLEY *et al.*, 1970). Therefore, a realistic $\boldsymbol{E}\times\boldsymbol{B}$ drift model should be used in the quantitative discussion of the occurrence of ESF. The pre-reversal enhancement of drift varies in strength, duration, and time with the season and solar activity (FEJER *et al.*, 1979). Also the $\boldsymbol{E}\times\boldsymbol{B}$ drift may change with the longitudes. Unfortunately, very scarce data are available for the drift velocity except at Jicamarca (12°S, 76.9°W; dip≃1°N), near Lima, Peru (FEJER *et al.*, 1979), where a direct measurement of the drift velocity by a high power VHF radar has been conducted for a long period.

As the Jicamarca drift data are the most reliable ones and since ESF has been extensively studied at Jicamarca and other observatories close to it, we will first apply the calculation to Jicamarca data. Three average diurnal variations of the drift velocity (FEJER *et al.*, 1979) are reproduced in Figure 4.2 for summer solstice (D months; November to February), winter solstice (J months; May to August), and equinoxes (E months; February to May, and August to November) in solar maximum period.

Although reliability is not as good as the incoherent scatter radar results at Jicamarca, ABDU *et al.* (1981) have investigated drift of the ionosphere in the evening hours using ionosonde data from Fortaleza (3.3°S, 38°W; dip≃-2°), Brazil. They estimated the drift velocity by examining the time derivative of virtual height of the F_2 layer, $h'F_2$, which is assumed to provide the information of the layer height. Owing to the method they used, the drift velocity is reliable only for early evening hours or around pre-reversal enhancement, when the layer altitude is high and chemical processes do not affect the layer altitude very much.

As Fortaleza is at a longitude with a large magnetic declination angle (∼20°W) in contrast with Jicamarca where the declination is small (∼2°E), a large eastward zonal wind in the evening hours yields a large southward component of winds in the magnetic meridional plane irrespective of season. On the other hand, a meridional wind blows from the summer hemisphere to the winter hemisphere in the evening

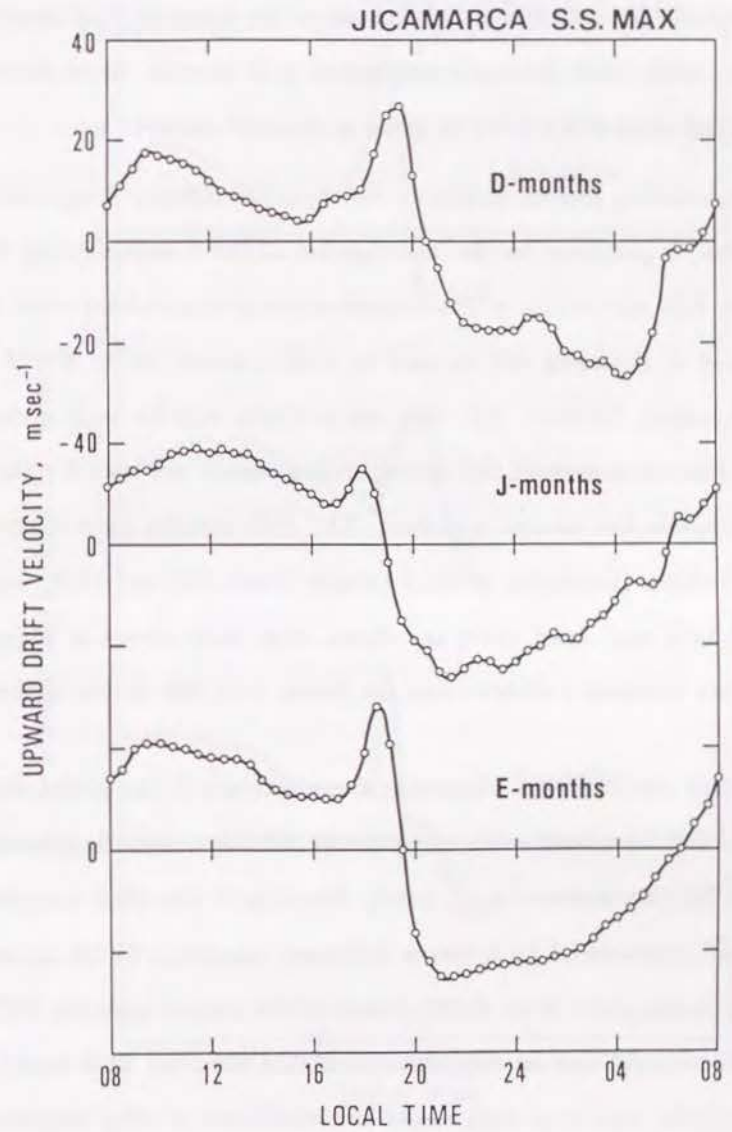

Fig. 4.2. Upward $\boldsymbol{E}\times\boldsymbol{B}$ drift velocity for typical seasons at Jicamarca under sun spot maximum condition (after FEJER *et al.*, 1979).

hours, i.e., southward in J months and northward in D months. As a result, large southward transequatorial flows of plasma along the magnetic field lines are expected in J months, while small flows are anticipated in D months. More discussion of the transequatorial neutral wind will be given in the next section.

Thus calculating plasma instability for these two different longitudes, Jicamarca and Fortaleza, is pertinent to the investigation of the transequatorial neutral wind effect on the ESF occurrence or the coupled seasonal-longitudinal effect of ESF. The data obtained at Fortaleza will be used to yield a second set of $\boldsymbol{E}\times\boldsymbol{B}$ drift velocities. Unfortunately, however, drift data are available only for early evening hours at Fortaleza. Jicamarca data in the corresponding season are used for the rest of the hours to complete the diurnal variation. The drift velocity data observed at Fortaleza for D months (December 1978), J months (June 1978 and 1979), and E months (September 1978 and April 1979) are shown with thick curves in Figure 4.3. The supplementary Jicamarca observations are shown with thin curves in the figure.

4.3.4. Neutral wind model Theoretical calculations of the global thermospheric neutral wind field have been made using the NCAR thermospheric general circulation model (TGCM) (Dickinson *et al.*, 1981). Recently, a simplified computer model of the wind field represented by a vector harmonic expansion (VSH model) has been constructed by Killeen *et al.* (1987) based on the output from the NCAR-TGCM. Zonal and meridional neutral winds are calculated from the VSH model for a given altitude, latitude, and local time under the conditions of solar maximum and December solstice. Zonal winds calculated from the VSH model at equatorial latitudes show fairly good agreement with those measured from the Wind and Temperature Experiment on the DE 2 satellite (Wharton *et al.*, 1984). The zonal winds measured by DE 2 seem to be the most comprehensive data set. Thus it is meaningful to compare the VSH model calculation and the DE 2 observations. The altitudes of the data from DE 2 measurement range from 200 km to 700 km, while most data

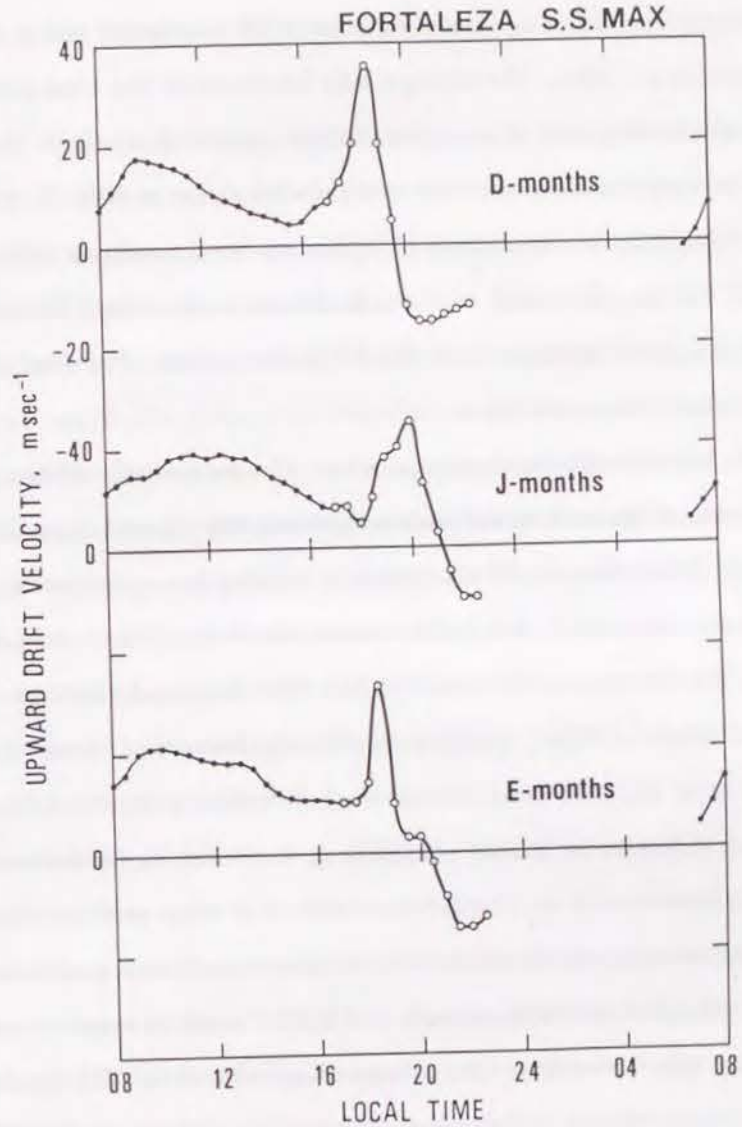

Fig. 4.3. Upward $\boldsymbol{E}\times\boldsymbol{B}$ drift velocity for typical seasons at Fortaleza under sun spot maximum condition. Open circles connected with thick curve are the velocity derived from ionosonde data (after Abdu *et al.*, 1981), and dots connected with thin curve are supplemental data from Jicamarca shown in Figure 4.2.

were obtained between 300 km and 400 km. The observations were made during the solar maximum period in agreement with the VSH calculation and at all local times (WHARTON *et al.*, 1984). We are especially interested in the wind in evening hours because equatorial spread F is a phenomenon appearing mostly in the post sunset hours. The observed eastward wind was 150~200 m/sec at 2000LT, while the wind from the VSH model at the altitude of 350 km reaches a maximum value of 110 m/sec at 2000LT. On the other hand, at the high altitude limit of the VSH model the wind seems to be in good agreement with the DE 2 observations. The disagreement at the lower altitudes is discussed below.

In the low-altitude thermosphere, where the ion-neutral collision frequency is large, solution of the neutral momentum equation may depend crucially on the electron density distribution model adopted since ion drag is a major deceleration mechanism. The electron density distribution model used in the VSH model (or the NCAR-TGCM) is the one supplied by CHIU (1975). According to ANDERSON *et al.* (1987) the F layer height of Chiu's model is significantly lower than observed at the magnetic equator in the post sunset hours. Such difference in layer height would cause a significant difference in the ion-neutral drag coefficient in the neutral momentum equation. ANDERSON *et al.* (1982) have shown that when realistic electron density distributions are adopted, the NCAR-TGCM model produces a maximum zonal wind velocity of 300 m/sec at 300 km altitude and 2000LT near the magnetic equator. This value is more than three times the corresponding value of the VSH model. However, observation supports such a high zonal wind velocity. SIPLER *et al.* (1983) observed wind velocity of ~300 m/sec by an optical method at Kwajalein (9.4°N, 167.5°E; dip≃4.3°N), Marshall Islands, under solstice and solar maximum conditions, although the maximum velocities during most nights are 150 to 200 m/sec, which are still larger than the VSH model calculations.

Turning to the meridional winds, there are no observational results like the DE 2 data to be compared with the VSH model calculations. Maximum southward velocities observed by an optical method at Kwajalein (SIPLER *et al.*, 1983) on five days in July 1979 exceed 100 m/sec. These are about twice the VSH model value at the altitude of 300 km.

At present, there seem to be no reliable observations of neutral winds except for the zonal wind by DE 2 at the altitude of 300 to 400 km with which we may construct a wind model for the ionospheric modeling. As a conclusion, the VSH model for the neutral wind field is very attractive for our purpose because it provides full diurnal variations for both zonal and meridional winds on a consistent basis, except for the fact that those amplitudes of the wind velocities may be somewhat underestimated. On the basis of the above discussion, we adopt the high altitude limit of the wind from the VSH model for the altitudes higher than 300 km, i.e., no height variation of the wind velocity at these altitudes is assumed. At the altitudes lower than 300 km, the model velocity reaches gradually to the VSH value. Furthermore, for simplicity, no latitude variation is assumed. The magnetic meridional component of the wind is calculated by using the magnetic declination angle of 2°E for Jicamarca and 20°W for Fortaleza. As the output from the present version of the VSH model is only for the December solstice (KILLEEN *et al.*, 1987) the sign of the meridional component is reversed for the June solstice. For the equinoxes, no meridional wind is assumed.

The calculated diurnal variations of the wind component in the magnetic meridional plane are shown in Figure 4.4 for Jicamarca. Because of the small magnetic declination angle at Jicamarca, the seasonal wind blowing from the summer hemisphere to the winter hemisphere, i.e., north to south in J months and south to north in D months, is the major cause of the transequatorial wind in the magnetic meridional plane. The transequatorial winds in the magnetic meridional plane attain to maximum values in the solstices (solid and dash-dotted curves in Figure 4.4), and no transequatorial wind in the equinoxes (dashed curve). The results for Fortaleza are shown in Figure 4.5. In contrast to Jicamarca, at Fortaleza where the magnetic declination angle is abut 20°W, the eastward zonal wind in the evening hours yields

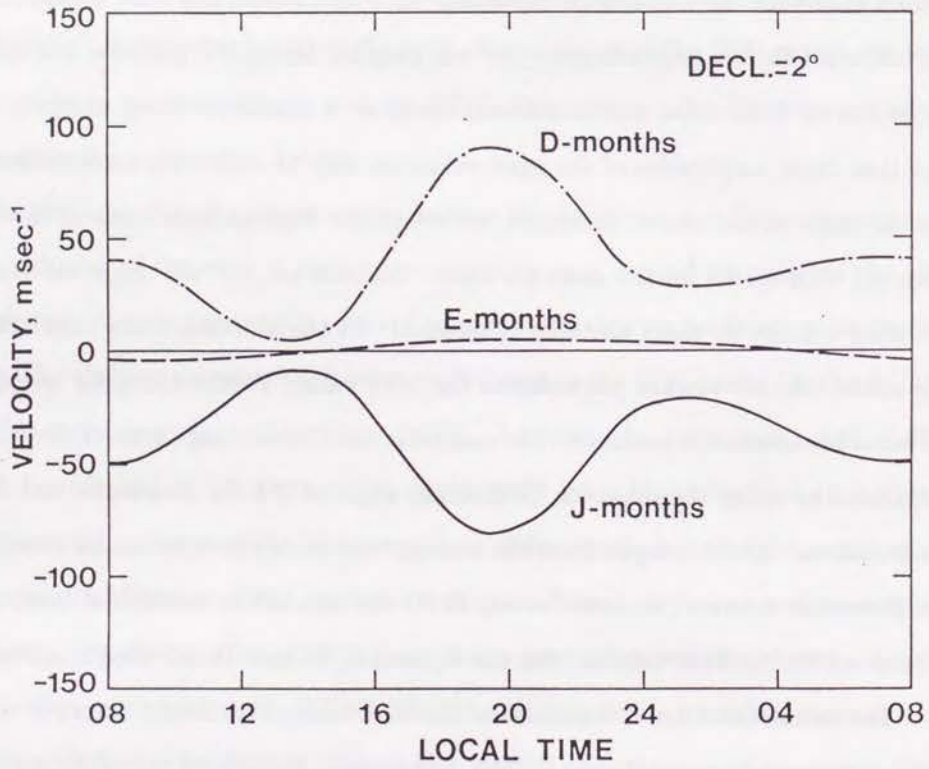

Fig. 4.4. Magnetic meridional component of the thermospheric neutral wind. Magnetic declination angle is 2° E being pertinent to the longitude of Jicamarca.

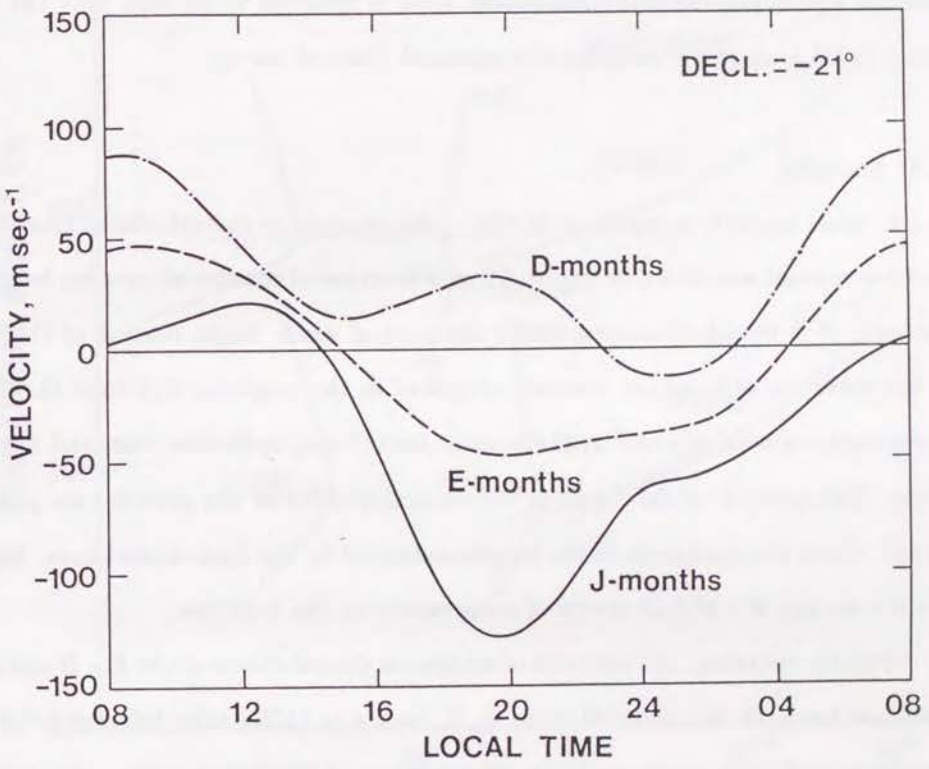

Fig. 4.5. Same as Figure 4.4 except for magnetic declination angle of 21° W which is pertinent to Fortaleza.

an appreciable southward component in the magnetic meridional plane. Conversely the seasonal wind is northward in the December solstice. As a result, the total wind component in the magnetic meridional plane for the December solstice becomes small (dash-dotted curve in Figure 4.5). On the contrary, for the June solstice, the total wind component in the magnetic meridional plane becomes very large (solid curve). For the equinoxes, since the meridional wind is assumed to be zero only the zonal wind yields a magnetic meridional component (dashed curve).

4.4. Results

4.4.1. Most unstable magnetic field line An example of the calculated growth rate and ion content are shown in Figure 4.6 as a function of equatorial crossing height for the case of D months/Jicamarca with the neutral wind. Right portion of the figure is the variation of total ion content integrated in the magnetic flux tube that has a cross sectional area of $1\,\mathrm{cm}^2$ at the equator for O^+ ion, molecular ions, and a sum of them. Left portion of the figure is the vertical profiles of the growth rate given by (4.34), which are maximum at the heights indicated by the dash-dotted lines. Dashed arrows are the $\boldsymbol{E}\times\boldsymbol{B}$ drift traces of some points on the field line.

Strictly speaking, the altitudes of maximum contributions of the $\boldsymbol{E}\times\boldsymbol{B}$ and gravitational terms do not coincide since κ_i, Ω_i, and g in (4.34) take different height dependence and both terms are different functions of those parameters. As a result, the altitude of the maximum growth rate (a sum of the $\boldsymbol{E}\times\boldsymbol{B}$ term and the gravitational term) is not necessarily fixed in the reference frame moving with the ambient $\boldsymbol{E}\times\boldsymbol{B}$ drift velocity. However, as shown in the figure, the altitude of the maximum growth rate only differs by 10 km in the reference frame of the drifting ionosphere during hours when the maximum growth rate is high viz. $\gtrsim 1\times10^{-3}\,\mathrm{sec}^{-1}$. This is also true for the other cases. The discussion in this thesis is restricted to the linear regime, and perhaps until the depletion grows to a few percent out of thermal noise. According to ANDERSON and HAERENDEL (1979), the additional $\boldsymbol{E}\times\boldsymbol{B}$ drift velocity

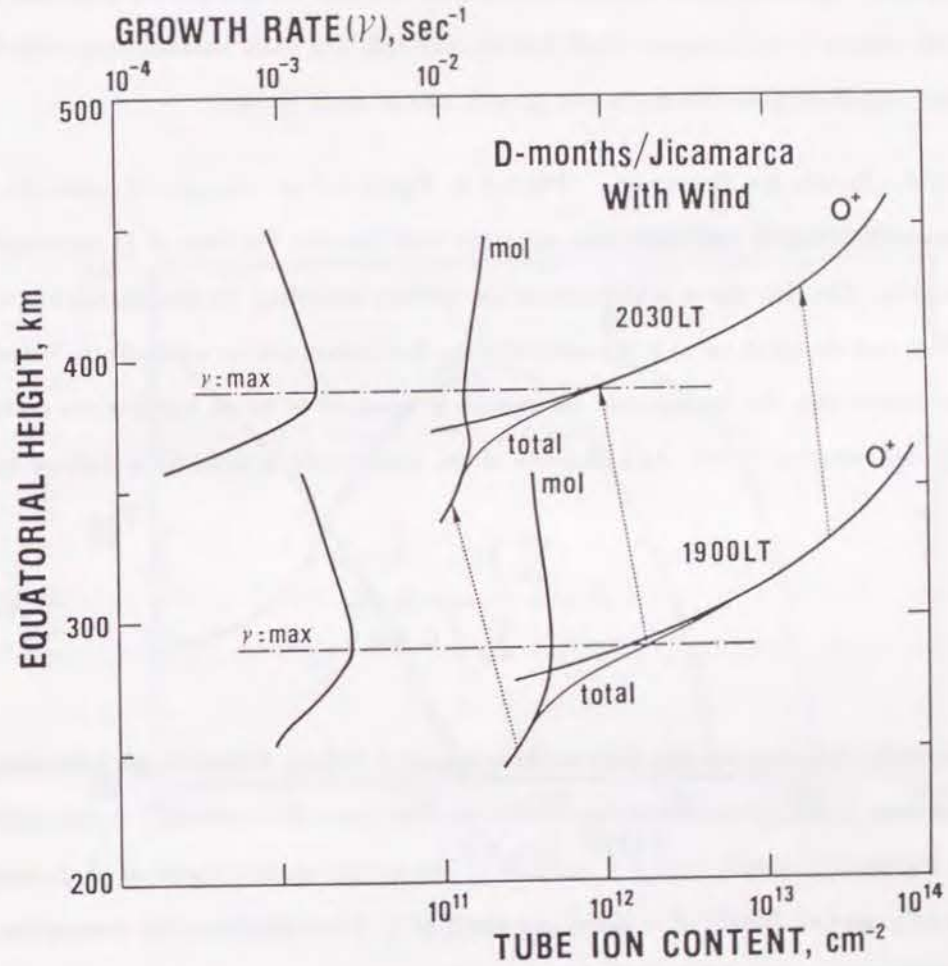

Fig. 4.6. Vertical profiles of linear growth rates (left portion) and tube integrated ion contents (right portion) for the two local times as a function of equatorial crossing height of the field line. The tube integrated ion contents are separately plotted for O^+, some of molecular ions (NO^+, O_2^+, and N_2^+; denoted as "**mol**") and their sum (denote as "**total**"). The dash-dotted lines indicate the altitude of maximum growth rate. The calculation is made under the condition of D months/Jicamarca including the thermospheric wind effect.

due to the instability for a bubble with 5% depletion is less than 1 m/sec. In this regime it is assumed that a perturbed region also drifts with the ambient $\boldsymbol{E} \times \boldsymbol{B}$ drift velocity. Therefore, it is convenient to discuss the time evolution of the growth rate with respect to the magnetic field line we may call "the most unstable magnetic field line" which exhibits the maximum growth rate at most times.

4.4.2. Results for Jicamarca Plotted in Figure 4.7 are the growth rates for the above determined most unstable magnetic field line for the case of D months/Jicamarca. The thin curve is the calculation without including the thermospheric wind effect and the thick curve is the one including the thermospheric wind effect. We must remember that the background ionosphere is assumed to be an equilibrium state in the derivation of (4.34). As a measure of the equilibrium, a quantity is defined by

$$\bar{\beta} = \frac{\sum_i \int (L_i - P_i) A ds}{\sum_i \int n_i A ds} \tag{4.38}$$

where the notations are the same as those appeared before. When the photoionization is absent, (4.38) gives a mean loss coefficient. The mean loss coefficient is also plotted in Figure 4.7. Until 1815LT $\bar{\beta}$ exceeds γ. At around sunset, however, $\bar{\beta}$ decreases rapidly, and at 1900LT $\bar{\beta}$ is about one tenth of γ. After this time the assumption of equilibrium may well be satisfied.

The time evolution of the maximum growth rate exhibits a peak around 2000LT (no wind) and around 1930LT (with wind) with both maxima occurring before the ambient drift changes the direction from upward to downward. The growth rate after all goes down to small values at ~2200LT (no wind) and at ~2115LT (with wind). Such a general view of the time evolution of the growth rate is already well explained as follows. The evening pre-reversal enhancement of the upward plasma drift raises the layer to a high altitude, which not only results in favorable conditions for the

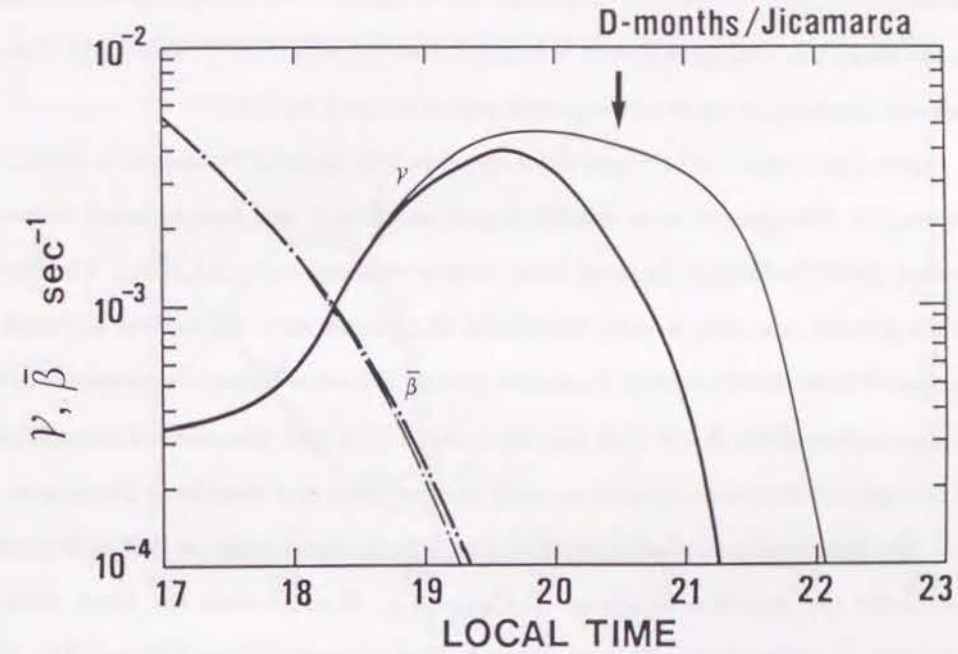

Fig. 4.7. Evolution of the linear growth rate and the mean loss coefficient for the D months/Jicamarca calculations. The altitude follows the most unstable magnetic field line (see text) which moves with $\boldsymbol{E} \times \boldsymbol{B}$ drift velocity. The vertical arrow indicates the reversal time of the ambient $\boldsymbol{E} \times \boldsymbol{B}$ drift.

gravitational Rayleigh-Taylor instability but the large eastward electric field itself causes the $\boldsymbol{E}\times\boldsymbol{B}$ drift instability. After the vertical drift changes the sign (this is a usual pattern) the $\boldsymbol{E}\times\boldsymbol{B}$ term acts as a stabilizing factor opposite to the gravitational term.

Comparing the two curves for the growth rate in Figure 4.7, we notice an effect of the thermospheric wind clearly. The effect is most remarkable after 1945LT when the growth rates start to decrease. Note the loss coefficient is small by this time. Owing to the wind, the peak growth rate is reduced from $4.7\times10^{-3}\,\mathrm{sec}^{-1}$ to $4.0\times10^{-3}\,\mathrm{sec}^{-1}$ and the duration of the positive growth rate is reduced by 1 h.

The time evolution of γ and $\bar{\beta}$ for the case of J months/Jicamarca is plotted in Figure 4.8. The growth rates exhibit a peak at 1815LT and turn to small values at around 1900LT~1915LT for cases both with or without the wind effect. The curves of the growth rate shift to early hours and the growth rates themselves are weak as compared with the D months/Jicamarca results. All these features correspond to the characteristics of the $\boldsymbol{E}\times\boldsymbol{B}$ drift velocity model, i.e., a weak pre-reversal enhancement of the upward drift velocity and an early reversal time in J months at Jicamarca.

The thermospheric wind velocity in J months is almost same as that in D months except for the direction as shown in Figure 4.4. Nevertheless, the wind effect in J months is quite small. This weak wind effect is explained as follows. The drift reversal time is so early that the large asymmetry in the ion distribution is not attained yet when the drift velocity changes sign. The small pre-reversal enhancement of the drift velocity does not lift the layer to a high altitude and the gravitational term in the growth rate is small. Once the drift reverses, the $\boldsymbol{E}\times\boldsymbol{B}$ term plays a stabilizing factor. In conjunction with the small gravitational term, the growth rate becomes negative soon after the reversal irrespective of the wind effect.

We now compare the results with the observations. There is, however, a problem for a quantitative discussion, since the instability model is valid only when the background ionosphere is in equilibrium. When the growth rate first exceeds $10^{-3}\,\mathrm{sec}^{-1}$

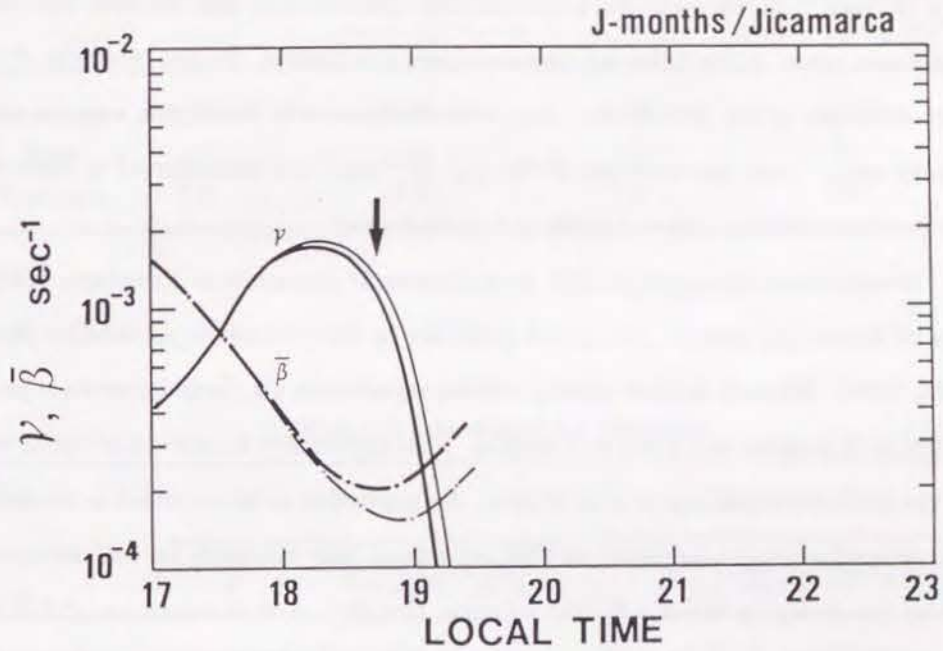

Fig. 4.8. Same as Figure 4.7 except for the J months/Jicamarca calculations.

at around sunset $\bar{\beta}$ is still $\sim 10^{-3}\,\mathrm{sec}^{-1}$. We are not allowed to subtract $\bar{\beta}$ from γ to obtain an effective growth rate as in a local theory (HANSON *et al.*, 1986), because the regions of rapid recombination of the molecular ions (at the same time there are productions due to the charge exchange with O^+) and large ion density gradient do not necessarily coincide. However, if we assumed $\gamma - \bar{\beta}$ gives an effective growth rate as a very rude measure, $\gamma - \bar{\beta}$ exceeds $10^{-3}\,\mathrm{sec}^{-1}$ about 15 min later. Thus we choose $\gamma \geq 10^{-3}\,\mathrm{sec}^{-1}$ to represent a duration of large growth rate, and this may not yield significant errors in the following discussion and conclusions. Because features of the time evolution of the growth rate vary with the seasons in a complex way the peak growth rate, Γ, and the duration, T, for $\gamma \geq 10^{-3}\,\mathrm{sec}^{-1}$ are summarized in Table 4.2 for the three seasons with and without the wind effect.

Observations of range type ESF by a bottomside ionosonde at Huancayo, 160 km east of Jicamarca, reveal a seasonal dependence in the occurrence probability (RASTOGI, 1980). There is marked winter/summer asymmetry, i.e., large occurrence probability in D months and small in J months. This asymmetry is reproduced quite well by the present calculations with or without the wind effect as summarized in the table. The winter/summer asymmetry of ESF occurrence may therefore be well accounted for by the change in the $\boldsymbol{E} \times \boldsymbol{B}$ drift velocity. However, close examination of ESF by RASTOGI (1980) shows that the maximum occurrence of ESF is not exactly in the December solstice but is slightly shifted toward equinoxes forming two peaks. Also gigahertz scintillations at Arequipa and Huancayo, both in Peru, show equinoctial maxima in occurrence (DASGUPTA *et al.*, 1982). To reproduce these two occurrence maxima with a model calculation, we need more detailed $\boldsymbol{E} \times \boldsymbol{B}$ drift model because the $\boldsymbol{E} \times \boldsymbol{B}$ drift velocity data used here are an average over three months centered at the solstices and equinoxes. The observations that should be compared with the current calculations are therefore average occurrence probability over three months centered at the equinox or at the solstice. The percentage occurrences averaged by eye from the Rastogi's (1980) data (his Figure 4) for the equinox and the December

TABLE 4.2. Summary for Jicamarca

	No Wind		With Wind	
	Γ	$T(\gamma \geq 10^{-3}\,\mathrm{s}^{-1})$	Γ	$T(\gamma \geq 10^{-3}\,\mathrm{s}^{-1})$
December	$4.7 \times 10^{-3}\,\mathrm{s}^{-1}$	216 min	$4.0 \times 10^{-3}\,\mathrm{s}^{-1}$	145 min
June	1.8	73	1.7	70
Equinox	3.5	110	3.5	110

TABLE 4.3. Summary for Fortaleza

	No Wind		With Wind	
	Γ	$T(\gamma \geq 10^{-3}\,\mathrm{s}^{-1})$	Γ	$T(\gamma \geq 10^{-3}\,\mathrm{s}^{-1})$
December	$4.7 \times 10^{-3}\,\mathrm{s}^{-1}$	180 min	$4.5 \times 10^{-3}\,\mathrm{s}^{-1}$	160 min
June	7.0	> 230	3.4	156
Equinox	3.5	174	3.5	159

solstice are almost same value. Turning to the summary in Table 4.2, we conclude the calculation including the wind effect is closer to the observations than the calculation without including the wind effect.

4.4.3. Results for Fortaleza As we saw in the results for Jicamarca, the thermospheric winds and background electric fields are equally important for the occurrence of equatorial spread F. Especially in J months the wind significantly reduces the growth rate. Now we will apply the instability model to Fortaleza. At the longitude of Fortaleza a component of the wind in the magnetic meridional plane becomes quite large in J months owing to the large magnetic declination angle; the occurrence of spread F is anticipated to be much more affected by the wind than the other longitudes and seasons.

The calculated growth rates for J months/Fortaleza are shown in Figure 4.9. As mentioned already, the drift velocity is reliable only for the early evening; therefore the growth rates are not calculated for local time after 2230LT. The thin curve represents the calculation without including the wind effect. The long duration of positive growth rate and the large peak growth rate correspond to the lengthy and late pre-reversal enhancement of the $\boldsymbol{E}\times\boldsymbol{B}$ drift velocity model. The thick curve is for the results including the wind effect. As expected from the large wind velocity in Figure 4.5, the growth rate is significantly reduced. Over all trend of the wind effect is similar to that in the D months/Jicamarca case.

The results for D months/Fortaleza are shown in Figure 4.10. In contrast to J months the reduction of the growth rate due to the wind effect is quite small in accord with a small wind component in the magnetic meridian.

Table 4.3 summarizes the results for Fortaleza, which are compared with observations below. The range type spread F at Fortaleza as observed by the bottomside ionosonde also shows seasonal variations. Percentage occurrences of range spread F in D months and E months at around evening hours are $\gtrsim 90\%$, while that in J months

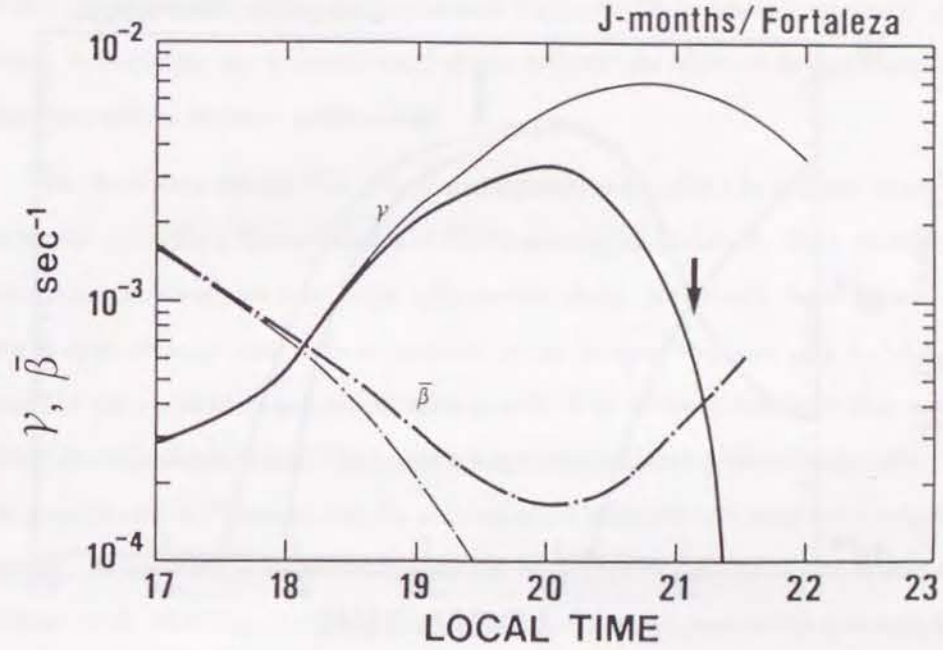

Fig. 4.9. Same as Figure 4.7 except for the J months/Fortaleza calculations.

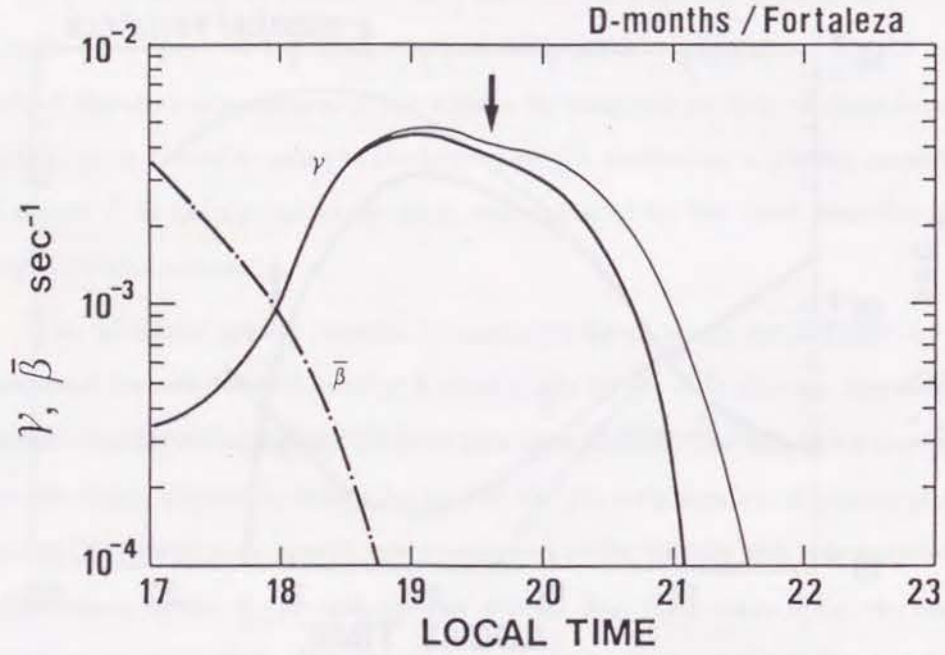

Fig. 4.10. Same as Figure 4.7 except for the D months/Fortaleza calculations.

is only 50% (ABDU *et al.*, 1981). These seasonal variations are opposite to the calculation without including the wind effect as shown in Table 4.3. Thus the background electric fields that change with season do not explain the observations at Fortaleza when the wind effect is absent. When the wind effect is included, the peak growth rate for J months is reduced by half but that for D months remains almost unchanged. As a result, the peak growth rate for D months exceeds that for J months. The duration T in J months is also reduced so much that Ts for the three seasons are nearly equal value. Accordingly the seasonal trend of the growth rate becomes in agreement with the observations at least qualitatively.

We have seen above that the thermospheric wind effect is a quite important factor for controlling the occurrence of ESF especially at Fortaleza. For a quantitative discussion, however, we need more information about the electric fields because the $\boldsymbol{E}\times\boldsymbol{B}$ drift velocity used here is obtained by an indirect way and only for the time near the pre-reversal enhancement after sunset. Also we need sufficient observations about thermospheric winds. Of course a larger neutral wind yields a larger effect and the growth rate in J months may be reduced much more when a large wind velocity is applied. At any rate, seasonal changes in the range spread F observations at Fortaleza (ABDU *et al.*, 1981) are never explained without taking account of the thermospheric wind effect.

4.4.4. Transequatorial wind effect The suppression of the growth rate due to the transequatorial wind is investigated in more detail based on the results of the first set of runs, D months/Jicamarca. The above wind effect is due to the change in the ion distribution along the magnetic field line. We examine how the change in ion distribution affects the other parameters for the magnetic field line that exhibits maximum growth rate. Figure 4.11 shows the ion density and each term that appears in (4.34) as a function of distance from the equator along the magnetic field line. The local time is 1930LT, when the upward $\boldsymbol{E}\times\boldsymbol{B}$ drift velocity is maximum. The terms

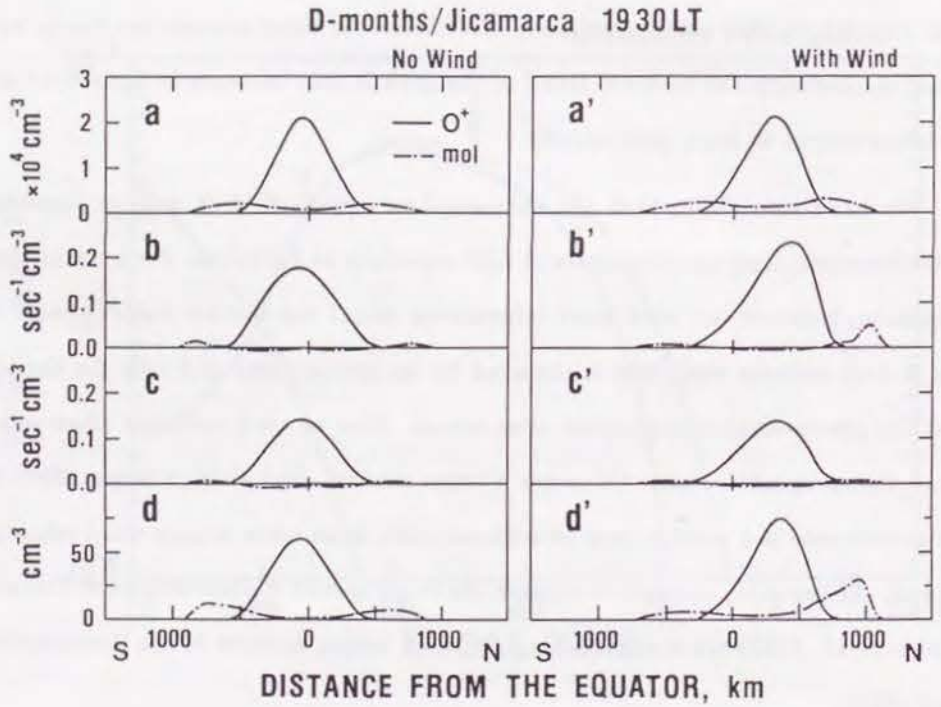

Fig. 4.11. Magnetic field aligned distribution of various parameters as a function of distance from the equator for D months/Jicamarca runs. Each panel is, from top to bottom, ion density, the $\boldsymbol{E}\times\boldsymbol{B}$ term, the gravitational term, and the n/κ term for the two cases with (right) and without (left) the wind effect. The equatorial crossing altitude of the magnetic field line is about 340 km where the growth rate is maximum. The local time is 1930 when the $\boldsymbol{E}\times\boldsymbol{B}$ drift velocity is maximum.

are defined by using the same notation in (4.34)as follows: Figures 4.11a, a' are ion density, $n_{10}A$ for O^+ ion and $\sum_{i=2}^{4} n_{i0}A$ for molecular ions, Figures 4.11b, b' are the $\boldsymbol{E}\times\boldsymbol{B}$ term,

$$\frac{v_p}{r_0}\frac{1}{\Delta\kappa_1}\frac{1}{\zeta}\frac{\partial}{\partial p}(\zeta n_{10})A \qquad \text{for } O^+ \text{ ion}$$

$$\frac{v_p}{r_0}\sum_{i=2}^{4}\frac{1}{\Delta\kappa_i}\frac{1}{\zeta}\frac{\partial}{\partial p}(\zeta n_{i0})A \qquad \text{for molecular ions}$$

Figures 4.11c, c' are the gravitational term,

$$\frac{1}{r_0}\frac{g\cos I}{\sin^3\theta\Omega_1}\frac{1}{\zeta}\frac{\partial}{\partial p}(\zeta n_{10})A \qquad \text{for } O^+ \text{ ion}$$

$$\frac{1}{r_0}\sum_{i=2}^{4}\frac{g\cos I}{\sin^3\theta\Omega_1}\frac{1}{\zeta}\frac{\partial}{\partial p}(\zeta n_{10})A \qquad \text{for molecular ions}$$

and Figures 4.11d, d' are n/κ that is directly related with the Pedersen conductivity,

$$\frac{n_{10}}{\Delta\kappa_1}A \qquad \text{for } O^+ \text{ ion} \qquad\qquad \sum_{i=2}^{4}\frac{n_{i0}}{\Delta\kappa_i}A \qquad \text{for molecular ions}$$

The left four panels in Figure 4.11 are for the calculation without including the wind. The ion density and other terms are quite symmetric with respect to the equator. A contribution from the molecular ions (dash-dotted curve) is most apparent in the n/κ term (Figure 4.11d), while it is small in the gravitational term (Figure 4.11c). This implies that the molecular ion dominated region acts as a load on the perturbed electric fields due to the gravitational Rayleigh-Taylor instability near the equator.

The right four panels in Figure 4.11 are the calculation including the wind. The ion distribution (Figure 4.11a') shifts toward north by 400 km owing to the northward wind. The shapes of the distribution of O^+ and molecular ions, however, are

not changed very much. While, for the molecular ions in the $\boldsymbol{E}\times\boldsymbol{B}$ term (Figure 4.11b') and n/κ (Figure 4.11d') the curves are largely deformed in addition to the northward shift. Especially note that the n/κ term of the molecular ions in the northern hemisphere is quite large while that in the southern hemisphere is negligible. These are well explained by the change in altitude because $1/\kappa_i(=\nu_{in}/\Omega_i)$ increases exponentially with lowering altitude. Another feature to be noted is the O^+ ion curve for the $\boldsymbol{E}\times\boldsymbol{B}$ term (Figure 4.11b') that shifts further to the north than the corresponding ion distribution function (Figure 4.11a'). Furthermore, the maximum value is more than 30% larger than the calculation without the wind (Figure 4.11b). This is also a result of the change in altitude. As a net effect of the wind, the increase of n/κ (molecular ions) cancels the increase of the $\boldsymbol{E}\times\boldsymbol{B}$ term (O^+ ions). Thus the growth rate does not change very much at all as we have seen in Figure 4.7, even though the thermospheric wind changes the field aligned distribution of ions.

Figure 4.12 is the same as Figure 4.11 except that the local time is 2030LT when the $\boldsymbol{E}\times\boldsymbol{B}$ drift velocity is zero (the $\boldsymbol{E}\times\boldsymbol{B}$ term vanishes) and the layer is highest. The left four panels without including the wind again indicate a symmetric distribution with respect to the equator. In the right four panels including the wind, distribution functions are shifted further toward north as compared with those for 1930LT. The contribution of the molecular ions in the n/κ term is significantly large. In the gravitational term, however, the contribution from the molecular ion is so small to be neglected. As a net effect, the growth rate is reduced to about one third of that obtained by the calculation without including the wind as shown in Figure 4.7.

4.5. Concluding remarks

To study the seasonal-longitudinal effect of ESF numerically, we have developed a diagnostic model and applied it to various cases in which the ionospheric parameters are determined by solving a continuity equation under variable conditions including ambient electric fields and transequatorial thermospheric winds. The instability model

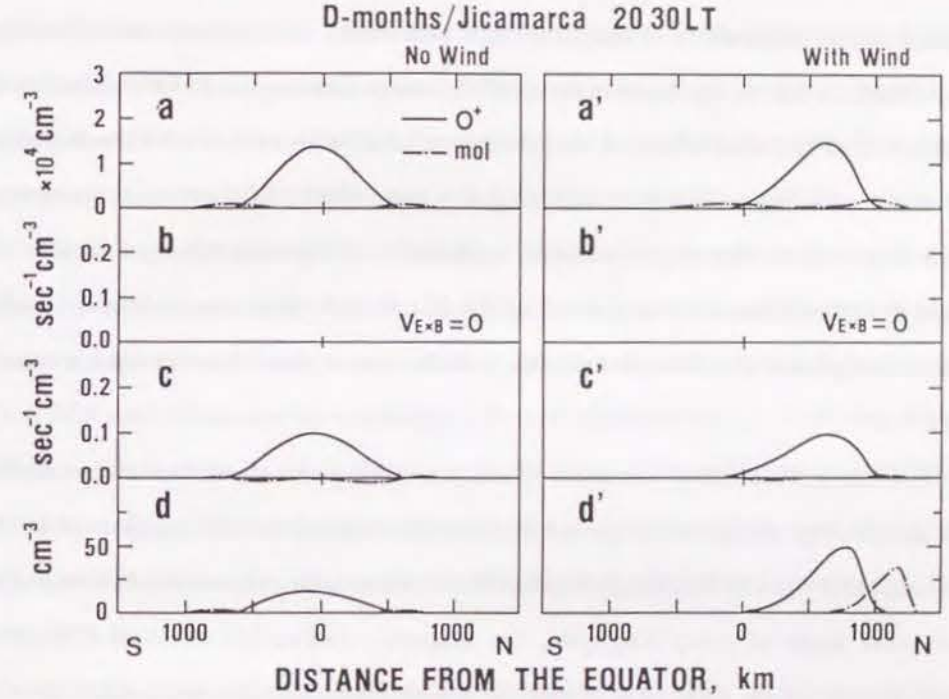

Fig. 4.12. Same as Figure 4.11 except that the local time is 2030LT when the $\boldsymbol{E}\times\boldsymbol{B}$ drift velocity is zero and the equatorial crossing altitude of the magnetic field line is about 390 km.

contains effects of the F region plasma away from the equatorial plane and the $\boldsymbol{E}\times\boldsymbol{B}$ drift effect.

The transequatorial wind and the $\boldsymbol{E}\times\boldsymbol{B}$ drift are equally important for controlling the generation of equatorial spread F. A large wind velocity significantly reduces the instability growth rate, even if a large upward $\boldsymbol{E}\times\boldsymbol{B}$ drift velocity is applied. The wind effect is more prominent when the reversal time of the $\boldsymbol{E}\times\boldsymbol{B}$ drift is late. The winter/summer asymmetry of the occurrence probability at Jicamarca and other stations close to it can be explained in terms of the seasonal change in $\boldsymbol{E}\times\boldsymbol{B}$ drift velocity irrespective of the wind effect. A morphology over all seasons indicates much better agreement with the calculations including the wind effect. Without taking account of the wind effect, the winter/summer asymmetry of the occurrence of equatorial spread F at Fortaleza is not explained by the $\boldsymbol{E}\times\boldsymbol{B}$ drift effect. An instability model incorporating both $\boldsymbol{E}\times\boldsymbol{B}$ drift and wind effects can explain the observed seasonal trend.

The current results of the wind effect are a key point to understand a worldwide morphology of equatorial spread F. Since the transequatorial component of the thermospheric wind in the magnetic meridional plane is determined by the magnetic declination angle at every longitude, the magnetic declination effect of ESF or a seasonal-longitudinal effect of ESF may be well explained by the wind effect investigated here. However, a possible longitudinal change in the $\boldsymbol{E}\times\boldsymbol{B}$ drift pattern could be equally important and is not known at this time.

Chapter 5: Irregularities at off-Equatorial Latitudes

5.1. Introduction

The discussion in this chapter is related with two more features of equatorial spread F; one is the latitudinal extent of the ESF region, and the other is the density enhancements or plasma blobs observed at the satellite heights associated with topside spread F near the equator. As we have seen in Chapter 2, the occurrence probability and strength of the equatorial spread F are maximum at the magnetic equator and decrease with latitudes. Although the midlatitude ionosphere is relatively quiescent compared with the other latitudes, it still contains irregular structure, which may be morphologically distinguished from that of ESF. The transition regions from the spread F active equatorial region to the quiescent midlatitudes, or rim regions of ESF zone, are not discussed very much until now, where some properties may be concerned with ESF and others may be concerned with midlatitude spread F. Studying the transition region, in turn, is a help for the understanding of the midlatitude irregularities; our knowledge of the midlatitude irregularities is quite poor compared with that of equatorial latitudes. Full discussion of midlatitude irregularities, however, is beyond of this thesis.

In the next section, as a preliminary discussion, we briefly review the latitudinal extent of the equatorial spread F. Section 5.3 describes an instability model and numerical calculations that yields the linear growth rate for the Rayleigh-Taylor and the $\boldsymbol{E}\times\boldsymbol{B}$ drift instabilities involving plasma in the entire magnetic flux tube, based on the result of Chapter 4. The ion distribution along the field line is obtained by solving the ion continuity equations for O^+ and H^+ ions. Description of the ionospheric modeling follows. Before presenting the results of growth rate, the response of the F layer to the eastward electric field is examined and the limit of the equilibrium assumption is tested. Finally, in section 5.4, the results of the growth rate are compared with observations.

5.2. Latitudinal extent of ESF

During nighttime in the equatorial F region, an irregular structure first appears at the bottomside where the ionosphere is unstable, then plasma-depleted region penetrates into the topside ionosphere by buoyancy force due to a nonlinear Rayleigh-Taylor process (WOODMAN and LAHOZ, 1976; OSSAKOW, 1981). The upward drift of the plasma-depleted region or plasma bubble ceases near the altitude where the ambient electron density is equal to that inside the bubble. This determines the maximum altitude of plasma bubbles and the latitudinal extent of equatorial spread F. This explanation of the latitude extension of ESF, however, is too primitive to apply real problems. In general, it is not easy to determine whether observed irregularities at subtropical latitudes originate from a plasma bubble or are locally generated at those latitudes.

From observations of medium frequency ducts by means of topside sounder, MULDREW (1980*a*) has suggested that, on a statistical basis, irregularities causing ducted echoes at altitudes corresponding to $L \gtrsim 1.2$ are not due to a rising plasma bubble. There are other observations of irregularities which cannot be explained by the rising plasma bubble. One example of them is a topside plasma blob or electron density enhancement at the satellite heights as shown in Figure 3.1*a*, which is reproduced as Figure 5.1. In the figure open circles indicate spread echoes at zero range of the ionogram, which means that the satellite is immersed in a severe topside irregularity region (DYSON and BENSON, 1978). On orbit 4416, density enhancement is observed at $\sim 15°$ magnetic latitude accompanied with severe irregularities. A comprehensive data set of density enhancements was also presented by WATANABE and OYA (1986). All the topside plasma enhancements are observed at subtropical latitudes and none can be explained by the traveling of plasma bubbles. Thus it is natural to assume that they are generated at the latitudes where they are observed.

Turning to theoretical works, plasma instability at equatorial latitudes has been widely and extensively studied by many researchers (see review by OSSAKOW (1981)).

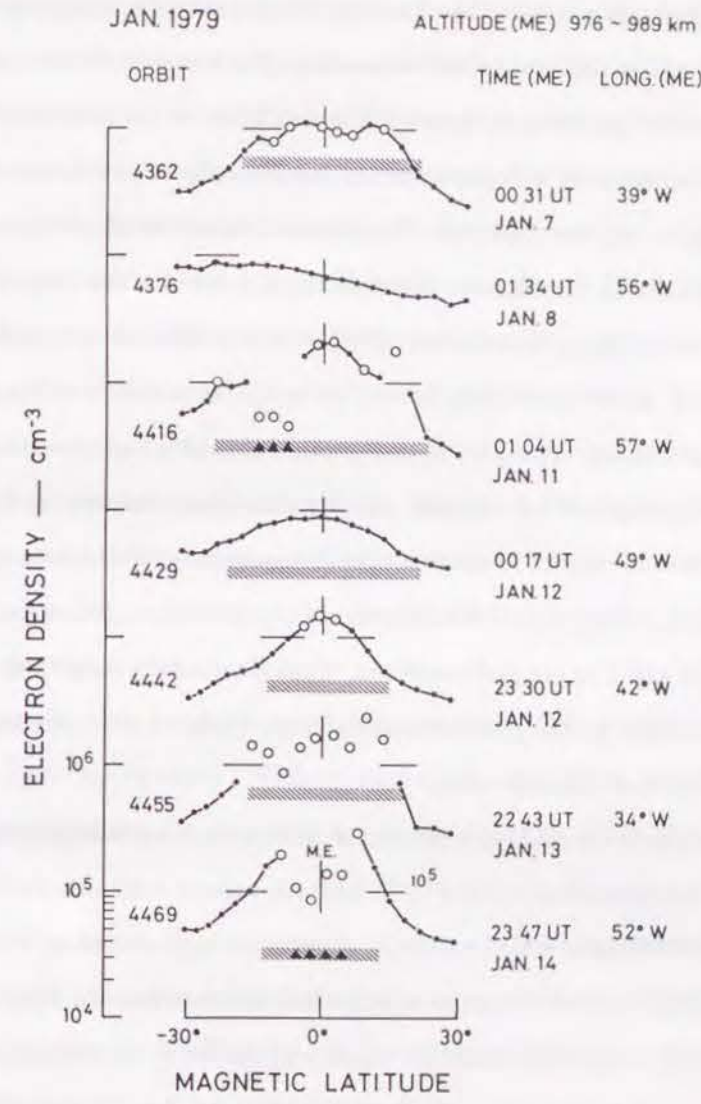

Fig. 5.1. Plasma depletion and enhancement in the topside ionosphere. Electron density at the satellite height ($\sim$ 1000 km) is observed by the topside ionosonde onboard ISS-b. Plasma depletions are seen in orbits 4362, 4416, and 4469, and plasma enhancements in orbit 4416. Both plasma depletions and enhancements are accompanied with intense backscatter echoes from the irregularities surrounding the satellite as indicated by open circles. Shaded bars indicate regions in which spread F is observed.

In a two-dimensional approximation in the equatorial plane, the ionosphere is unstable against the gravitational force (the Rayleigh-Taylor instability) and eastward electric fields (the $\boldsymbol{E}\times\boldsymbol{B}$ instability) in the bottomside. The two-dimensional approximation for the equatorial geometry is based on the fact that the magnetic field lines in the F region are assumed to be equipotentials and ionospheric parameters do not significantly change along the field line. Thus the two-dimensional model is correct only in the bottomside at the equator. Considering the contribution from plasma laying off the equatorial plane, HAERENDEL (1973) showed that the ionosphere is unstable just above the F layer peak as well as in the bottomside in the gravitational Rayleigh-Taylor mode. The growth rate is calculated in terms of vertical gradient of the flux-tube-integrated ion content; the unstable region extends up to the altitude where the total ion content in the flux tube is maximum. This maximum altitude corresponds approximately to the field line that penetrates the equatorial anomaly crests at 10 to 15° N and S in magnetic latitude. Thus Haerendel's result indicates that the ionosphere is stable for the gravitational Rayleigh-Taylor mode at midlatitudes higher than the equatorial anomaly crests.

When ambient electric fields exist, it is inaccurate to consider instability in terms of flux-tube-integrated ion content (S.T. Zalesak, private communication, 1988). This is crucial for field lines which cross the equator at high altitudes, because the ion-neutral collision frequency changes widely along the field line. In Chapter 4, we have derived a linear instability model for equatorial spread F considering plasma in the entire magnetic flux tube when ambient electric fields exist. This model accumulates the contribution of the ion density gradient at each point along the field line instead of dealing with the gradient of the flux-tube-integrated ion content. The model can be extended to a problem in the off-equatorial to midlatitude ionosphere.

This Chapter applies the above model to theoretical investigation of latitudinal extent of ESF, plasmaspheric ducts, subtropical plasma blobs in the topside ionosphere, and midlatitude spread F. However, care must be taken in applying the model

to the midlatitude magnetic field configuration. In deriving the linear growth rate represented by Equation (4.34) or (5.1) we assumed that the redistribution of plasma along the magnetic field line is negligible when the layer is uplifted by the eastward ambient and polarization electric fields. This may be a good approximation for the equatorial bottomside ionosphere, since the magnetic field lines are almost horizontal everywhere. While, in the midlatitudes, prompt downward redistribution of the plasma occurs parallel to the field line when eastward electric fields uplift the layer in the direction perpendicular to the magnetic field line. As a result, the net uplift of the layer is smaller than that deduced from the $\boldsymbol{E}\times\boldsymbol{B}$ drift velocity. Nevertheless, in studying instability, the background ionospheric density distribution can be assumed to be in a quasi-equilibrium state in a frame moving at the $\boldsymbol{E}\times\boldsymbol{B}$ drift velocity if the density perturbation grows to a sufficient amplitude within the time constant of the plasma redistribution. Therefore the time constant of the redistribution becomes essentially important.

The above-mentioned assumption of the quasi-equilibrium condition is quite contrast to that made by PERKINS (1973) on midlatitude instability. Perkins has shown that the nighttime F region supported by eastward electric fields is unstable when a north-south electric field component exists in addition to the supporting eastward field. To derive an instability growth rate, he assumed that the ionosphere is at the equilibrium height, i.e., the redistribution of plasma along the magnetic field line compensates the upward $\boldsymbol{E}\times\boldsymbol{B}$ drifts. In the actual ionosphere, however, there are many nights during which the height changes often.

5.3. Plasma instability

5.3.1. Two-layer model This section first examines a simple two-layer system as an instability model at off-equatorial latitudes.

Geometry of the model is illustrated in Figure 5.2. Layers T and B, both perpendicular to the magnetic field line, represent the topside and bottomside, respectively.

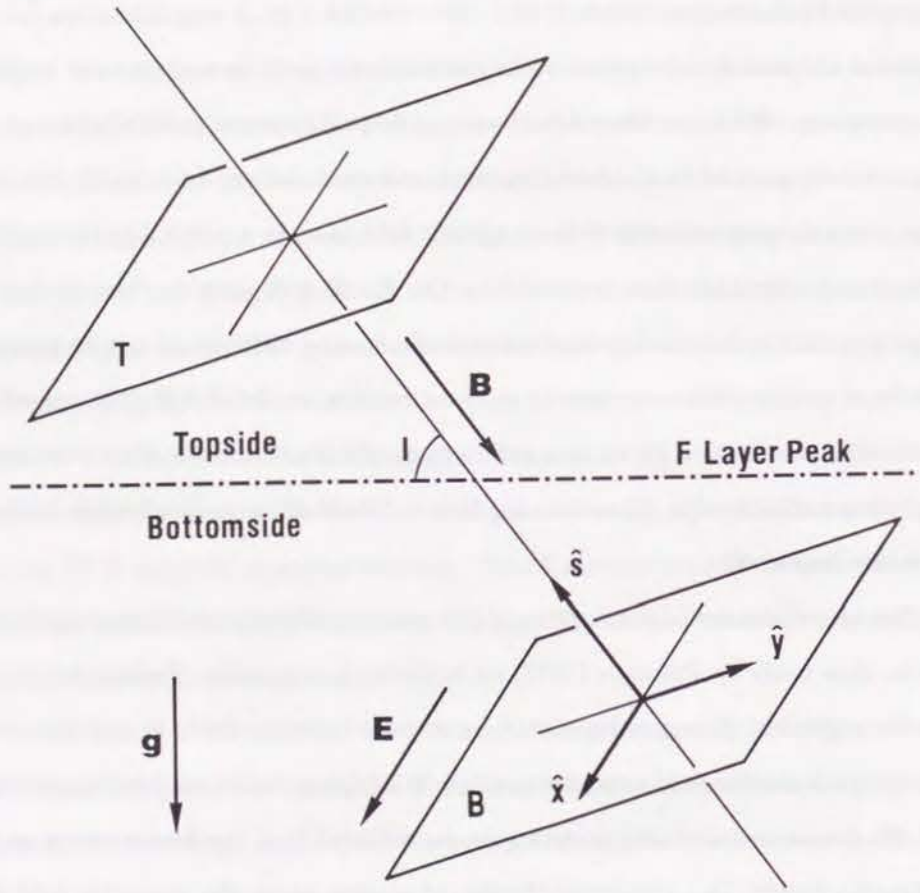

Fig. 5.2. Two-layer system for midlatitude plasma instability. Two layers are electrically connected to each other with highly conductive magnetic field lines.

The two layers are electrically connected by magnetic field lines with high parallel conductivity, but an interflow of plasma between the layers is not allowed. The magnetic field line is assumed to be parallel and I is the magnetic dip angle. Unit vectors are defined as follows: $\hat{x}$ is perpendicular to the magnetic field line and points eastward, $\hat{y}$ is perpendicular to the magnetic field line and points northward, and $\hat{s}$ is antiparallel to the magnetic field vector.

We have already derived the linear growth rate of the instability for the multilayer model represented by (5.1), which is identical to (4.34), in Chapter 4.

$$\gamma = \frac{v_p \sum_i \int \frac{1}{\Delta\kappa_i}\frac{1}{\zeta}\frac{\partial}{\partial p}(\zeta n_{i0})Ads}{r_0 \sum_i \int \frac{n_{i0}}{\Delta\kappa_i}Ads} + \frac{\sum_i \int \frac{g\cos I}{\sin^3\theta\Omega_i}\frac{1}{\zeta}\frac{\partial}{\partial p}(\zeta n_{i0})Ads}{r_0 \sum_i \int \frac{n_{i0}}{\Delta\kappa_i}Ads} \qquad (4.34), (5.1)$$

where the all notations are same as those in Chapter 4. In the two-layer model the parameters, $\Delta, \zeta, \Omega_i, A$, and $\cos I$, in (5.1) are constant, and the integral along the field line is replaced by the summation for the two layers. Thus (5.1) is simplified as follows:

$$\gamma = \frac{v_\perp \sum_l \sum_i \nu_{in,l}\frac{\partial}{\partial y}(n_{i0,l})}{\sum_l \sum_i \nu_{in,l} n_{i0,l}} + \frac{\cos I \sum_l \sum_i g_l \frac{\partial}{\partial y}(n_{i0,l})}{\sum_l \sum_i \nu_{in,l} n_{i0,l}} \qquad (5.2)$$

where the subscript l denotes layers T and B, $v_\perp$ is the local $\boldsymbol{E}\times\boldsymbol{B}$ drift velocity, and we have used the relation,

$$\frac{1}{r_0}\frac{\partial}{\partial p} = \frac{\sin^3\theta}{\Delta}\frac{\partial}{\partial y}$$

$$v_p = \frac{\Delta}{\sin^3\theta}v_\perp$$

To interpret (5.2) a parabolic F layer consisting of O^+ ions is considered. Layer

T is taken at δh above the F layer peak and layer B at δh below the F layer peak, where δh is equal to one scale height of the neutral atmosphere, which is assumed to be 50 km. The following parameters are also assumed:

$$n_{i0,T} = n_{i0,B} = 10^5\,\mathrm{cm}^{-3}$$

$$\frac{1}{n_{i0,B}}\frac{\partial n_{i0,B}}{\partial y} = -\frac{1}{n_{i0,T}}\frac{\partial n_{i0,T}}{\partial y} = \frac{1}{L} = (10\,\mathrm{km})^{-1}$$

$$\nu_{in} = 2.5\,\mathrm{sec}^{-1} \qquad \text{at the } F \text{ layer peak}$$

$$hmF_2 = 350\,\mathrm{km}$$

$$v_\perp = 30\,\mathrm{m/s}$$

$$I = 41^\circ$$

$$g_T = 868\,\mathrm{cm/s}^2$$

$$g_B = 894\,\mathrm{cm/s}^2$$

The above magnetic dip angle corresponds to the field line that crosses the equator at 1600 km above the earth's surface, and the F layer peak at 23.5° magnetic latitude. The $\boldsymbol{E}\times\boldsymbol{B}$ drift velocity corresponds to an electric field of about 1 mV/m. Each term of the right-hand side of (5.2) is evaluated. The $\boldsymbol{E}\times\boldsymbol{B}$ drift term is

$$\frac{v_\perp(-\nu_{in,T}+\nu_{in,B})}{L(\nu_{in,T}+\nu_{in,B})} = \frac{30\times10^2\cdot(-2.5/2.72+2.5\times2.72)}{10\times10^5\cdot(2.5/2.72+2.5\times2.72)} = 2.3\times10^{-3}\,\mathrm{sec}^{-1}$$

The gravitational term is

$$\frac{(-g_T+g_B)\cos I}{L(\nu_{in,T}+\nu_{in,B})} = \frac{(-868+894)\times0.883}{10\times10^5\cdot(2.5/2.72+2.5\times2.72)} = 2.6\times10^{-6}\,\mathrm{sec}^{-1}$$

This instability estimation shows that the $\boldsymbol{E}\times\boldsymbol{B}$ mode still plays an important role in the instability even at off-equatorial latitudes, but that the gravitational mode does not. As expected from the direction of the density gradient, plasma in the topside stabilizes the system both for the gravitational mode and the $\boldsymbol{E}\times\boldsymbol{B}$ mode with eastward electric fields, while plasma in the bottomside destabilizes it. Contributions for the gravitational term from the topside and bottomside are almost the same magnitude, with opposite signs, because the acceleration of gravity changes little with altitude within the F layer thickness. On the other hand, in the $\boldsymbol{E}\times\boldsymbol{B}$ term, the contribution from plasma in the bottomside is much larger than that in the topside because the ion-neutral collision frequency decreases according to the scale height of the neutral density, which is comparable to the F layer thickness.

As shown above, the $\boldsymbol{E}\times\boldsymbol{B}$ instability may operate in the midlatitude ionosphere even though there are conflicting effects from the stable topside and the unstable bottomside ionosphere on the same field line. In the actual ionosphere, however, the net effect on instability is more complicated as the integration path is longer in the topside than that in the bottomside, while density gradient is larger on the bottomside than on the topside. In the following subsections, more careful calculations are made using a continuous model described by (5.1) which employs a realistic magnetic field geometry and ion density distribution along the field line.

5.3.2. Ionospheric modeling The unperturbed state of ion density distribution for the calculations of the integrals in (5.1) is obtained by a modeling approach, which is basically same as that used in Chapter 4 except for the ion species and minor modifications pertinent to the midlatitude ionosphere. The same approach is used to examine the transient response of the background ionosphere to strong eastward electric fields and the quasi-equilibrium condition of the F layer at midlatitudes. The

ion species are assumed to be O^+ and H^+ because a part of the magnetic fields in the midlatitude ionosphere penetrates into the protonosphere and molecular ions are less important. The ion continuity equations in a reference frame moving at $\boldsymbol{E}\times\boldsymbol{B}$ drift velocity $v_{E\times B}$ are (BAILEY, 1983)

$$\frac{dn_i}{dt} = P_i - L_i - \frac{1}{A}\frac{\partial(An_i v_{\parallel i})}{\partial s} - n_i \nabla_\perp \cdot v_{E\times B} \tag{5.3}$$

where the ion production rate P_i includes photoionization and charge exchange with the other species, and the ion loss rate L_i includes charge exchange and recombination. Other notations are the same as those appearing in Chapter 4. The photoionization rates for O^+ and H^+ at the top of the ionosphere are $p_1 = 3.75 \times 10^{-7} s^{-1}$ and $p_2 = 0$, respectively. Sunspot medium conditions are assumed for solar activity. Other chemical reactions pertinent to the above productions and losses are as follows:

$$\begin{aligned}
O^+ + N_2 &\rightarrow NO^+ + N \qquad k_1 = 7.0 \times 10^{-13}\,\mathrm{cm^3\,sec^{-1}} \\
O^+ + O_2 &\rightarrow {O_2}^+ + O \qquad k_2 = 2.0 \times 10^{-11}(300/T)^{0.5}\,\mathrm{cm^3\,sec^{-1}} \\
O^+ + H &\rightarrow O + H^+ \qquad k_3 = 2.5 \times 10^{-11} T^{0.5}\,\mathrm{cm^3\,sec^{-1}} \\
H^+ + O &\rightarrow H + O^+ \qquad k_4 = 2.3 \times 10^{-11} T^{0.5}\,\mathrm{cm^3\,sec^{-1}}
\end{aligned}$$

The recombination rates for NO^+ and ${O_2}^+$ are sufficiently large. Ion and electron temperatures are assumed to be the same as the neutral temperature ($T = T_i = T_e = T_n$). The neutral temperature, T_n, and the density of neutral species, $n(O)$, $n(N_2)$, $n(O_2)$, $n(H)$, and $n(He)$, are calculated from the empirical thermospheric model based on the mass spectrometer and incoherent scatter data (MSIS83) (HEDIN, 1983) with $F_{10.7} = 120$, $A_p = 15$, and day count of 81.

The field-aligned ion velocity $v_{\parallel i}$ containing a diffusion effect is determined from the momentum equation,

$$-g\sin I - \frac{k_B T}{m_i n_i}\frac{\partial n_i}{\partial s} - \frac{k_B T}{m_i n_e}\frac{\partial n_e}{\partial s} - \frac{2k_B}{m_i}\frac{\partial T}{\partial s} - \nu_{in} v_{\parallel i} - \nu_{ij}(v_{\parallel i} - v_{\parallel j}) = 0 \tag{5.4}$$

where k_B is Boltzmann's constant, ν_{in} is the collision frequency between i-th ion and neutral species, and ν_{ij} is the collision frequency between i-th and j-th ion species. The result of STUBBE (1968) is adopted for the ion-neutral collision frequency. To simplify the discussion, no neutral wind is assumed and the magnetic equator is assumed to coincide with the geographical equator.

The equation set (5.3) and (5.4) for O^+ and H^+ is solved by an implicit finite difference method using mathematical techniques described by BAILEY *et al.* (1979) and BAILEY (1983) except that the ion and electron temperatures are assumed to be equal to those of neutral species given by the MSIS model. To calculate the ion density gradient perpendicular to the magnetic field line, the same equation set is solved for magnetic field lines separated by 25km of altitude at the equator. Initial states of the concentration are determined by a combination of the chemical equilibrium at low altitudes and diffusive equilibrium at high altitudes. Integration is started at 0700LT and continued until the required local time of the following day. The integration time may not be sufficient for H^+ ion. However, this matters little because the integrals in (5.1) mainly depend on the O^+ ion dominated region at low altitudes where the density gradient and the ion-neutral collision frequency are relatively large.

Electric field models are given in Figure 5.3 as a form of $\boldsymbol{E}\times\boldsymbol{B}$ drift velocity at the equator. The following assumptions are made for the electric field: Vertical $\boldsymbol{E}\times\boldsymbol{B}$ drift velocity does not depend on altitude; and vertical electric fields or zonal $\boldsymbol{E}\times\boldsymbol{B}$ drifts are zero. These assumptions for the vertical and zonal drift models are not self-consistent (MURPHY and HEELIS, 1986), but which does not matter for the current purpose. The vertical $\boldsymbol{E}\times\boldsymbol{B}$ drift velocity consists of a basic diurnal pattern shown by the solid line and enhancements during evening hours shown by the dashed line (step function) or the dash-dotted line (Gaussian function). The calculation for the first day is made with the solid line. The step-function-like enhancement of the

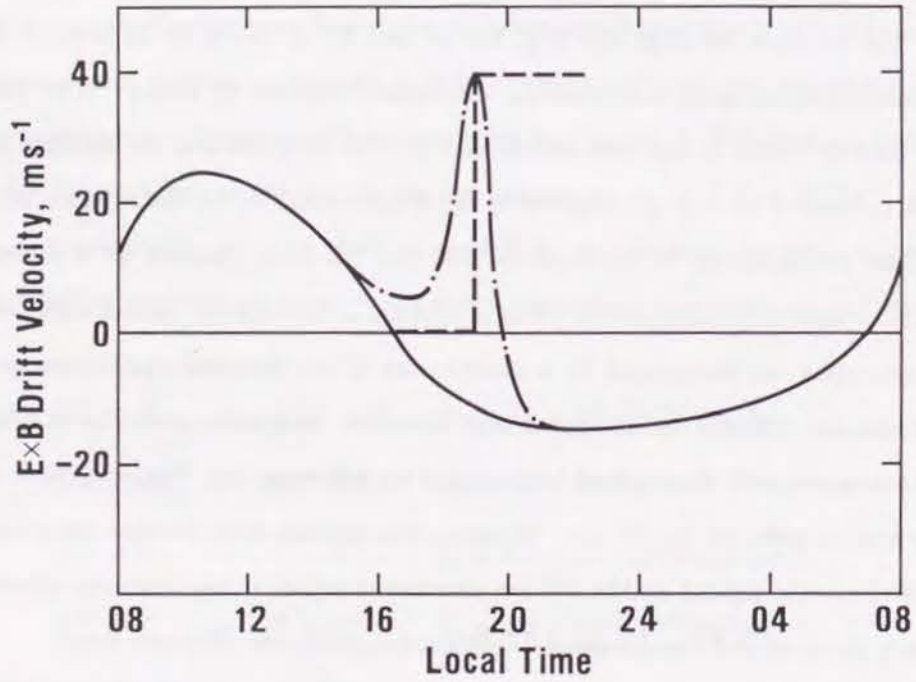

Fig. 5.3. Vertical $\boldsymbol{E}\times\boldsymbol{B}$ drift velocity models with two types of evening drift enhancement. The dashed line indicates step-like enhancement for study of the response of the F layer to intense eastward electric fields. The Gaussian-like (synthesized with two appropriate Gaussian functions) line is for calculation of the instability. Maximum drift velocities are 40 m/sec in both cases.

$\boldsymbol{E}\times\boldsymbol{B}$ drift is used to examine the response of the ionosphere to strong eastward electric fields. The amplitude of the step-like enhancement shown in the figure is 40 m/sec, but examination is made for a variety of the amplitude of enhancement. The Gaussian-type enhancement is more realistic and used to examine the instability.

5.3.3. Quasi-equilibrium condition The basic assumption made in the derivation of the linear growth rate of the instability, a quasi-equilibrium condition in the drifting frame, is not obvious except near the magnetic equator. When zonal electric fields exist at midlatitudes, ionospheric equilibrium is complicated. Tanaka and Hirao (1973) studied effects of an eastward electric field, on electromagnetic dynamics, ion chemistries and induced neutral winds. The response of the layer height to the step-like increase in the eastward electric field strength is as follows. First, the layer height continues to increase due to the $\boldsymbol{E}\times\boldsymbol{B}$ drift. However, the upward drift of the layer ceases and the layer reaches its highest level 30~60min after the change of the electric field strength. Around this time, plasma is appreciably redistributed along the magnetic field. Then the layer begins to descend slowly. By this time a poleward neutral wind is induced by ion-neutral collision. The neutral wind velocity, however, is not sufficient to cancel the height increase due to the $\boldsymbol{E}\times\boldsymbol{B}$ motion.

The above calculation was made with the solar zenith angle of 45° and the dip angle of 60°. Because our interest is in the nighttime subtropical to midlatitude ionosphere, similar calculations assuming nighttime and somewhat low latitude conditions are made. The neutral wind set up by the ion $\boldsymbol{E}\times\boldsymbol{B}$ drift motion is neglected since the time constant is longer than that for the redistribution of the plasma along the magnetic field line.

Field-aligned ion distribution is obtained by solving the continuity equation (5.3) in conjunction with a stepwise increase in the $\boldsymbol{E}\times\boldsymbol{B}$ drift velocity indicated by the dashed line in Figure 5.3. Calculation is made for the field line that crosses the equator at 1600 km, 30 min after the drift increased. The height of the layer peak, hmF_2, is

approximated by a peak in the field-aligned distribution of electron density. At the layer peak when $t = 30$ min, magnetic latitude is 23.5°, dip angle is 41°, and $\boldsymbol{E} \times \boldsymbol{B}$ drift velocity $v_\perp$ is 25.5 m/sec. Time evolution of the layer peak, hmF_2, after the electric field is increased is shown in Figure 5.4. The dashed line indicates the change in hmF_2 deduced from the $\boldsymbol{E} \times \boldsymbol{B}$ drift velocity without any redistribution. From 0 to $\sim$ 15min the layer height increases in response to the $\boldsymbol{E} \times \boldsymbol{B}$ drift velocity, and the assumption of quasi-equilibrium condition in the drifting frame is suitable. After $\sim$ 30min, however, apparent drift of the layer slows. This is due to the increase in downward ion drift along the field line at high altitudes, where the diffusion constant is large.

The characteristic time in which appreciable downward drift is set up is consistent with the observations at Arecibo (BEHNKE *et al.*, 1985); they observed that, during the rise of the F layer, variations in ion velocity parallel to the magnetic field line lag by $\sim$16 min the corresponding variations in ion velocity perpendicular to the field line due to the $\boldsymbol{E} \times \boldsymbol{B}$ motion.

The change in hmF_2 is shown in Figure 5.5 when the amplitude of the step-like increase in the electric field is changed. The figure shows that the layer height responds linearly to the applied electric field until $\sim$ 30 min. This fact is important for amplification of the density perturbations since the polarization electric field arising from the instability process effectively modulates the layer height and the Pedersen conductivity. Within these times the instability process is still effective.

5.3.4. Growth rates of the instability

Instability growth rates as expressed by (5.1) are calculated incorporating the Gaussian-type enhancement of the external electric field indicated by the dash-dotted line in Figure 5.3. The growth rate is maximum at 1900LT according to the peak of the enhanced electric field. The result is shown in Figure 5.6 for 1900LT. In Figure 5.6*a* the $\boldsymbol{E} \times \boldsymbol{B}$ term (the first term on the right-hand side of (5.1)), the gravitational term

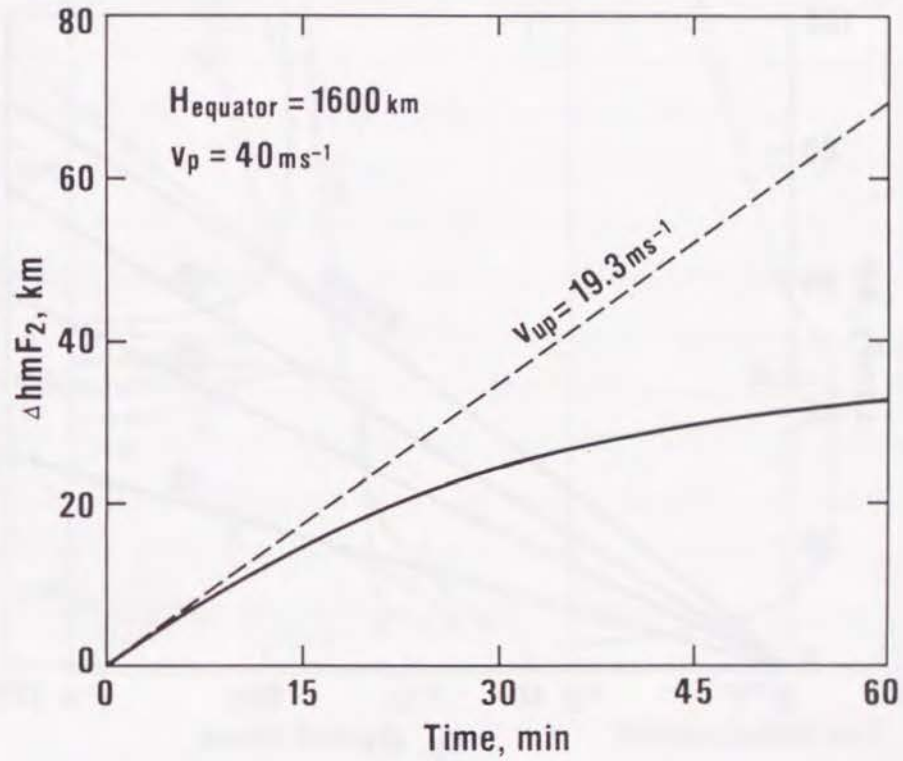

Fig. 5.4. Response of the F layer peak height to the step-like change in the $\boldsymbol{E} \times \boldsymbol{B}$ drift velocity given by the dashed line in Figure 5.3. The equatorial crossing altitude of the field line is 1600 km, 30 min after the change of the electric field. At the F layer peak, magnetic latitude is about 23.5°, dip angle is about 41°, and $v_\perp$=25.5 m/sec.

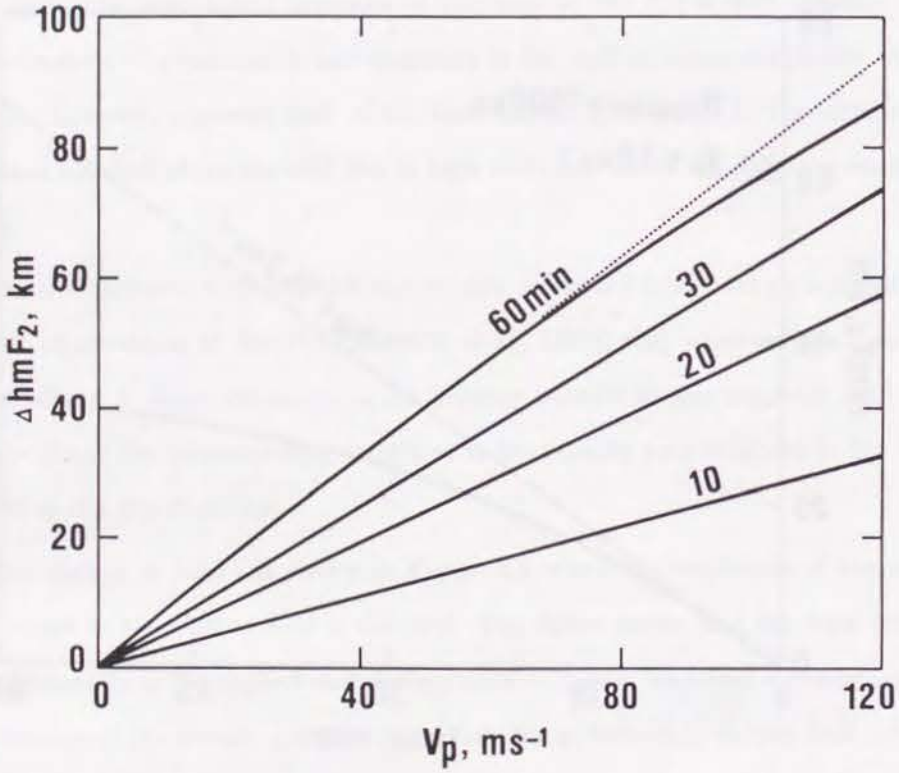

Fig. 5.5. Increases in the F layer peak height 10, 20, 30, and 60 min after the step-like enhancement of $\boldsymbol{E} \times \boldsymbol{B}$ drift velocity when the amplitude of the enhancement varies to 120 m/sec.

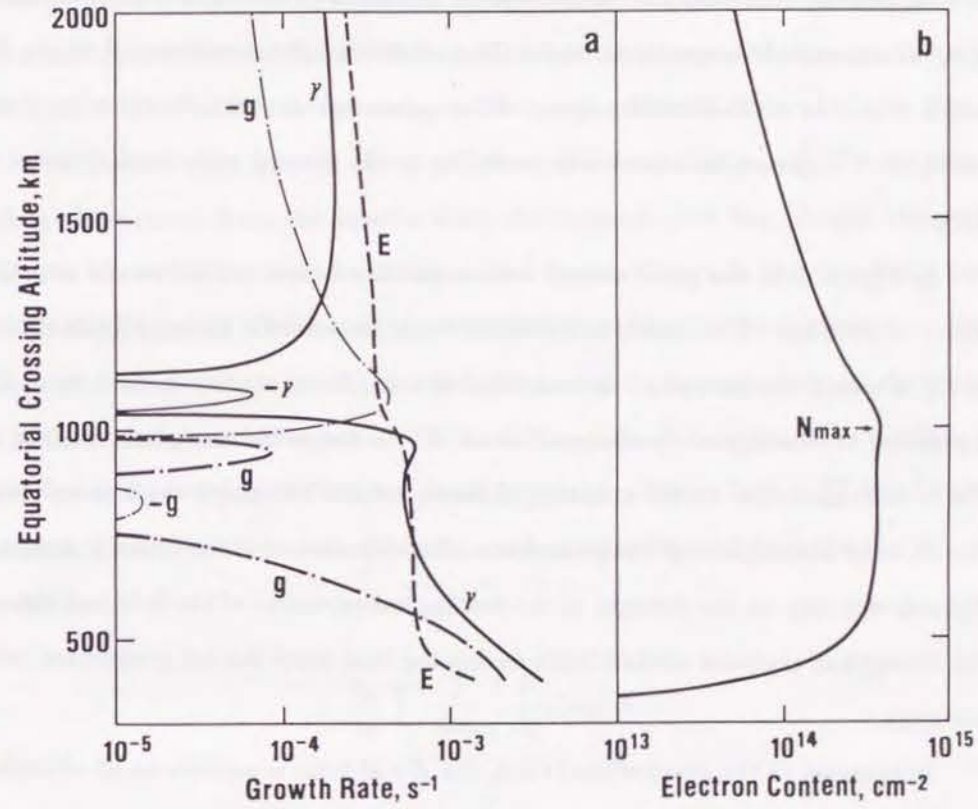

Fig. 5.6. Calculated growth rate (a) and flux tube electron content (b) as a function of equatorial crossing altitude of the field line. Lines in panel (a) are the gravitational term (dash-dotted curve), the $\boldsymbol{E} \times \boldsymbol{B}$ term (dashed curve), and their sum (solid curve). Negative values are indicated by light curves. In panel (b), N_{max} indicates the altitude of the maximum tube electron content which nearly corresponds to the field line penetrates through the crests of equatorial anomaly.

(the second term on the right-hand side of (5.1)), and their sum are plotted. Figure 5.6*b* shows the total electron content, N, in the magnetic flux tube having unit cross sectional area at the equator. At altitudes up to 450 km the magnetic field lines are in the bottomside at every latitude and N increases rapidly with altitudes. A bump in N appearing near 1000 km corresponds to the crests of the equatorial anomaly of f_oF_2 at around 15° magnetic latitude. The altitude of the maximum of N, h_mN, nearly coincides with that of the bump of the equatorial anomaly. At altitudes above 1000 km, N decreases monotonically according to the general latitudinal decrease of f_oF_2.

In Figure 5.6*a* the gravitational term is positive below $\sim$ 750 km and negative above $\sim$ 1000 km. This result is consistent with Haerendel's theory (HAERENDEL, 1973) in which the ionosphere is unstable below h_mN and stable above it since the instability is determined by the gradient of N. A somewhat complex variation at 750 $\sim$ 1000 km is due to the existence of the equatorial anomaly, which complicates the altitude distribution of the parameters. Development of the equatorial anomaly depends not only on the strength of the evening enhancement of the field but also on the strength of eastward electric fields during daytime when the ion production rates are large.

In contrast to the gravitational term, the $\boldsymbol{E}\times\boldsymbol{B}$ term is positive at all altitudes, therefore all latitudes, as shown by the dashed line in the figure. As a result, the total growth rate given by the sum of the two terms is positive except around 1100 km where the gravitational term has a large negative value. The large total growth rate at lower half of the figure, which increases toward the bottomside near the equator, apparently corresponds to equatorial plasma bubbles (OSSAKOW, 1981). The growth rate below 400 km, however, is unrealistic because the current model does not include molecular ions. The positive growth rate at upper half presumably corresponds to midlatitude spread F. The growth rate in the upper part or at midlatitudes is about one tenth of that for plasma bubbles. This accounts for the fact that extremely large

scintillations or intense range-type spread F, which frequently appear at equatorial latitudes, are rare events at midlatitudes (OGAWA and KUMAGAI, 1985; TANAKA, 1986).

Physical meaning of the negative value of the gravitational term at high altitudes, where vertical gradient of tube content is negative, is obvious from Haerendel's theory (HAERENDEL, 1973). For the $\boldsymbol{E}\times\boldsymbol{B}$ term, however, there may need more examination. The variation of each term appearing in the integrands in (5.1) are shown in Figure 5.7 (middle and right panels) along with the ion density (left panel). Shown to the left is the distance from the equator along the magnetic field line. Height above the earth is shown on the right-hand side of the figure. Shown in the figure is a part for an altitude range less than about 1000 km and for the northern hemisphere since the contribution from high altitudes is small enough to be neglected and the model is symmetrical about the equator. The terms are defined using the same notation in (5.1) as follows: Figure 5.7*a* is ion density, $\sum_i n_{i0}A$; Figure 5.7*b* is $\sum_i(n_{i0}/\Delta\kappa_i)A$ which is directly related to the Pedersen conductivity; Figure 5.7*c* is the $\boldsymbol{E}\times\boldsymbol{B}$ term (solid line),

$$\frac{v_p}{r_0}\sum_i \frac{1}{\Delta\kappa_i}\frac{1}{\zeta}\frac{\partial}{\partial p}(\zeta n_{i0})A$$

and the gravitational term (dash-dotted line),

$$\frac{1}{r_0}\sum_i \frac{g\cos I}{\sin^3\theta\Omega_1}\frac{1}{\zeta}\frac{\partial}{\partial p}(\zeta n_{10})A$$

In Figure 5.7 the maximum ion density occurs at 353 km, which is nearly equal to h_mF_2, while the maximum n/κ is lower than h_mF_2 by $\sim$70 km. This is due to that the ion-neutral collision frequency decreases with altitudes. In Figure 5.7*c* both the gravitational and $\boldsymbol{E}\times\boldsymbol{B}$ terms are negative at altitudes above h_mF_2 and positive below h_mF_2 according to the ion density gradient perpendicular to the magnetic

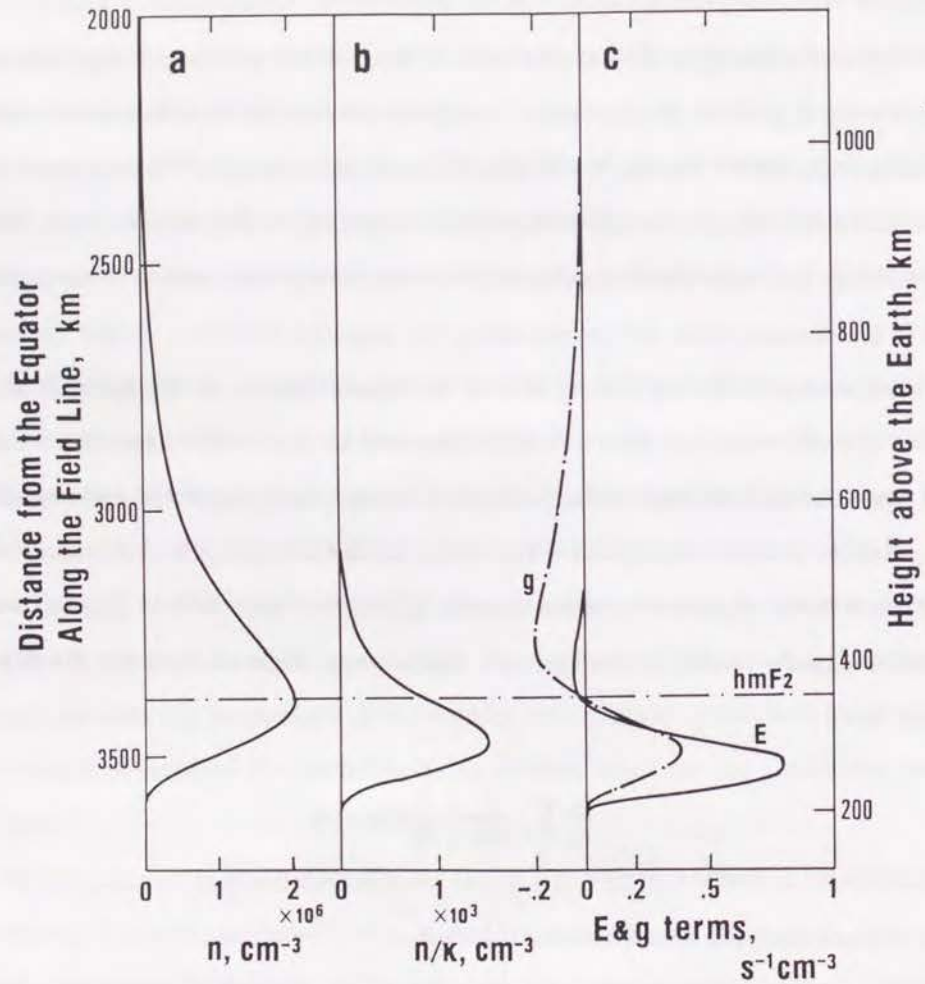

Fig. 5.7. Altitude variation of the integrands appearing in the expression of growth rate (see text) as a function of distance from the equator along the magnetic field line. Equatorial crossing altitude of the field line is 1600 km.

field line. Two terms, however, differs quantitatively; for the gravitational term the negative area looks larger than the positive area. (We should note that the figure is in linear scale on both horizontal and vertical axes and the cross sectional area of the flux tube is already included in each term.) Such a quantitative result cannot be expected from the simple two-layer model discussed previously. On the other hand, the negative value of the $\boldsymbol{E} \times \boldsymbol{B}$ term on the topside is so small that the contribution is almost negligible. The net positive growth rates at midlatitudes can be concluded to originate from the large $\boldsymbol{E} \times \boldsymbol{B}$ term below the F layer peak.

5.4. Comparison with observations

5.4.1. Plasma blobs The calculations are compared with observations. We first discuss a possible generation mechanism of plasma blobs presented in Figure 5.1. From the viewpoint of plasma dynamics, irregularities are produced by convection of the magnetic flux tube. When the midlatitude ionosphere is unstable by the mechanism as described in this chapter, plasma depleted region in the bottomside drifts northward and upward with respect to the ambient ionosphere by the polarization electric field. The local electron density gradient in the topside is reverse to the drift direction. Thus density enhancement appears in the topside, as a counterpart, which is connected with the magnetic field line passing through the bottomside depletion. The linear instability theory just predicts undulation of density irregularities, and the isolated plasma blobs as observed are presumably generated by nonlinear process similarly to the case of equatorial plasma bubbles.

For comparison between the theoretical results and observations, unfortunately, the number of plasma blobs detected by ISS-b is too small; well-defined events are less than 10. However, we are able to discuss statistical results in the published material. The Hinotori satellite observed fairly large number of plasma blobs (Oya *et al.*, 1986; Watanabe and Oya, 1986). According to this, the blobs are observed mostly in the narrow latitude region from 15°to 30° in both hemispheres (Figure 3 of Watanabe

and OYA (1986)), though the properties at latitudes higher than $\sim 30°$ were not observed because the orbital inclination angle of the satellite to the equatorial plane is 31°. These latitudes correspond to the rims of the area of equatorial spread F as shown in Figures 2.5 through 2.8. The plasma blob shown in Figure 5.1 is associated with severe backscatter echoes from the irregularities surrounding the space craft. Apparently a fraction of the equatorial spread F discussed in Chapter 2 is related with the plasma blobs.

Plasma blobs are often observed in the winter topside ionosphere at subtropical latitudes (WATANABE and OYA, 1986). This may be accounted for as follows: The amount of the density enhancement of plasma blobs in the topside ionosphere depends on the local density gradient antiparallel to the direction of $\boldsymbol{E}\times\boldsymbol{B}$ drift due to eastward electric fields. Generally a large equatorward gradient of the electron density is attained in the winter hemisphere by seasonal winds blowing from the summer hemisphere to the winter one (e.g., Figure 5.4 of ANDERSON and ROBLE (1981)). Such density gradient is observed by ISS-b as presented in Figures 3.4 through 3.6. Furthermore the largest gradient appears at the longitudes of large eastward magnetic declination during northern summer season and westward declination during northern winter season. As we have discussed in detail in Chapters 3 and 4, gravitational Rayleigh-Taylor instability is greatly suppressed at these longitudes. This longitudinal variability of equatorward gradient is also consistent with the longitudinal distribution of the plasma blob as observed by Hinotori.

Although blobs are detected only in one hemisphere (WATANABE and OYA, 1986), if the convection of the magnetic field line creates the irregularities, small field-aligned enhancements are anticipated in the other hemisphere. These irregularities may be hard to detect with plasma probes, but cause conjugate ducted echoes (MULDREW, 1980*a*) as discussed next.

5.4.2. Conjugate ducted echoes Field-aligned structure is one of the peculiar features of irregularities observed by satellite-borne topside ionosondes (MULDREW, 1963). Conjugate ducted echoes are sometimes observed on ionograms at low- to mid-latitudes, which are caused by field-aligned irregularities extending from one hemisphere to the other. The topside sounding is a sensitive technique for detecting such irregularities because a duct with a density discontinuity of a few percent in the direction perpendicular to the magnetic field line can trap transmitted waves in it (MULDREW, 1963). Therefore observations of conjugate ducted echoes are pertinent to comparison with the instability calculations because irregularities with large amplitude, like a plasma bubble, are not expected other than at the equatorial latitudes.

MULDREW (1980*a*) examined a large number of Alouette 2 topside ionograms and obtained some morphology on the occurrence of conjugate ducts. There is a minimum in duct occurrence near $L = 1.2$ with respect to radial variation in his L-value versus local-time diagram. On the basis of the morphology, he concluded that the conjugate ducts with $L \lesssim 1.2$ could be associated with equatorial plasma bubbles, while those with $L \gtrsim 1.2$ do not result from rising plasma bubbles. The altitude variation of the calculated growth rate shown in Figure 5.6 exhibits a negative or stable region near 1100 km, which corresponds to $L \sim 1.17$. Apparently the large growth rate at altitudes below 1000 km accounts for generation of plasma bubbles. At altitudes greater than 1100 km the growth rate of the instability is smaller than that in the low altitude region by one order. In the analogy to plasma bubbles (OSSAKOW *et al.*, 1979), it needs some 10 growth times to generate disturbance like a rising plasma bubble. Thus large disturbance may not occur at midlatitudes except when unusually large electric field events. However, small field-aligned density discontinuity could be easily generated through electromagnetic convection and downward (equatorward) density gradient in the topside ionosphere. Irregularities generated in such a way have an intrinsically field-aligned nature. They remain where they are generated and do not travel far like rising bubbles. Thus present calculation results agree with the L-value

distribution of conjugate ducts observed by the topside ionosonde.

Another interesting feature of the conjugate ducts pointed out by MULDREW (1980*a*) is local time variation. The occurrence of ducts for $L \gtrsim 1.2$ tends to increase near 20 to 22 hours, while that for $L \lesssim 1.2$ increases from 20 to 02 hours. As seen in Figure 5.6, for $L \gtrsim 1.17$, the gravitational term acts as a stabilizing factor and the $\boldsymbol{E} \times \boldsymbol{B}$ term as a destabilizing factor when the electric fields are eastward. Thus for $L \gtrsim 1.17$, generation of irregularities ceases when the electric field reverses from eastward to westward. On the other hand for $L \lesssim 1.17$, the gravitational term acts as a destabilizing factor irrespective of direction of the electric field. The net growth rate at these altitudes may be positive even after the reversal of the electric fields until the layer is moved to lower altitudes where the ion-neutral collision frequency is high. If the behavior of electric fields does not change with altitude or latitude, the present theory also agrees with the local time variation of the ducts observed.

5.4.3. MU radar observations Recently, field aligned irregularities have been observed by the radar at Shigaraki, Japan (FUKAO *et al.*, 1988, 1991). This radar, the MU radar, operates at 46.5MHz and is steerable up to a zenith angle of 56° at which the radar beam is perpendicular to the magnetic field line. Intense echoes from field-aligned irregularities are recorded as a range-time-intensity map. There are a variety of cases of apparent drift direction that is deduced from the gross feature of echo region, i.e., northward, southward, and stationary. However, fine structures always incline as they drift northward when an intense echo region first appears (FUKAO *et al.*, 1991). Doppler shifts corresponding to a radial drift velocity of ~100 m/s are also observed in some events (FUKAO *et al.*, 1988, 1991). These observations indicate that the field-aligned irregularities are associated with eastward electric field events, which is consistent with the $\boldsymbol{E} \times \boldsymbol{B}$ instability presented here. More direct comparisons between $\boldsymbol{E} \times \boldsymbol{B}$ drift velocity and midlatitude field-aligned irregularities are expected from the MU radar facility at Shigaraki.

5.4.4. Origin of the electric field enhancements The electric field model illustrated in Figure 5.3 requires some comments. There are two origins of enhancements in the eastward electric field at night. One is due to action of the F layer dynamo, and the other reflects penetration of the magnetospheric fields.

A model calculation based on the dynamo theory predicts enhancement of eastward electric fields near the equator in the evening hours (HEELIS *et al.*, 1974). The amplitude of this electric field enhancement is somewhat larger than observations by the incoherent scatter (IS) radar at Jicamarca (FEJER *et al.*, 1979). Height variation of the equatorial electric fields, which is equivalent to latitudinal variation at the F layer peak, is studied both experimentally (PINGREE and FEJER, 1987) and theoretically (MURPHY and HEELIS, 1986). Both studies predict that the enhancement of electric fields in the evening hours becomes weaker at higher latitudes. Data used for these studies are limited to sunspot minimum conditions. However, equatorial electric fields indicate a large day-to-day variation and change with solar activity, season (FEJER *et al.*, 1979), and longitude (BATISTA *et al.*, 1986). At any rate it is not clear that the F layer dynamo effect causes the midlatitude irregularities on the basis of information currently available.

Direct evidence of the penetration of magnetospheric origin electric fields is possible by using data from the IS radar chain in the American sector (GONZALES *et al.*, 1983; EARLE and KELLEY, 1987). At the midlatitude station, Arecibo, the largest electric field amplitude reported corresponds to a northward $\boldsymbol{E} \times \boldsymbol{B}$ drift velocity of $v_{\perp N} \gtrsim 100$ m/s (GONZALES *et al.*, 1983; BEHNKE *et al.*, 1985). If the magnetic fields are assumed to be in a dipole geometry the northward $\boldsymbol{E} \times \boldsymbol{B}$ drift velocity in the midlatitude ionosphere, $v_{\perp N}$, is related to the equatorial upward drift velocity, v_p, in the same magnetic meridional plane using the colatitude, θ, of the point concerned as follows:

$$v_{\perp N} = \frac{\sin^3\theta}{(1+3\cos^2\theta)^{1/2}} v_p$$

Thus the $\boldsymbol{E}\times\boldsymbol{B}$ drift velocity in the magnetic meridional plane over Arecibo ($\theta \sim 60°$) is about half the corresponding equatorial upward drift velocity. The above observed amplitude of electric field is about five times the enhanced electric field given in Figure 5.3. Unfortunately, it is not clear how often such a large disturbance in electric fields occurs.

At night, $h'F$ scaled from the ionogram is a good indicator of short term change in the electric field, and we have a much larger data base than the IS radars. Anomalous variations of $h'F$ and corresponding f_oF_2 in the evening hours associated with magnetospheric disturbances are presented by using data from the lower-midlatitude ionosonde station chain in Japan's sector (TANAKA, 1986). Variations appear as an enhancement of the eastward electric field. These ionospheric disturbances are interpreted as a penetration of magnetospheric electric fields into low latitudes. During one of these events midlatitude irregularities indicating a field-aligned duct were observed by the topside ionosonde onboard ISIS 2 after the eastward electric field enhancement (TANAKA, 1987).

5.5. Concluding remarks

The non-local theory of equatorial spread F developed in Chapter 4 is applied to the off-equatorial and midlatitude ionospheric instability. The gravitational Rayleigh-Taylor mode is stable at latitudes higher than the crests of the equatorial anomaly, while the $\boldsymbol{E}\times\boldsymbol{B}$ mode is unstable at all latitudes when the electric fields are eastward. Net instability growth rate is negative in the narrow region around the magnetic field line that crosses the equator at 1100 km and penetrates the F layer peak near 18° in magnetic latitude. In lower and higher latitude regions of the crests, the ionosphere becomes unstable. In the lower latitude region the instability accounts for generation

of plasma bubbles, while in the higher latitude region it accounts for generation of conjugate plasma ducts, plasma blobs in the topside ionosphere, and midlatitude bottomside spread F.

At the latitudes near the rims of the equatorial spread F region, which are ~20° in magnetic latitude, presumably both effects coexist; nonlinear traveling of the plasma bubble from the equator and $\boldsymbol{E}\times\boldsymbol{B}$ drift instability developing at those latitudes.

The growth rate at midlatitudes, which is a function of the eastward electric field, is generally smaller than that for equatorial plasma bubbles by one order. The small growth rate is consistent with the latitudinal distribution of spread F shown in Figures 2.5 through 2.8 and the fact that severe scintillations are rare events at midlatitudes. However, in an unusually large eastward electric field event, intense irregularities and gigahertz scintillations can occur, even at off-equatorial and midlatitudes.

6.1. Experimental results

The topside ionospheric sounding by the ISS-b satellite first allowed to investigate complete worldwide morphology of equatorial spread F (ESF), which yielded fairly clear picture of a coupled seasonal-longitudinal effect of ESF: during northern winter season the ESF activity is high at the Atlantic longitudes where the geomagnetic fields have large westward declination; during northern summer season the longitudinal peak of ESF activity moves to the Pacific longitudes where the geomagnetic fields have large eastward declination; and during the equinoxes the ESF activity is high at the Indian longitudes where the magnetic declination angle is small.

Also revealed from the ionograms are the abrupt plasma depletions associated with severe back scatter echoes at zero range, which are ascribed to the encounter with a plasma bubble. The plasma bubbles are the results of nonlinear evolution of the Rayleigh-Taylor instability, which is considered to be a primary mechanism to generate equatorial spread F. The positions of the plasma bubble encounter coincide with the areas of high ESF activity. Another category of plasma irregularities at the satellite height is the localized plasma enhancement or blob. The generation of plasma blobs can not be explained by any previous theories. The generation of the plasma blobs is discussed with theoretical and numerical calculations as described later.

The background ionospheric configuration is examined by the same ionosonde data, which may be connected with the cause of the seasonal-longitudinal effect of ESF. It is found that the electron density distribution in the magnetic meridional plane is symmetric with respect to the magnetic equator when and where the ESF activity enhancement is seen, while it is asymmetric when and where the ESF activity is low. This morphological connection between the large scale structure and ESF suggests that a transequatorial component of thermospheric winds in the magnetic meridional plane plays a role in suppression of the growth of the gravitational

Rayleigh-Taylor instability and the ESF activity. A plausible mechanism of the instability suppression is the increase of Pedersen conductivity integrated along the magnetic field line that is due to the lowering of the ionospheric height in the lee side hemisphere. Therefore absence of a transequatorial thermospheric wind is one of the important necessary conditions for the growth of equatorial spread F. Such condition tends to be satisfied at the Atlantic longitudes during the northern winter, at the Pacific longitudes during the northern summer, and at the Indian longitudes during the equinoxes, where the directions of the thermospheric diurnal winds in the nighttime F region tend to be perpendicular to the magnetic meridians following the seasonal migration of the thermospheric pressure bulge.

6.2. Computational results

The mechanism proposed to take account for the seasonal-longitudinal effect of ESF is further investigated. For this purpose, we have developed a diagnostic model and applied it to the ionosphere using parameters determined by solving a continuity equation under variable conditions including ambient electric fields and transequatorial thermospheric winds. The instability model contains effects from F region plasma away from the equatorial plane and the $\boldsymbol{E}\times\boldsymbol{B}$ drift effect.

Numerical calculations are made with realistic electric field model based on the observations at Jicamarca and Fortaleza and thermospheric wind based theoretical calculations. The results have shown that the transequatorial wind and the $\boldsymbol{E}\times\boldsymbol{B}$ drift are equally important for controlling the generation of ESF. A large wind velocity significantly reduces the instability growth rate, even if a large upward $\boldsymbol{E}\times\boldsymbol{B}$ drift velocity is applied. Some properties of ESF at Jicamarca and other stations close to it can be explained in terms of the seasonal change in $\boldsymbol{E}\times\boldsymbol{B}$ drift velocity irrespective of the wind effect. A morphology over all seasons, however, indicates much better agreement with the calculations including the wind effect. On the other hand, without taking account of the wind effect, the seasonal dependence of the occurrence of

equatorial spread F at Fortaleza cannot be explained by the $\boldsymbol{E}\times\boldsymbol{B}$ drift effect only. An instability model incorporating both $\boldsymbol{E}\times\boldsymbol{B}$ drift and wind effects can explain the observed seasonal trend.

The above results can be extended at all longitudes. Since the transequatorial component of the thermospheric wind in the magnetic meridional plane is determined by the magnetic declination angle at every longitude, the magnetic declination effect of ESF or a seasonal-longitudinal effect of ESF may be well explained by the wind effect investigated here. However, a possible longitudinal change in the $\boldsymbol{E}\times\boldsymbol{B}$ drift pattern could be equally important and is not known at this time.

The non-local theory of linear plasma instability developed for the equatorial latitudes is applied to the off-equatorial and midlatitude ionospheric instability. The gravitational Rayleigh-Taylor mode is stable at midlatitudes higher than the crests of the equatorial anomaly, while the $\boldsymbol{E}\times\boldsymbol{B}$ mode is unstable at all latitudes when the electric fields are eastward. As a result, the net instability growth rate is negative in the narrow region around the magnetic field line that crosses the equator at 1100km and penetrates the F layer peak near 18° in magnetic latitude. In lower and higher latitude regions the ionosphere becomes unstable; in the lower latitude region the instability accounts for generation of plasma bubbles; while in the higher latitude region it accounts for generation of plasma ducts, plasma blobs observed in the topside ionosphere, and midlatitude bottomside spread F.

At the latitudes near the rims of the equatorial spread F region, which are ~20° in magnetic latitude, presumably the following two effects coexist: nonlinear evolution of the plasma bubble from the equator and $\boldsymbol{E}\times\boldsymbol{B}$ drift instability growth at those latitudes.

The growth rate at midlatitudes, which is a function of the eastward electric field, is generally one order of magnitude smaller than that for equatorial plasma bubbles. This small growth rate is consistent with the latitudinal distribution of spread F shown in Figures 2.5 through 2.8 and the fact that severe scintillations are

rare events at midlatitudes. However, in a quite large eastward electric field event, intense irregularities and gigahertz scintillations can occur, even at off-equatorial and midlatitudes.

References

Abdu, M. A., J. A. Bittencourt, and I. S. Batista, Magnetic declination control of the equatorial F region dynamo electric field development and spread F, *J. Geophys. Res., 86*, 11,443-11,446, 1981.

Anderson, D.N. and G. Haerendel, The motion of depleted plasma regions in the equatorial ionosphere, *J. Geophys. Res., 84*, 4251-4256, 1979.

Anderson, D.N. and M. Mendillo, Ionospheric conditions affecting the evolution of equatorial plasma depletions, *Geophys. Res. Lett., 10*, 541-544, 1983.

Anderson, D.N., and R.G. Roble, Neutral wind effects on the equatorial F-region ionosphere, *J. Atmos. Terr. Phys., 43*, 835-843, 1981.

Anderson, D.N. and D.W. Rusch, Composition of the nighttime ionospheric F_1 region near the magnetic equator, *J. Geophys. Res., 85*, 569-574, 1980.

Anderson, D.N., A.D. Richmond, B.B. Balsley, R.G. Roble, M.A. Biondi and D.P. Sipler, In-situ generated gravity waves as a possible seeding mechanism for equatorial spread-F, *Geophys. Res. lett., 9*, 789-792, 1982.

Anderson, D. N., M. Mendillo, and B. Herniter, A semi-empirical low-latitude ionospheric model, *Radio Sci., 22*, 292-306, 1987.

Bailey, G.J., The effect of meridional $\boldsymbol{E}\times\boldsymbol{B}$ drift on the thermal plasma at L=1.4, *Plant. Space Sci., 31*, 389-409, 1983.

Bailey, G.J., R.J. Moffett, and J.A. Murphy, Calculated daily variations of O^+ and H^+ at mid-latitudes - II. Sunspot maximum results, *J. Atmos. Terr. Phys., 41*, 417-429, 1979.

Balsley, B.B., G. Haerendel, and R.A. Greenwald, Equatorial spread F: Recent observations and a new interpretation, *J. Geophys. Res., 77*, 5625-5628, 1972

Basu, S., and S. Basu, Equatorial scintillations: Advances since ISEA-6, *J. Atmos.*

Terr. Phys., 47, 753-768, 1985.

Basu, S., and M.C. Kelley, A review of recent observations of equatorial scintillations and their relationship to current theories of *F* region irregularity generation, *Radio Sci., 14*, 471-485, 1979

Basu, S., S. Basu and B.K. Khan, Model of equatorial scintillations from in-situ measurements, *Radio Sci., 11*, 821-832, 1976.

Basu, S., S. Basu, S. Ganguly, and J.A. Klobuchar, Generation of kilometer scale irregularities during the midnight collapse at Arecibo, *J. Geophys. Res., 86*, 7607-7616, 1981.

Batista, I.S., M.A. Abdu, and J.A. Bittencourt, Equatorial *F* region vertical plasma drifts: Seasonal and longitudinal asymmetries in the American sector, *J. Geophys. Res., 91*, 12,055-12,064, 1986.

Behnke, R., M. Kelley, C. Gonzales, and M. Larsen, Dynamics of the Arecibo ionosphere: A case study approach, *J. Geophys. Res., 90*, 4448-4452, 1985.

Benson, R.F., Stimulated plasma waves in the ionosphere, *Radio Sci., 12*, 861-878, 1977.

Benson, R.F., Stimulated plasma instability and nonlinear phenomena in the ionosphere, *Radio Sci., 17*, 1637-1659, 1982.

Bittencourt, J.A., and Y. Sahai, *F*-region neutral winds from ionosonde measurements of $hmF2$ at low latitude magnetic conjugate regions, *J. Atmos. Terr. Phys., 40*, 669-676, 1978.

Bittencourt, J. A., B. A. Tinsley, G. T. Hicks, and E. I. Reed, Tropical *F* region winds from OI 1356-Å and [OI] 6300-Å emissions 2. Analysis of Ogo 4 data, *J. Geophys. Res., 81*, 3786-3790, 1976.

Burke, W.J., D.E. Donatelli, R.C. Sagalyn and M.C. Kelley, Low density regions

observed at high altitudes and their connection with equatorial spread *F*, *Planet. Space Sci., 27*, 593-601, 1979.

Burke, W.J., D.E. Donatelli and R.C. Sagalyn, The longitudinal distribution of equatorial spread *F* plasma bubbles in the topside ionosphere, *J. Geophys. Res., 85*, 1335-1340, 1980.

Calvert, W. and C.W. Schmid, Spread-*F* observations by the Alouette topside sounder satellite, *J. Geophys. Res., 69*, 1839-1852, 1964.

Chiu, Y.T., An improved phenomenological model of ionospheric density, *J. Atmos. Terr. Phys., 37*, 1563-1570, 1975.

Chiu, Y.T. and J.M. Straus, Rayleigh-Taylor and wind-driven instabilities of the nighttime equatorial ionosphere, *J. Geophys. Res., 84*, 3283-3290, 1979.

DasGupta, A., J. Aarons, J. A. Klobuchar, S. Basu, A. Bushby, Ionospheric electron content depletions associated with amplitude scintillations in the equatorial region, *Geophys. Res. Lett., 9*, 147-150, 1982.

Dickinson, R. E., E. C. Ridley, and R. G. Roble, A three-dimensional general circulation model of the thermosphere, *J. Geophys. Res., 86*, 1499-1512, 1981.

Dyson, P.L. and R.F. Benson, Topside sounder observations of equatorial bubbles, *Geophys. Res. Lett., 5*, 795-798, 1978.

Earle, G.D., and M.C. Kelley, Spectral studies of the sources of ionospheric electric fields, *J. Geophys. Res., 92*, 213-224, 1987.

Farley, D.T., B.B. Balsley, R.F. Woodman, and J.P. McClure, Vertical drift velocities and east-west electric field at the magnetic equator, *J. Geophys. Res., 75*, 7199-7216, 1970.

Fejer, B.G., and M.C. Kelley, Ionospheric irregularities, *Rev. Geophys. Space Phys., 18*, 401-454, 1980.

Fejer, B.G., D.T. Farley, R.F. Woodman, and C. Calderon, Dependence of equatorial *F* region vertical drifts on season and solar cycle, *J. Geophys. Res., 84*, 5792-5796, 1979.

Franklin, C.A., R.J. Bibby, and N.S. Hitchcock, A data acquisition and processing system for mass producing topside ionograms, *Proc. IEEE, 57*, 929-944, 1969.

Fukao, S., J.P. McClure, A. Ito, T. Sato, I. Kimura, T. Tsuda, and S. Kato, First VHF radar observation of midlatitude *F*-region field-aligned irregularities, *Geophys. Res. Lett., 15*, 768-771, 1988.

Fukao, S., M.C. Kelley, T. Shirakawa, T. Takami, M. Yamamoto, T. Tsuda, and S. Kato, Turbulent upwelling of the mid-latitude ionosphere 1. Observational results by the MU radar, *J. Geophys. Res., 96*, 3725-3746, 1991.

Ganguly, S., R.A. Behnke, and B.A. Emery, Average electric field behavior in the ionosphere above Arecibo, *J. Geophys. Res., 92*, 1199-1210, 1987.

Gonzales, C.A., M.C. Kelley, R.A. Behnke, J.F. Vickrey, R. Wand, and J. Holt, On the latitudinal variations of the ionospheric electric field during magnetospheric disturbances, *J. Geophys. Res., 88*, 9135-9144, 1983.

Gross, S.H., and D.B. Muldrew, Uniformly spaced field-aligned ionization ducts, *J. Geophys. Res., 89*, 8986-8996, 1984.

Guzdar, P.N., P. Satyanarayana, J.D. Huba and S.L. Ossakow, Influence of velocity shear on the Rayleigh-Taylor instability, *Geophys. Res. Lett., 9*, 547-550, 1982.

Haerendel, G., Theory of equatorial spread *F*, *report, Max-Planck Inst. für Phys. Astrophys.*, Federal Republic of Germany, 1973.

Hanson, W.B. and S. Sanatani, Relationship between Fe^+ ions and equatorial spread *F*, *J. Geophys. Res., 76*, 7761-7768, 1971.

Hanson, W.B., J.P. McClure and D.L. Sterling, On the cause of equatorial spread *F*, *J. Geophys. Res., 78*, 2353-2356, 1973.

Hanson, W.B., S. Sanatani and T.N.L. Patterson, Influence of the *E* region dynamo on equatorial spread *F*, *J. Geophys. Res., 88*, 3169-3173, 1983.

Hanson, W.B., B.L. Cragin, and A. Dennis, The effect of vertical drift on the equatorial *F*-region stability, *J. Atmos. Terr. Phys., 48*, 205-212, 1986.

Hartz, T.R., Radio noise levels within and above the ionosphere, *Proc. IEEE, 57*, 1042-1050, 1969.

Hartz, T.R. and R.S. Roger, The effective antenna beam width for a satellite-borne radio telescope, *Can. J. Phys., 42*, 2146-2152, 1964.

Hedin, A. E., A revised thermospheric model based on mass spectrometer and incoherent scatter data: MSIS-83, *J. Geophys. Res., 88*, 10,170-10,188, 1983.

Hedin, A.E., J.E. Salah, J.V. Evans, C.A. Reber, G.P. Newton, N.W. Spencer, D.C. Kayser, D. Alcayde, P. Bauer, L. Cogger and J.P. McClure, A global thermospheric model based on mass spectrometer and incoherent scatter data MSIS 1. N_2 density and temperature, *J. Geophys. Res., 82*, 2139-2147, 1977a.

Hedin, A.E., C.A. Reber, G.P. Newton, N.W. Spencer, H.C. Brinton, H.G. Mayr and W.E. Potter, A global thermospheric model based on mass spectrometer and incoherent scatter data MSIS 2. Composition, *J. Geophys. Res., 82*, 2148-2156, 1977b.

Heelis, R.A., P.C. Kendall, R.J. Moffett, D.W. Windle, and H. Rishbeth, Electrical coupling of the *E*- and *F*-regions and its effect on *F*-region drifts and winds, *Planet. Space Sci., 22*, 743-756, 1974.

Herman, J.R., Spread *F* and ionospheric *F*-region irregularities, *Rev. Geophys., 4*, 255-299, 1966.

Kelley, M.C. and T. Maruyama, A diagnostic model for equatorial spread *F* : 2. The

effect of magnetic activity, *J. Geophys. Res. 97*, 1271-1277, 1992.

Kelley, M.C. and J.P. McClure, Equatorial spread-F: A review of recent experimental results, *J. Atmos. Terr. Phys., 43*, 427-435, 1981.

Kelley, M.C., K.D. Baker, and J.C. Ulwick, Late time barium cloud striation and their possible relationship to equatorial spread F, *J. Geophys. Res., 84*, 1898-1904, 1979.

Kelley, M.C., M.F. Larsen, C. LaHoz and J.P. McClure, Gravity wave initiation of equatorial spread F: A case study, *J. Geophys. Res., 86*, 9087-9100, 1981.

Killeen, T.L., R.G. Roble, and N.W. Spencer, A computer model of global thermospheric winds and temperatures, *Adv. Space Res., 7*, 207-215, 1987.

Lockwood, G.E.K. and L.E. Petrie, Low latitude field aligned ionization observed by the Alouette topside sounder, *Planet. Space Sci., 11*, 327-330, 1963.

Malcolm, R., C. Miles, and B.A. Tinsley, Field aligned observations of transequatorial bubbles from Rarotonga in 1969-70, *Geophys. Res. Lett, 11*, 665-668, 1984.

Maruyama, T., A diagnostic model for equatorial spread F 1. Model description and application to electric field and neutral wind effects, *J. Geophys. Res., 93*, 14,611-14,622, 1988.

Maruyama, T., $\boldsymbol{E} \times \boldsymbol{B}$ instability in the F-region at low- to midlatitudes, *Planet. Space Sci., 38*, 273-285, 1990.

Maruyama, T. and N. Matuura, Global distribution of occurrence probability of spread echoes based on ISS-b observation, *J. Radio Res. Labs., 27*, 201-216, 1980.

Maruyama, T., and N. Matuura, Longitudinal variability of annual changes in activity of equatorial spread F and plasma bubbles, *J. Geophys. Res., 89*, 10,903-10,912, 1984.

Matuura, N., M. Kotaki, S. Miyazaki, E. Sagawa and I. Iwamoto, ISS-b experimental results on global distributions of ionospheric parameters and thunderstorm activity, *Acta Astronautica, 8*, 527-548, 1981.

McClure, J.P., W.B. Hanson and J.H. Hoffman, Plasma bubbles and irregularities in the equatorial ionosphere, *J. Geophys. Res., 82*, 2650-2656, 1977.

Morse, F.A., B.C. Edgar, H.C. Rice, W.J. Heikkila, J.H. Hoffman, B.A. Tinsley, J.D. Winningham, A.B. Christensen, R.W. Woodman, S. Pomalaza, and N.R. Teixeira, Equion, an equatorial ionosphere irregularity experiment, *J. Geophys. Res., 82*, 578-592, 1977.

Muldrew, D.B., Radio propagation along magnetic field-aligned sheets of ionization observed by the Alouette topside sounder, *J. Geophys. Res., 68*, 5355-5370, 1963.

Muldrew. D. B., The formation of ducts and spread F and the initiation of bubbles by field-aligned currents, *J. Geophys. Res., 85*, 613-625, 1980a.

Muldrew, D. B., Characteristics of ionospheric bubbles determined from aspect sensitive scatter spread F observed with Alouette 1, *J. Geophys. Res., 85*, 2115-2123, 1980b.

Murphy, J.A., and R.A. Heelis, Implications of the relationship between electromagnetic drift components at mid and low latitudes, *Planet. Space Sci., 34*, 645-652, 1986.

Murphy, J. A., G. J. Bailey, and R. J. Moffett, A theoretical study of the effects of quiet-time electromagnetic drifts on the behavior of thermal plasma at midlatitudes, *J. Geophys. Res., 85*, 1979-1986, 1980.

Ogawa, T., and H. Kumagai, Deep depletions of total electron content associated with severe mid-latitude gigahertz scintillations during geomagnetic storms, *J. Geophys. Res., 90*, 6652-6656, 1985.

Ossakow, S.L., Spread-*F* theories - a review, *J. Atmos. Terr. Phys., 43*, 437-452, 1981.

Ossakow, S.L., S.T. Zalesak, B.E. McDonald and P.K. Chaturvedi, Nonlinear equatorial spread *F*: Dependence on altitude of the *F* peak and bottomside background electron density gradient scale length, *J. Geophys. Res., 84*, 17-29, 1979.

Ott, E., Theory of Rayleigh-Taylor bubbles in the equatorial ionosphere, *J. Geophys. Res., 83*, 2066-2070, 1978.

Oya, H., T. Takahashi, and S. Watanabe, Observation of low latitude ionosphere by the impedance probe on board the Hinotori satellite, *J. Geomag. Geoelectr., 38*, 111-123, 1986.

Perkins, F., Spread *F* and ionospheric currents, *J. Geophys. Res., 78*, 218-226, 1973.

Pingree, J.E., and B.G. Fejer, On the height variation of the equatorial *F* region vertical plasma drifts, *J. Geophys. Res., 92*, 4763-4766, 1987.

Raitt, W.J., R.W. Schunk, and P.M. Banks, A comparison of the temperature and density structure in high and low speed thermal proton flows, *Planet. Space Sci., 23*, 1103-1117, 1975.

Rastogi, R.G., Seasonal variation of equatorial spread *F* in the American and Indian zones, *J. Geophys. Res., 85*, 722-726, 1980.

Rishbeth, H., Thermospheric winds and the *F*-region: A review, *J. Atmos. Terr. Phys., 34*, 1-47, 1972.

Scannapieco, A.J. and S.L. Ossakow, Nonlinear equatorial spread *F*, *Geophys. Res. Lett., 3*, 451-454, 1976.

Shimazaki, T., A statistical study of world-wide occurrence probability of spread *F*, 1, Average state, *J. Radio Res. Labs., 6*, 669-687, 1959.

Sipler, D.P., M.A. Bionodi, and R.G. Roble, *F*-region neutral winds and temperatures

at equatorial latitudes: measured and predicted behaviour during geomagnetically quiet conditions, *Planet. Space Sci., 31*, 53-66, 1983.

Stubbe, P., Frictional forces and collision frequencies between moving ion and neutral gases, *J. Atmos. Terr. Phys., 30*, 1965-1985, 1968.

Stubbe, P., Simultaneous solution of the time dependent coupled continuity equations, and equations of motion for a system consisting of a neutral gas, an electron gas, and a four component ion gas, *J. Atmos. Terr. Phys., 32*, 865-903, 1970.

Tanaka, T., Low-latitude ionospheric disturbances: Results for March 22, 1979, and their general characteristics, *Geophys. Res. Lett., 13*, 1399-1402, 1986.

Tanaka, T., ISIS 2 observations of the irregularity distribution during the low-latitude ionospheric disturbance event caused by the magnetospheric electric field, *Ann. Geophys., 5A*, 421-428, 1987.

Tanaka, T., and K. Hirao, Effects of an electric field on the dynamical behavior of the ionospheres and its application to the storm time disturbance of the *F*-layer, *J. Atmos. Terr. Phys., 35*, 1443-1452, 1973.

Torr, M.R., and D.G. Torr, Ionization frequencies for solar cycle 21: Revised, *J. Geophys. Res., 90*, 6675-6678, 1985.

Tsunoda, R.T., Control of the seasonal and longitudinal occurrence of equatorial scintillations by the longitudinal gradient in integrated *E* region Pedersen conductivity, *J. Geophys. Res., 90*, 447-456, 1985.

Tsunoda, R.T., On the generation and growth of equatorial backscatter plumes 2. Structuring of the west walls of upwellings, *J. Geophys. Res., 88*, 4869-4874, 1983.

Watanabe, S. and H. Oya, Occurrence characteristics of low latitude ionosphere irregularities observed by impedance probe on board the Hinotori satellite, *J. Geomag.*

Geoelectr., 38, 125-149, 1986.

Weber, W.J., J. Buchau, R.H. Eather, and S.B. Mende, North-south aligned equatorial airglow depletions, *J. Geophys. Res., 83*, 712-716, 1978.

Wharton, L. E., N. W. Spencer, and H. G. Mayr, The earth's thermospheric super rotation from Dynamics Explorer 2, *Geophys. Res. Lett., 11*, 531-533, 1984.

Woodman, R.F. and C. LaHoz, Radar observations of F region equatorial irregularities, *J. Geophys. Res., 81*, 5447-5466, 1976.

Zalesak, S.T., S.L. Ossakow and P.K. Chaturvedi, Nonlinear equatorial spread F: The effect of neutral winds and background Pedersen conductivity, *J. Geophys. Res., 87*, 151-166, 1982.